Modeling and interpretation of the ultraviolet spectral energy distributions of primeval galaxies

Alba Vidal García

▶ To cite this version:

Alba Vidal García. Modeling and interpretation of the ultraviolet spectral energy distributions of primeval galaxies. Astrophysics [astro-ph]. Université Pierre et Marie Curie - Paris VI, 2016. English. NNT : 2016PA066667 . tel-01658921

HAL Id: tel-01658921
https://theses.hal.science/tel-01658921
Submitted on 8 Dec 2017

HAL is a multi-disciplinary open access archive for the deposit and dissemination of scientific research documents, whether they are published or not. The documents may come from teaching and research institutions in France or abroad, or from public or private research centers.

L'archive ouverte pluridisciplinaire **HAL**, est destinée au dépôt et à la diffusion de documents scientifiques de niveau recherche, publiés ou non, émanant des établissements d'enseignement et de recherche français ou étrangers, des laboratoires publics ou privés.

École Doctorale d'Astronomie et Astrophysique d'Île-de-France

UNIVERSITÉ PARIS VI - PIERRE & MARIE CURIE

DOCTORATE THESIS

to obtain the title of Doctor of the
University of Pierre & Marie Curie in Astrophysics

Presented by
Alba Vidal García

Modeling and interpretation of the ultraviolet spectral energy distributions of primeval galaxies

Thesis Advisor: Stéphane Charlot

prepared at Institut d'Astrophysique de Paris, CNRS (UMR 7095),
Université Pierre & Marie Curie (Paris VI)
with financial support from the
European Research Council grant 'ERC NEOGAL'

Composition of the jury

Reviewers:	Alessandro Bressan	-	SISSA, Trieste, Italy
	Rosa González Delgado	-	IAA (CSIC), Granada, Spain
Advisor:	Stéphane Charlot	-	IAP, Paris, France
President:	Patrick Boissé	-	IAP, Paris, France
Examinators:	Jeremy Blaizot	-	CRAL, Observatoire de Lyon, France
	Vianney Lebouteiller	-	CEA, Saclay, France

Dedicatoria

Contents

Abstract vii

Résumé ix

1 Introduction 3
- 1.1 Historical context 4
- 1.2 Early epochs of the Universe 5
- 1.3 Galaxy types 6
- 1.4 Components of a Galaxy 8
  - 1.4.1 Classification of stars 9
  - 1.4.2 The ISM: components and phases 9
  - 1.4.3 Physical processes in the ISM 12
- 1.5 Chemical content of a galaxy 17
- 1.6 Galaxy spectral energy distributions 17
- 1.7 Future observing facilities 19
- 1.8 Outline 20

2 Modeling spectral energy distributions of galaxies 23
- 2.1 Stellar emission 24
  - 2.1.1 Stellar population synthesis codes 24
  - 2.1.2 Evolutionary tracks 25
  - 2.1.3 IMF 29
  - 2.1.4 Stellar spectral libraries 30
- 2.2 Absorption and emission in the ISM 31
  - 2.2.1 Photoionization code: CLOUDY 31
  - 2.2.2 General spectrum synthesis code: SYNSPEC 33
  - 2.2.3 Summary of the modeling 33
- 2.3 The star formation history of galaxies 34

3 Calibration of the SSP models in the ultraviolet 37
- 3.1 Introduction 38
- 3.2 Ultraviolet signatures of young stellar populations 40
  - 3.2.1 Stellar population synthesis modelling 40
  - 3.2.2 Ultraviolet spectral indices 41
  - 3.2.3 Dependence of index strength on age, metallicity and integrated stellar mass 41
  - 3.2.4 Associated broadband magnitudes 46
- 3.3 Interpretation of ultraviolet star-cluster spectroscopy 46
  - 3.3.1 Observational sample 46
  - 3.3.2 Model library 48
  - 3.3.3 Age, metallicity and stellar-mass estimates 49

4 Influence of the ISM on ultraviolet spectra of star-forming galaxies 57
4.1 ISM modelling 58
4.1.1 Approach 58
4.1.2 Examples of model spectra 64
4.2 Ultraviolet tracers of stars and the ISM 67
4.2.1 Features tracing young stars 67
4.2.2 Features tracing nebular emission 71
4.2.3 Features tracing interstellar absorption 72
4.2.4 Important composite features 72

5 On statistical tools for galaxy SED-fitting 79
5.1 Standard methodology 80
5.2 In this work: BEAGLE. 81

6 Results from galaxy SED-fitting with BEAGLE 85
6.1 Lyα and C III] emission in $z = 7 - 9$ galaxies: accelerated reionization around luminous star-forming systems? 86
6.2 The three most metal-poor nearby galaxies 90
6.3 10 nearby galaxies with hard optical spectra 95

7 Conclusions and perspectives 99

Appendices 103

A Ultraviolet stellar absorption-line indices 105

B Correction of ultraviolet index strengths for Galactic absorption 109

C P-Cygni profiles 113

Bibliography 115

Abstract

In this work, I combine state-of-the-art models for the production of stellar radiation and its transfer through the interstellar medium (ISM) to investigate ultraviolet-line diagnostics of stars, the ionized and the neutral ISM in star-forming galaxies. I start by assessing the reliability of the stellar population synthesis modelling by fitting absorption-line indices in the ISM-free ultraviolet spectra of 10 Large-Magellanic-Cloud clusters. In doing so, I find that neglecting stochastic sampling of the stellar initial mass function in these young ($\sim$ 10–100 Myr), low-mass clusters affects negligibly ultraviolet-based age and metallicity estimates but can lead to significant overestimates of stellar mass. Then, I proceed and develop a simple approach, based on an idealized description of the main features of the ISM, to compute in a physically consistent way the combined influence of nebular emission and interstellar absorption on ultraviolet spectra of star-forming galaxies. My model accounts for the transfer of radiation through the ionized interiors and outer neutral envelopes of short-lived stellar birth clouds, as well as for radiative transfer through a diffuse intercloud medium. I use this approach to explore the entangled signatures of stars, the ionized and the neutral ISM in ultraviolet spectra of star-forming galaxies. I find that, aside from a few notable exceptions, most standard ultraviolet indices defined in the spectra of ISM-free stellar populations are prone to significant contamination by the ISM, which increases with metallicity. I also identify several nebular-emission and interstellar-absorption features, which stand out as particularly clean tracers of the different phases of the ISM.

Résumé

Je combine de nouveaux modéles de production de radiations stellaires et de transport radiatif á travers le milieu interstellaire (MI). Cela permet de caractériser les étoiles ainsi que le MI neutre et ionisé dans des galaxies formant des étoiles (GFE), via des raies ultraviolettes dans leur spectre. J'évalue la fiabilité des modèles stellaires en ajustant dans l'ultraviolet les indices d'absorption mesurés dans les spectres stellaires de 10 amas d'étoiles dans le Grand Nuage de Magellan. Je montre que négliger l'échantillonnage stochastique de la fonction de masse initiale stellaire de ces amas jeunes et peu massifs a une faible influence dans l'estimation d'âge et de métallicité, mais peut entraîner une surestimation significative des estimations de leur masse. Ensuite, je développe une approche basée sur une description épurée des principales caractéristiques du MI, afin de calculer de manière auto-cohérente l'influence combinée de l'émission et de l'absorption de ce milieu dans le spectre ultraviolet des GFE. Ce modèle tient compte du transport radiatif aussi bien à travers les couches intérieures ionisées, qu'à travers les couches extérieures neutres des nuages de formation d'étoiles ainsi que le milieu diffus entre ces nuages. J'utilise cette approche pour étudier la signature enchevêtrée des étoiles, du milieu neutre et du milieu ionisé dans les spectres ultraviolets des GFE. J'obtiens que la plupart des indices stellaires dans l'ultraviolet sont susceptibles de présenter une contamination par le MI qui augmente avec la métallicité. Enfin, j'identifie des raies d'émission et d'absorption interstellaires pouvant discriminer efficacement les différrentes phases du MI.

dam

Chapter 1

Introduction

In this thesis, I present a new approach to model in a physically consistent way the competing effects of stellar absorption, nebular emission and interstellar absorption in ultraviolet spectra of star-forming galaxies. I achieve this by combining state-of-the-art models for the production of stellar radiation and its transfer through the ISM to investigate ultraviolet-line diagnostics of stars, the ionized and the neutral ISM in star-forming galaxies. The goal of this chapter is to summarize the main physical processes controlling the different components of galaxies, placing this in the general framework of what we know so far about the formation and evolution of galaxies.

Contents

1.1 Historical context **4**
1.2 Early epochs of the Universe **5**
1.3 Galaxy types **6**
1.4 Components of a Galaxy **8**
  1.4.1 Classification of stars 9
  1.4.2 The ISM: components and phases 9
  1.4.3 Physical processes in the ISM 12
1.5 Chemical content of a galaxy **17**
1.6 Galaxy spectral energy distributions **17**
1.7 Future observing facilities **19**
1.8 Outline **20**

1.1 Historical context

At the beginning of the 20th century, the knowledge that we had of the Universe was very different from the one we have today. The Milky Way was thought to be the only galaxy in the Universe, at that epoch known as *Island universes*. This idea was taken to debate the 26th of April 1920, in the renowned *Great debate*, and the main question to answer was whether these distant Island universes or nebulae, such as Andromeda, were part of the Milky Way or if they were independent galaxies. Harlow Shapley defended the point of view that spiral nebulae are part of the Milky Way with a size argument; he claimed that if Andromeda were not part of the Milky Way, the distance between the two would be of 10^8 light years, a distance greater than what astronomers at that epoch thought was the size of the Universe. In contrast, Heber Doust Curtis defended the nature of Andromeda as an independent nebula for various reasons. His main arguments were that the nova[1] rate in Andromeda was found to be higher than that in the Milky Way and also that velocity measurements performed by Vesto Slipher on several of these nebulae suggested that they are not gravitationally bound to the Milky Way. A few years later, in 1925, Edwin Hubble established that these nebulae are too distant to be part of the Milky Way, suggesting that the Universe extends further than what was thought before, and that those diffuse objects have sizes similar to that of the Milky Way. Hubble was able to measure the distance to these objects through observations of Cepheid stars, whose Period-Luminosity relation[2] had been discovered by Henrietta Swan Leavitt. Hubble demonstrated in this way that Curtis' vision of the Universe was likely to be more accurate than that of Shapley. Instead, Shapley was right about the position of the Solar System, which he placed in the outer regions of the Milky Way, while Curtis had placed it at the center. On other points, both scientists were partly right. For example, the size of the Milky Way is in between the estimates that both proposed.

In addition to measuring distances to nearby galaxies, Hubble compared these with recession velocities measured by Vesto Slipher and found a correlation between both quantities known as the *Hubble law*:

$$v = H_0\, d, \tag{1.1}$$

where v is the recession velocity, d the distance to the object and H_0 the proportionally constant (known as the *Hubble constant*). To calculate the recession velocity, we recall the Doppler effect for non relativistic objects:

$$\frac{\lambda_{obs} - \lambda_{em}}{\lambda_{em}} = \frac{v}{c}, \tag{1.2}$$

where v is the velocity of the emitting source with respect to the receptor, c the speed of light, λ_{obs} the wavelength at which the observer detects the light and λ_{em} the wavelength at which the light is emitted. The *redshift*, z, is defined as:

$$z = \frac{\lambda_{obs} - \lambda_{em}}{\lambda_{em}}\,. \tag{1.3}$$

Combining Equations (1.1), (1.2) and (1.3), we find that, for non-relativistic objects, the Hubble law can be expressed as:

$$cz = H_0\, d\,. \tag{1.4}$$

---

[1] A nova is a cataclysmic nuclear explosion on a white dwarf.

[2] The period-luminosity relation for Cepheids states that the intrinsic luminosity of these variable stars is related to a regular pulsation period, making them the first *standard candles* to be discovered.

Hence, redshift can be used as a measurement of distance in the Universe. Based on these arguments, Hubble concluded that galaxies are moving away from the Milky Way and that the Universe is expanding (Hubble, 1929).

The expansion of the Universe can be understood in the framework of the Friedmann-Robertson-Walker solution to Einstein's equations. In the standard model of cosmology, the Universe is homogeneous and isotropic (as stated in the cosmological principle) and expanding in an accelerated way. According to this model, the story of the Universe began ~ 13.7 Gyr ago in an initial explosion, called the Big Bang, after which the Universe has been expanding and cooling. Recent observations of distant Type-Ia supernovae (a calibrated standard candle) have shown that this expansion is accelerated (Riess et al., 1998; Spergel et al., 2003), due to a fluid qualified as Dark Energy, corresponding to the cosmological constant Λ in Einstein's equations.

Another main component of the Universe is Dark Matter. In the standard cosmological model, Dark matter accounts for $\sim 23\%$ of the total energy density of the Universe, while Dark Energy accounts for $\sim 72\%$ and the remaining $\sim 5\%$ is in the form of baryonic matter. Dark matter does not interact electromagnetically with baryonic matter, but it interacts gravitationally. We thus cannot see it, but it has been detected for example in measurements of rotational curves of galaxies (which reveal the strong influence of a dark dynamic component in the outskirts) and by gravitational lensing in galaxy clusters.

Dark matter plays a major role in the growth of structure in the Universe, the idea accepted so far being that dark matter structures grow from small perturbations in the initial density field. These density perturbations grow fast, amplified by gravity, into dark matter halos where baryons merge to form galaxies. The complexity of these interactions makes a complete theoretical understanding of how galaxies form and evolve elusive. However, much progress has been accomplished in this area with the development over the last decades of new ground-based and space-based observatories across the entire electromagnetic spectrum, from γ-ray to radio wavelengths, improving tremendously our knowledge of the physical processes ongoing in galaxies on different scales. The aim of the following sections is to present a general view of what we have learned about the formation and evolution of galaxies thanks to these observations.

1.2 Early epochs of the Universe

One of the goals of this thesis is to provide the community with new models to interpret the light emitted by galaxies from the very first episodes of star formation in the Universe, which, according to the standard model of cosmology, occurred over 13 Gyr ago. To set the scene for this study, it is worth briefly summarizing the main epochs through which our Universe has gone during the first billion years after the Big Bang:

- Recombination epoch. At the beginning, the Universe was a hot and dense plasma of protons, neutrons, electrons and other elemental particles. While expanding, the Universe eventually became cool enough to let hydrogen and helium nucleons capture electrons to form electrically neutral atoms. This process, known as *recombination*, is thought to have occurred relatively fast around $\sim 380,000$ years after the Big Bang. At the end of this epoch, most protons and neutrons were parts of atoms, which increased the photons' mean free path[3]. Indeed at the end of recombination, photons could travel freely without being scattered any longer by free electrons through Thompson scattering. This cosmic event is usually referred to as *matter-radiation decoupling*. The first photons to escape that plasma are the same that we see today in the cosmic microwave background (CMB). This radiation has been observed with satellites like the *Cosmic Microwave Background Explorer* (*COBE*), the *Wilkinson Microwave Anisotropy Probe* (*WMAP*) and *Planck* after traveling through an expanding and cooling Universe.

---

[3] The mean free path is the distance that a particle can travel without interacting with another one.

- Dark Ages. After Recombination, the Universe entered a transition period during which the only radiation emitted was the 21 cm line of neutral hydrogen. This period is thought to have lasted from between 150 and 800 million years after the Big Bang, during which the temperature of the CMB cooled from 4000 to about 60 K.

- Reionization. The first stars to form in the Universe are expected to have been very hot and massive and therefore capable of emitting a large amount of ionizing photons. This radiation reionized neutral hydrogen and the Universe became again an ionized plasma. The last results from the *Planck* collaboration indicate that this epoch must have occurred at redshifts in the range $6 \lesssim z \lesssim 10$ (Planck Collaboration et al., 2016). Aside from newly formed stars in starburst galaxies, it is also believed that Active Galactic Nuclei (AGN)[4] helped reionize neutral hydrogen. Yet, little is known about the relative contributions by galaxies and AGN (Haardt & Salvaterra, 2015), which makes it crucial to characterize the physical properties of galaxies at this period.

Fig. 1.1 shows a schematic diagram of this early history of the Universe, along with the subsequent evolution of galaxies until the appearance of our solar system.

1.3 Galaxy types

Galaxies exhibit different colors, shapes and sizes. Hubble made the first classification of galaxies based on morphology (Hubble, 1926). Fig. 1.2 shows the division of galaxies he proposed between *Ellipticals* (E), *Lenticulars* (S0), *Spirals* (Sa, Sb, Sc, ...; which can also be barred: SBa, SBb, SBc, ...) and *Irregulars* (Irr). It is also common to denote galaxies on the left-hand side of the sequence in Fig. 1.2 as *early-type galaxies* and those on the right-hand side as *late-type galaxies*. Following the same logic, Sa and SBa galaxies are often referred to as early-type spirals, Sb and SBb galaxies as intermediate-type spirals and Sc and SBc galaxies as late-type spirals. This terminology was borrowed from stars, where young and massive stars of O and B types were known as early-type stars while older stars were known as late-type stars. Hubble stated that his classification had no evolutionary implication, but eventually, it was discovered that early-type galaxies are dominated by late-type stars and late-type galaxies show a larger content of early-type stars.

Galaxy morphology correlates with color. A color traces the flux ratio between a long and a short wavelengths, changing from blue to red as this ratio increases. Early-type galaxies tend to show red colors because they are dominated by evolved stellar populations and have little gas content, while the young stellar content of gas-rich, star-forming late-type galaxies makes these

---

[4] An Active Galactic Nucleus is a compact region at the center of a galaxy, which has much higher luminosity than the galaxy over some portion of the electromagnetic spectrum. The radiation from an AGN is believed to result from accretion of matter by a supermassive black hole at the center of the host galaxy.

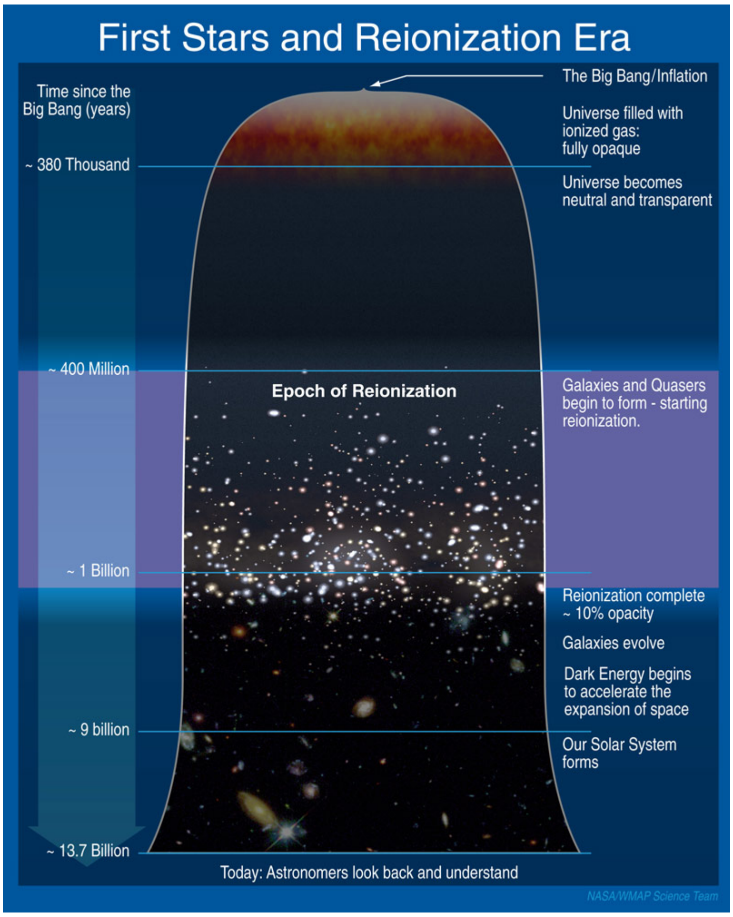
First Stars and Reionization Era
Time since the Big Bang (years)
~ 380 Thousand
~ 400 Million
~ 1 Billion
~ 9 billion
~ 13.7 Billion
The Big Bang/Inflation
Universe filled with ionized gas: fully opaque
Universe becomes neutral and transparent
Epoch of Reionization
Galaxies and Quasars begin to form - starting reionization.
Reionization complete ~ 10% opacity
Galaxies evolve
Dark Energy begins to accelerate the expansion of space
Our Solar System forms
Today: Astronomers look back and understand
NASA/WMAP Science Team

Figure 1.1 – Scheme of the different evolutionary epochs in the Universe, from the Big Bang until the present time. Credit: Wikipedia.

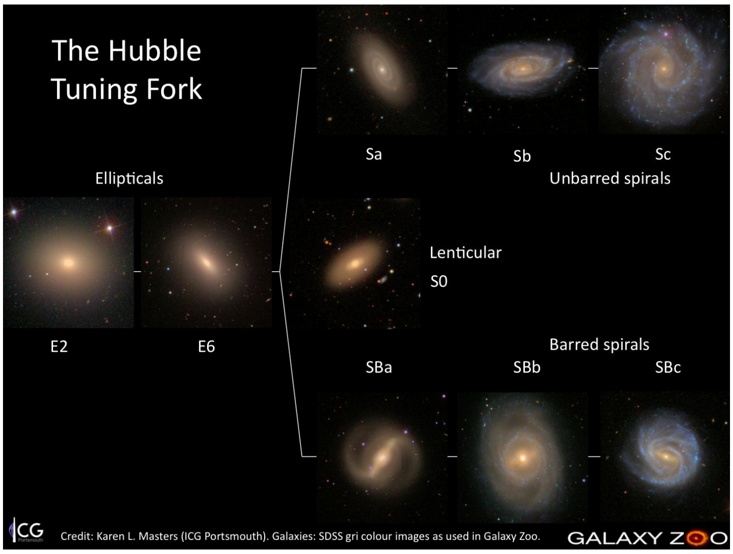
The Hubble Tuning Fork
Ellipticals
E2
E6
Sa
Sb
Sc
Unbarred spirals
Lenticular
S0
Barred spirals
SBa
SBb
SBc
ICG
Credit: Karen L. Masters (ICG Portsmouth). Galaxies: SDSS gri colour images as used in Galaxy Zoo.
GALAXY ZOO

Figure 1.2 – Hubble classification of galaxies based on morphology. Credit: Karen L. Masters.

galaxies bluer, modulo the effect of dust reddening.

Another way of classifying galaxies is by plotting them in a diagram of star-formation rate versus stellar mass, the latter being the result of all previous star-formation episodes. This diagram is schematically represented in Fig. 1.3, where we can distinguish various modes of star formation: a *main sequence* of star formation where the majority of galaxies lie; a *starburst* mode, corresponding to more actively star-forming galaxies than main-sequence galaxies at a given stellar mass; a *red sequence*, composed of galaxies with negligible star formation and dominated by evolved stellar populations; and a *green valley*, populated by galaxies traveling from the main sequence to the red sequence. We also see a positive correlation between stellar mass and star formation rate.

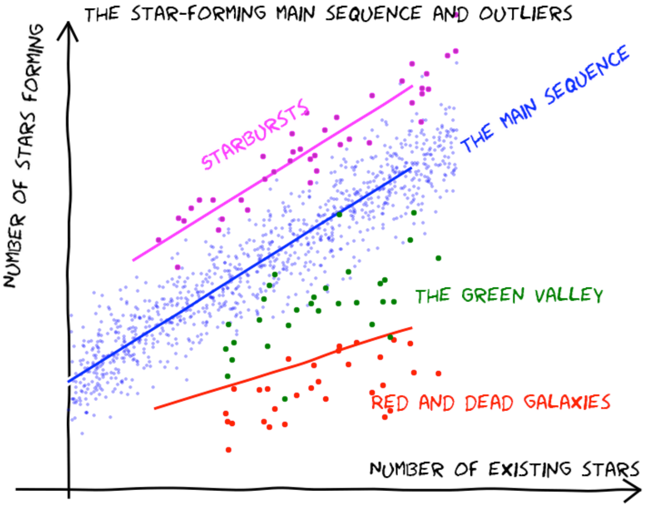

Figure 1.3 – Classification of galaxies based on star-formation activity. Credit: Brian Koberlein.

1.4 Components of a Galaxy

A galaxy like the Milky Way can be seen as a gravitationally bound ensemble of stars, gas, dust and dark matter. Dynamically, most of the mass appears to be in the form of dark matter, whose presence we can infer from the flattening of galaxy rotation curves at large radii. Stars are another important component of galaxies, because they emit most of the light we can observe and are the main drivers of chemical enrichment. In the Milky Way, about 10 % of the total mass is stored in stars of different masses, ages, temperatures and metallicities (see Section 1.4.1 for more details about the different stellar populations in disk galaxies). Another $\sim 10\%$ of the mass of the Milky Way is accounted for by gas at different temperatures and densities (see Section 1.4.2). Finally, dust accounts for only about 0.1% of the mass of the Milky Way, in the form of small (0.1-1μm) particles composed of carbon, oxygen, silicon and other metals, the most abundant being composites of silicates and graphite. Despite its small contribution to the mass budget, dust has significant effect on the appearance of galaxies as it absorbs radiation at ultraviolet and optical wavelengths, which it reemits at mid- and far-infrared (IR) wavelengths.

In this thesis, I am interested in modeling and characterizing the light emitted by stars and how this light interacts with the different components of the interstellar medium (or ISM) before emerging from a star-forming galaxy. For this reason, in the next subsections, I briefly summarize the main properties these different components and the physical processes occurring in the ISM of star-forming galaxies.

1.4.1 Classification of stars

Stars are valuable tracers of the past and current physical conditions in galaxies. By studying the light emitted by stars, we can learn about, for example, their ages and chemical compositions, the past star formation history and the physical conditions in the ISM currently attenuating their light. Stars are classified according to age and metallicity, as follows:

- Population III stars. These are the very first stars to form at the end of the dark ages in the history of the Universe. They are thought to have formed by the collapse of giant clouds of primordial gas in low-mass dark-matter minihaloes (with masses $< 10^6$ $\mathrm{M}_\odot$). At this early stage of evolution of the Universe, the gas is still not polluted with metals, so the temperature remains too high for the gas to fragment efficiently[5]. These stars are therefore traditionally expected to be very massive (e.g. around several hundred solar masses, Bromm et al., 1999) and metal poor (with metallicities $< 10^{-4}\,Z_\odot$, Schneider et al., 2002) and to contain mainly hydrogen and helium and some traces of primordial lithium. These massive stars consume their fuel via thermonuclear reactions very fast and explode as type-II supernovae (SNe), which pollute the ISM with α-capture elements (mostly O, S, Ne, Si and Mg).

- Population II stars. After the explosion of the first SNe, gas polluted with metals can cool more efficiently and fragment in less massive clouds than primordial gas. This produces Pop II stars, with lower masses and higher metallicities than those of Pop III stars. These stars can be found today in the haloes and bulges of spiral galaxies and have metallicities in the range from 0.001 to 0.1 times $Z_\odot$.

- Population I stars. On a timescale of the order of a billion years, gas becomes heavily polluted in iron-peak elements through the explosion of type-Ia SNe[6]. This produces Pop I stars with metallicities $Z > 0.1\,Z_\odot$, which can be found in the disks of spiral galaxies today like our own Sun.

1.4.2 The ISM: components and phases

The main components of the interstellar medium are the dust and gas between stars. My primary aim in this work being to model the influence of the ISM on stellar radiation in star-forming galaxies, I briefly summarize below the main phases of the gas in the ISM and the effect of dust on galaxy spectra, leaving aside more remote subjects, such as the interactions between the ISM and dark matter, heating of the ISM by cosmic rays and the interstellar magnetic field.

Dust is made of small solid particles with sizes around 0.1-1μm, whose presence in the ISM is revealed by various observational signatures. Among these, we can find the wavelength-dependent extinction (or attenuation)[7] of starlight, and the reradiation at mid- and far-infrared wavelengths of light absorbed at shorter wavelengths. Indirect measurements of the dust have also been carried out. Studies of abundances of the interstellar gas suggest that some elements are missing from the gas phase, presumably because they have been *depleted* onto dust grains (Draine, 1990). The extinction A_λ, measured in magnitudes (see Section 1.6 for a definition of magnitude), is defined as:

---

[5] This is because gas cooling is more efficient when it occurs through radiative deexcitation of collisionally excited metal transitions.

[6] An explosion occurring after an accreting white dwarf in a binary system exceeds the Chandrasekhar limit of ~ 1.4 $\mathrm{M}_\odot$, beyond which the electron pressure degeneracy is no longer sufficient to prevent the collapse of the star.

[7] *Extinction* usually refers to the absorption of photons along and their scattering out of a single line of sight to a star or quasar, while *attenuation* refers to the combined effects of absorption and scattering in and out of the line of sight toward a galaxy, caused by both local and global geometric effects.

$$\frac{A_\lambda}{\text{mag}} = -2.5 \log \left(\frac{F_\lambda}{F_\lambda^0} \right), \tag{1.5}$$

where F_λ is the flux observed from the star and F_λ^0 is the flux that would be observed in the absence of dust. The extinction measured in magnitudes is also proportional to the optical depth:

$$\frac{A_\lambda}{\text{mag}} = -2.5 \log \left(e^{-\tau_\lambda} \right) = 1.086 \tau_\lambda, \tag{1.6}$$

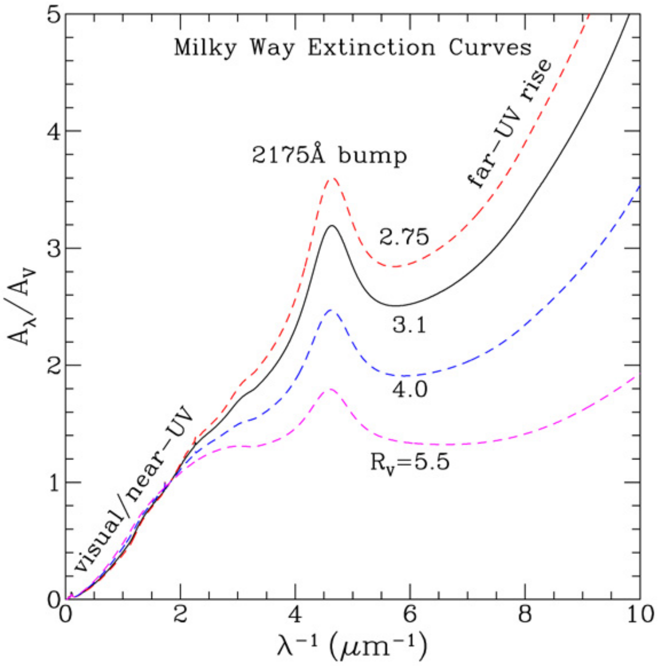

Figure 1.4 – Interstellar extinction curves of the Milky Way ($R_V = 2.75, 3.1, 4.0, 5.5$). There exist considerable regional variations in the Galactic optical/UV extinction curves, as characterized by the total-to-selective extinction ratio R_V, indicating that dust grains on different sightlines have different size distributions. Credit: https://ned.ipac.caltech.edu/level5/Sept07/Li2/Li2.html.

Fig. 1.4 shows a typical extinction curve, with A_λ increasing from red to blue wavelengths. This causes the light reaching us from a background source to be reddened. Since a grain absorbs and scatters light most effectively at wavelengths comparable to its size, the detailed wavelength dependence of A_λ is sensitive to the composition and size distribution of dust particles. In fact, observed extinction curves vary in shape from one line of sight to another. The slope of A_λ at visible wavelengths is characterized by the dimensionless ratio R_V:

$$R_V \equiv \frac{A_V}{A_B - A_V} \equiv \frac{A_V}{E(B-V)}, \tag{1.7}$$

where A_B and A_V are the extinctions measured in the B(4405Å) and V(5470Å) photometric bands, and $E(B-V) \equiv A_B - A_V$ is the reddening. As a reference, sightlines through the diffuse gas in the Milky Way have $R_V \approx 3.1$.

We now turn to the baryonic gas component, which in the Milky Way is found in a wide range of temperatures and densities. These can be arranged roughly in a few main phases known as Coronal gas, HII gas, Warm HI gas, Cool HI gas, molecular gas and stellar outflows.

- Coronal gas. This corresponds to gas heated to temperatures $T \gtrsim 10^{5.5} K$ by shocks from blastwaves of supernova explosions. This gas is collisionally ionized and found at low densities, typically around $n_{\rm H} \sim 0.004\,{\rm cm}^{-3}$.

- HII gas. This corresponds to gas photoionized by ultraviolet photons from hot stars. Most of this photoionized gas is maintained at temperatures in the range $T = 30,000$–$50,000\,{\rm K}$ by radiation from recently formed, massive hot O–B stars. This gas may be dense material in a star-forming cloud (HII region) or lower-density gas in the intercloud medium (diffuse HII). Bright HII regions, such as the Orion Nebula, have dimensions of a few pc; their lifetimes are essentially those of the ionizing stars, $\sim$ 3–10 Myr, and their masses in the range from 10^2 to 10^4 $M_\odot$. An HII region is generally described as a *Strömgren Sphere*, i.e., an ionized region around the ionizing source that is separated from the outer neutral region by a transition zone ionizing photons cannot cross. HII regions and diffuse ionized gas are expected to have temperatures $T \gtrsim 10^4\,{\rm K}$ and densities ranging from $n_{\rm H} = 0.2\,{\rm cm}^{-3}$ up to $10^4\,{\rm cm}^{-3}$. We note that photoionized gas can also be found in much fainter, short-lived ($\sim 10^4\,{\rm yr}$) planetary nebulae.[8]

- Warm HI gas. This is mainly atomic gas heated to temperatures around $T \approx 5000\,{\rm K}$. In the local interstellar medium, this gas is found at densities $n_{\rm H} \approx 0.6\,{\rm cm}^{-3}$. It fills a significant fraction of the disk volume, around $\sim$ 40%, and is sometimes referred to as the warm neutral medium, or WNM.

- Cool HI gas. This is predominantly atomic gas at temperatures around $T \approx 100\,{\rm K}$ and densities around $n_{\rm H} \approx 30\,{\rm cm}^{-3}$, which fills $\sim$ 1% of the volume of the local interstellar medium. It is sometimes referred to as the cold neutral medium, or CNM.

- Molecular gas. This can be divided into diffuse molecular gas and dense molecular gas. The diffuse molecular gas is similar to the cool HI gas, but with sufficiently large densities and column densities for self-shielding[9] to allow H_2 molecules to survive in the cloud. The dense molecular clouds are gravitationally bound clouds with densities of $n_{\rm H} \gtrsim 10^3\,{\rm cm}^{-3}$. These clouds are often dark, with visual extinction $A_V \gtrsim 3\,{\rm mag}$ through the central regions. It is within these regions that star formation takes place.

- Stellar outflows. Evolved stars can achieve mass loss rates of up to 10^{-4} $M_\odot\,{\rm yr}^{-1}$ with outflow velocities of $\lesssim 30\,{\rm km\,s}^{-1}$, leading to relatively dense outflows. Hot stars can have faster winds, although these are less dense.

---

[8] A planetary nebula forms when rapid mass loss occurring during the last stages of evolution of stars with initial masses $0.8\ M_\odot < M < 6\ M_\odot$ exposes the hot stellar core. See Section 2.1.2 for more details on the last evolutionary stages of different types of stars.

[9] Self-shielding occurs when photoexcitation transitions become optically thick, so that the molecule is shielded from starlight by other molecules.

In this work, I adopt a simple description of the main features of the ISM inspired from the model of Charlot & Fall (2000). Fig. 1.5 shows a schematic representation of the stellar birth clouds and the ambient, diffuse ISM in this model. Stars are assumed to ionize HII regions in the molecular clouds where they are born. The emission-line photons produced in HII regions and the nonionizing continuum photons from young stars propagate through the outer HI envelopes of the birth clouds and then through the ambient ISM on their way out of the galaxy. The birth clouds have finite lifetimes, thus, photons emitted by older stars propagate only through the ambient ISM. See Section 4.1.1 for a detailed description of the modelling of the different phases of the ISM. I do not attempt to model coronal gas (as the photoionization code I am using is not adapted to model shocks) nor the molecular component in the clouds.

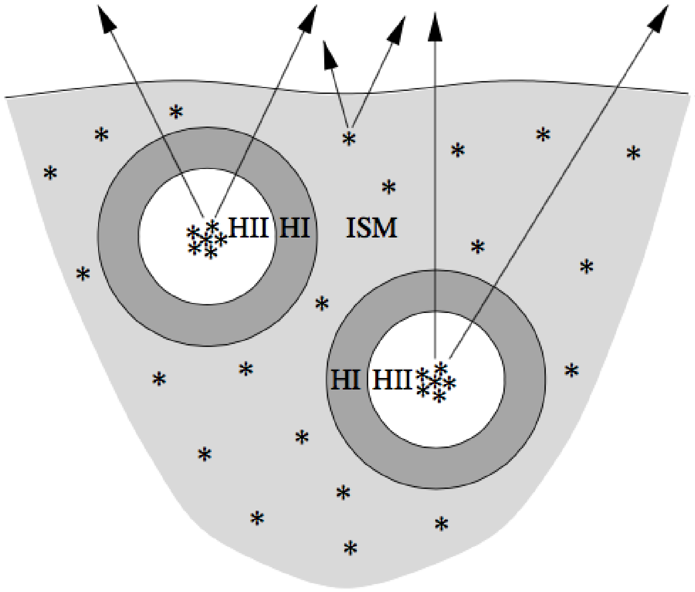

Figure 1.5 – Schematic representation of the birth clouds and ambient ISM surrounding each generation of stars in a model galaxy. Credit: Charlot & Fall (2000).

1.4.3 Physical processes in the ISM

Figure 1.5 provides an idealized description of the main phases of the ISM. In this section, I summarize the main physical processes that control, in these different phases, the absorption and emission features in the light emerging from star-forming galaxies. In particular, the ultraviolet spectra of such galaxies exhibit a myriad of spectral features produced by nebular emission lines, continuum emission and absorption line from the ISM. In the next paragraphs, I briefly describe how these different features are formed.

Emission-lines

The central ionizing source in an HII region, which can be either a single massive star or a young star cluster, must be hot enough ($T \gtrsim 30,000\,\mathrm{K}$) to emit H-ionizing photons, i.e. photons with energy $> 13.6\,\mathrm{eV}$ (corresponding to a wavelength $\lambda < 912\text{Å}$). If there is enough material around the ionizing source, the gas extends beyond the Strömgren Sphere and the nebula is called *ionization bounded*, as no ionizing photon can escape. A nebula truncated inside the Strömgren Sphere is known as a *density bounded* nebula.

The photoionization process releases an electron, which will tend to be recaptured by an ion in a process called *recombination.* During recapture, for example by an H^+ proton, the electron can land on any excited level of the atom and lead to a radiative cascade in one of several decays to lower energy levels. During each of these decays, a photon is emitted in an H I recombination line, which can be detected in the emergent spectrum as an emission line. The emitted photons have a particular energy corresponding to the energy difference between the departure and arrival levels. Most hydrogen recombination lines can be observed at optical and ultraviolet wavelengths. The lines are called differently depending on the lower level to which the electron decays (Fig. 1.6): *Lyman* lines are produced when the electron decays to the level $n = 1$, *Balmer* lines when the lower level is $n = 2$, *Paschen* lines when the electron decays to level $n = 3$, and so on. The strongest H-recombination lines are the Lyman-α line at 1216Å, the Balmer Hα (or just Hα) line with a wavelength of 6563Å, created from a transition of $n = 3$ to $n = 2$ levels and Balmer Hβ (or just Hβ) at 4861Å, due to the $n = 4$ to $n = 2$ level transition.

Regions of ionized gas are generally classified into two idealized types: the optically thin one, corresponding to case A recombination and the optically thick one, corresponding to case B recombination. In case A recombination, all Lyman-line photons produced through recombination escape from the nebula before they are reabsorbed by another atom, whereas in case B recombination, all Lyman-line photons are re-absorbed by other atoms until they finally cascade down to the $n = 2$ level and produce either a Lyman-α photon or a two-photon decay. I assume case B recombination in this work.

Helium can also be ionized in an H II region if the central source is hot enough to produce photons of energy higher than 24.6 eV, corresponding to the ionizing potential of Helium. When this occurs, He I recombination lines will appear in the emergent spectrum, such as He I 5876Å. If the central source is hot enough to produce photons of at least 54.4 eV, helium can also be doubly ionized, giving rise to He II recombination lines in the emergent spectrum, such as He II 4686 Å.

H II-region spectra can also exhibit collisionally excited emission lines from *metals* (i.e. elements heavier than H and He). These neutral or ionized elements can be excited through collisions with thermal electrons, which will lead to a jump of a valence electron to an excited metastable energy level. These levels have long lifetimes and therefore, at high gas densities, deexcitation will occur on a shorter timescale through a collision. In H II regions, however, the density is low enough for the timescale of a collision to be larger than the radiative decay deexcitation timescale. The electron will deexcite thus emitting a photon to a lower energy level and producing what is called a *forbidden line*, designated by square brackets. Examples of such lines are [O III] $\lambda\lambda$ 4959, 5007 Å and [S II] $\lambda\lambda$ 6717, 6731 Å. Depending on the spontaneous transition probabilities, we can also find semi-forbidden lines, designated by a single bracket, such as C III]λ 1909Å and O III]$\lambda\lambda$ 1661, 1666Å.

Hence, in an H II region, H is fully ionized, He can be singly or even doubly ionized and other elements can be singly or multiply ionized. The ionization structure of the interstellar medium will depend sensitively on the nature of the ionizing source.

Nebular continuum

In addition to the increase of the thermal continuum in the mid- and far-infrared due to

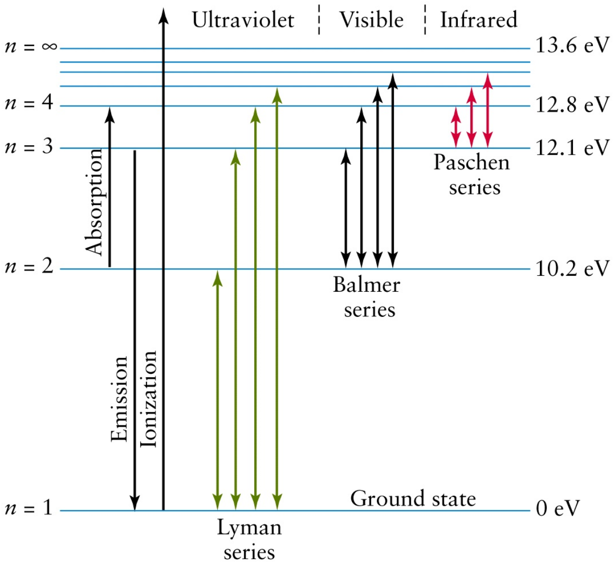

Figure 1.6 – Schematic representation of the electronic transitions of the hydrogen atom. Credit:https://leticiateran.wordpress.com/tag/energy/

the presence of dust, other physical processes can produce continuum radiation in HII regions: free-free emission, free-bound transitions and two-photon processes.

- Free-free continuum. This emission is produced when free electrons pass close to ions without being captured. This causes a deceleration of the electron scattered by the ions, leading to the emission of electromagnetic radiation known as *Brehmsstrahlung.* This emission involves the transition of the electron from one free kinetic state to another, resulting in a continuum emission extending across the entire electromagnetic spectrum. This component is the strongest at radio wavelengths in an HII region.

- Free-bound continuum or recombination continuum. This continuum is produced during the recapture of a free electron to a bound state of an atom. The free electrons initially have a range of energies, and when they are captured by the atom, produce different discontinuities in the spectrum depending on the level on which they land: the *Balmer discontinuity* (arising from recombinations of free electrons to the level $n = 2$), the *Paschen discontinuity* (arising from recombinations to the level $n = 3$), and so on. These discontinuities appear in the spectrum as an edge followed by a continuum of emission.

- Two-photon process. This is a spontaneous transition into a virtual level between the first two excited states of an atom, which leads to the emission of two photons of total energy equal to the energy of the transition. This double emission has a low probability to occur, but is not negligible in regions where few collisions occur. This continuum emission arises from any metastable excited state and becomes important at ultraviolet wavelengths, where it is stronger than the free-free and free-bound continuum.

Interstellar absorption lines

Another main component of star-forming galaxy spectra is the imprint on the stellar population signal of absorption lines arising from the ISM. The strongest line often arise from the diffuse intercloud medium, where because of the low density, most atoms and ions are in the ground state (lowest-energy level). As a consequence, most atomic or ionic lines observed in the ISM are resonance lines, corresponding to transitions of electrons from the ground state to an excited state. This photo-excitation is generally followed by a fast de-excitation back to the ground state, with an emission of a photon of almost the same wavelength as the incident photon but in any direction; this is known as a *resonant scattering*. These resonance lines are mostly found in the ultraviolet spectral region, because the energy gaps from ground states to first excited states are quite large (although there are a few studied resonance lines in the optical too, such as the Ca H and K lines at 3933.7, 3968.5Å and the Na D lines at 5890.0, 5895.9Å).

It is instructive to recompute the effect on an incident spectrum $F_\nu(0)$ of absorption at the frequency ν caused by an ISM line transition:

$$F_\nu = F_\nu(0)\exp(-\tau_\nu), \tag{1.8}$$

where τ_ν is the line-absorption optical depth, given by:

$$\tau_\nu = \int_0^D k_\nu(ij)\,\mathrm{ds} = \int_0^{\mathrm{D}} \mathrm{a}_\nu(\mathrm{ij})\,\mathrm{n_i}\,\mathrm{ds}, \tag{1.9}$$

where D is the distance over which the absorption takes place, $k_\nu(ij)$ is the volume opacity for transition $i \to j$ (in units of m^{-1}), $a_\nu(ij)$ the absorption cross-section (in m^2) and n_i is the number density of the absorber i. For a line transition from levels i to j the absorption cross-section is given by:

$$a_\nu(ij) = a_0(ij)\,\phi_\nu(s), \tag{1.10}$$

where $\phi_\nu(s)$ is the normalized profile function at position s and $a_0(ij)$ a constant that varies from transition to transition as:

$$a_0(ij) = \frac{c^2}{8\pi\nu^2}\frac{g_j}{g_i}A_{ji}, \tag{1.11}$$

where g_i, g_j are statistical weights for the lower and upper levels of the transition and A_{ji} is the emission transition probability, also known as the Einstein coefficient[10]. When working with absorption lines it is common to consider the oscillator strength instead of the Einstein coefficient.

---

[10] Einstein coefficients are mathematical quantities which are a measure of the probability of absorption or emission of light by an atom or molecule.

They are both related as:

$$A_{ji} = \frac{8\pi^2 e^2 \nu^2}{m_e c^3} \frac{g_i}{g_j} f_{ij}, \tag{1.12}$$

where e is the charge of the electron, and m_e its mass. And Eqs. 1.4.3, 1.4.3, 1.4.3 lead to:

$$a_\nu(ij) = \frac{\pi e^2}{m_e c} f_{ij} \phi_\nu(s), \tag{1.13}$$

Substituting Eq. 1.4.3 into the definition of optical depth (eq. 1.4.3) we have:

$$\tau_\nu = \frac{\pi e^2}{m_e c} f_{ij} \int_0^d \phi_{nu}(s) n_i(s) ds, \tag{1.14}$$

and if ϕ_ν is independent of s:

$$\tau_\nu = \frac{\pi e^2}{m_e c} f_{ij} \phi_{nu} N_i, \tag{1.15}$$

where N_i is the column density of the absorber i, that is the number of particles in a column of unit cross-section from the observer to the background source. It is usually measured in cm^{-2}. Equation 1.4.3 shows that the optical depth (and therefore the line profile) also depends on ϕ_ν, that is the shape of the absorption profile.

The shape of the absorption profile is determined by various physical processes. In particular, the absorption and emission lines are not infinitely narrow because of a number of processes that we can regroup into three categories: microscopic processes, macroscopic ones and instrumental effects. Microscopic processes are broadening mechanisms, which occur at length scales smaller than the photon mean free path (see below). These processes operate on atomic and molecular scales and they change the profile function independently of the number of absorbers. Macroscopic broadening involves the redistribution of absorption through processes that operate on length scales greater than the photon mean path. They do not change the line strength, but they redistribute a fixed amount of absorption to different wavelengths. Finally, instrumental broadening is a form of macroscopic broadening but is usually considered apart as it is not due to any astrophysical effect. For reference, the main microscopic processes that can broaden an absorption line are:

- Natural broadening. This broadening is intrinsic to the transition and comes from the Heisenberg uncertainty principle[11]. It produces a Lorentzian profile.
- Thermal broadening or Doppler broadening. It is due to random thermal motions of the atoms. For a Maxwellian velocity distribution, the 1-D projected velocity distribution is Gaussian.
- Microturbulent broadening. This is an ad hoc description of nonthermal motions that also affect the broadening of the lines. It is generally assumed to have a Gaussian velocity distribution. The total Doppler broadening is simply obtained by adding the thermal and the turbulent velocities in quadrature $v_D^2 = v_{turb}^2 + v_{th}^2$, giving rise to another Gaussian.

The convolution of a Gaussian and a Lorentzian profiles gives a Voigt profile.

---

[11] The Heisenberg uncertainty principle is a variety of mathematical inequalities assessing a fundamental limit to the precision with which certain pairs of physical properties of a particle, known as complementary variables, can be known. The complementary variables that produce the Natural broadening are energy and time.

1.5 Chemical content of a galaxy

The chemical content of a galaxy reflects the past history of that galaxy. Elements are formed in the interior of the stars and pollute the ISM at the final episodes of their lives (see Section 2.1.2). Besides, the elements are formed in various events occurring on different timescales. In particular, thermonuclear reactions inside stars produce elements until Fe, while the rest of the elements are created when type-Ia SNe explode. As anticipated in Section 1.4.1, the timescales of these events are different, type-II (core-collapse) SNe polluting the ISM on short timescales (~ 10 Myr) with light elements, while type-Ia SNe release iron-peak elements on longer timescales (a few $\times 10^8$ yr to ~ 1 Gyr). Therefore we can distinguish two steps in the pollution of the ISM with metals, a first one in which the elements lighter than Fe (α elements) will become part of the ISM, and a posterior pollution with Fe-peak elements through explosions of type-Ia SNe.

This time sequence in the production of α and iron-peak elements implies that the α/Fe element ratio depends on the past Star Formation History (or SFH) of a galaxy. In particular, we can expect young galaxies at very high redshift undergoing their first episodes of star formation to have formed α elements but very few Fe-peak elements, therefore exhibiting significant α/Fe enhancement. In contrast, more evolved galaxies with a smoother SFH are expected to have scaled-solar abundances. Therefore, constraints on chemical abundances are valuable clues to the history of star formation of galaxies.

Interestingly, the stellar populations in different geometric components of star-forming galaxies can also be classified based on metal enrichment: in the Milky Way, the halo population, the bulge population, the thick-disk population and the thin-disk population have different kinematic and chemical-enrichment properties:

- Halo population. These stars have iron abundances $[\mathrm{Fe/H}] \lesssim -1.0$ dex. They lie about 920 pc above the Galactic plane and orbit around it on eccentric and elongated trajectories. This is the region where the oldest stars of the Galaxy live.

- Bulge population. These stars have iron abundances $-1.5 \lesssim [\mathrm{Fe/H}] \lesssim +1.0$. They share kinematic and age properties with the stellar population of the halo.

- Thick-disk population. These are stars have iron abundances in the range $-1.0 \lesssim [\mathrm{Fe/H}] \lesssim -0.6$ dex. They are located between 270 and 920 pc above the Galactic plane and have kinematic properties between those of the halo and thin-disk populations. They are probably younger than the halo population.

- Thin-disk population. These stars have metallicities $[\mathrm{Fe/H}] \gtrsim -0.6$ dex. They are located within 270 pc of the Galactic plane and describe circular orbits. In this region, the stars display a variety of ages, from a few Myr up to ~ 10 Gyr.

1.6 Galaxy spectral energy distributions

The spectral energy distribution of a galaxy is the sum of the contributions from all sources to the light emerging across the electromagnetic spectrum after being transferred through the ISM. At ultraviolet and optical wavelengths, the light is mostly produced by young massive stars (we do not consider here the possible contribution by an active galactic nucleus). These photons can be scattered and absorbed by interstellar dust, which reradiates energy at mid- and far-infrared wavelengths. Older stars tend to dominate the light at red and near-infrared wavelengths. Finally, gas in the ISM both absorbs and produces radiation, giving rise to characteristic absorption- and emission-line features in the spectra. Observationally, there are two main ways of looking at the light emerging from a galaxy: one is to integrate the flux through a filter (photometry); and the other is to disperse the light through a spectrograph to gather more detailed information as a function of wavelength (spectroscopy).

In photometric observations, the light integrated through the filter is expressed in units of magnitude (mag). There are two broadly used systems, based on different zero points, to quantify astronomical flux: the Vega-magnitude and AB-magnitude systems. In general, the flux coming from an object can be expressed as:

$$m = m_0 - 2.5 \log \frac{f_\nu}{f_\nu^0}, \tag{1.16}$$

where m is the apparent magnitude of the object, f_ν the flux convolved with the filter response function (see below), f_ν^0 the filter-convolved flux of the zero-point reference object and m_0 the zero-point of the magnitude system. In the Vega system m_0 is equal to zero for Vega star, the brightest star in the sky.

AB magnitudes are defined with a constant zero-point equal to 3631 Jy[12] in any band, which means $m_0 = 0$ for $f_0 = 3631\,\mathrm{Jy}$, implying:

$$m_{\mathrm{AB}} = -2.5 \log f_\nu - 8.9 \tag{1.17}$$

The logarithmic scale is maintained for historical reasons, due to the response of the eye to light that is almost logarithmical. The actual flux we detect from the object is the convolution of the flux by the filter response function, S_ν, such that:

$$f_\nu = \frac{\int d\nu S_\nu F_\nu}{\int d\nu S_\nu}, \tag{1.18}$$

where F_ν the flux of the object and f_ν is expressed in $\mathrm{ergs\,s^{-1}cm^{-2}Hz^{-1}}$. Here S_ν includes the filter transmission function, the atmosphere transmission and the efficiency of the telescope system.

Spectroscopic observations allow more precise investigations of the stellar and interstellar content of a galaxy by measuring the intensities of absorption and emission lines relative to the continuum level. As described previously, the wavelengths at which these transitions occur are determined by quantum transitions between energy levels of different ions. The strength of an absorption or emission feature is generally measured through the *equivalent width.* The equivalent width is defined as the width of the rectangle that has the height of the continuum level and the same integrated area as the feature under consideration. This can be expressed analytically as:

$$EW = \int_{\lambda_1}^{\lambda_2} d\lambda \left(1 - \frac{F_\lambda}{F_{c,\lambda}}\right) \tag{1.19}$$

where λ_1 and λ_1 are the wavelengths between which the feature is defined, F_λ is the observed flux per unit wavelength and $F_{c,\lambda}$ the continuum level per unit wavelength. Since equivalent widths are defined as flux ratios, they do not depend sensitively on the flux calibration of the observations, although a reliable determination of the continuum level is needed. In practice, this continuum level is not always easy to measure in a region containing many absorption or emission features, which leads to the definition of a *pseudo-continuum* (Worthey, 1994).

---

[12] $1\ \mathrm{Jy} \equiv 10^{-23}\ \mathrm{ergs\,s^{-1}cm^{-2}Hz^{-1}}$.

Stars of different ages and metallicites exhibit different spectral absorption-line signatures, which can be valuable tools to characterize the ongoing and past star-formation episodes in a galaxy. The need for a characterization of such absorption features motivated the definition of optical *spectral indices*. Twenty-five such absorption-line indices were defined at wavelengths in the range range $4000 \lesssim \lambda \lesssim 6000$ Å, and their equivalent widths measured, in the spectra of a large sample of stars observed at Lick Observatory. These Lick Indices were originally developed to break the so-called age-metallicity degeneracy of old stellar populations (Worthey, 1994), but have since also been used to study abundances of α elements relative to iron (Lee & Worthey, 2005) and of other elements (Tripicco & Bell, 1995; Korn et al., 2005).

Similarly, Fanelli et al. (1992) defined 19 ultraviolet absorption-line indices at wavelength in the range $1300 \lesssim \lambda \lesssim 3200$ Å as diagnostics of temperature, luminosity and abundances in the spectra of 218 stars observed with the *International Ultraviolet Explorer*. As in the case of the Lick indices, the Fanelli et al. (1992) indices are defined by means of a central bandpass flanked by two pseudo-continuum bandpasses (see Section 3.2.2). They have been used to derive ages and metallicities of globular clusters in the Galaxy (Chavez et al., 2009) and the Large Magellanic Cloud (LMC) (Maraston et al., 2009).

Another set of spectral indices was defined by Leitherer et al. (2011), who selected strong (stellar and interstellar) absorption-line regions in the spectra of 28 nearby starburst and star-forming galaxies. The indices are defined in bands of between 8 to 40 Å width at wavelengths in the range $1250 \lesssim \lambda \lesssim 2850$ Å. The bands were chosen to be broad enough to include various ranges of velocity dispersions, but not too broad to avoid contamination by a nearby spectral feature.

In this work, I calibrate the predictions of new models for ultraviolet spectral evolution of simple stellar populations using measurements of the Fanelli et al. (1992) indices in the observed spectra of LMC star clusters. These indices seem suitable to study spectra of stars not contaminated by interstellar features, but are less useful for studies of galaxy spectra. The major inconvenience is that these indices are defined in wide (~ 20 Å) windows, in which various interstellar absorption and emission features can overlap with the stellar features (See Section 4.2 for more details). For studies of galactic spectra, a set of indices similar of those proposed by Leitherer et al. (2011) should be more suitable, as the narrower windows in which the features are defined are less sensitive to the inclusion of features of different nature (see Section 4.2.3 for a discussion of different absorption-line indices and their appropriateness for studies of ultraviolet spectra of high-redshift galaxies).

1.7 Future observing facilities

Current observing facilities routinely allow studies of the rest-frame ultraviolet and optical spectral regions of star-forming galaxies out to redshifts $z \sim 1-3$ (see for instance Shapley et al., 2003; Steidel et al., 2010; Stark et al., 2014; Steidel et al., 2016). These galaxy spectra are detected in the near-infrared and have revealed valuable information about different physical processes governing the formation and evolution of galaxies. Detections of spectra at higher redshifts have been limited so far to a few bright lensed sources (Stark et al., 2015a; Stark et al., 2015b; Sobral et al., 2015). Future telescopes such as the *James Webb Space Telescope* (hereafter

JWST) and Extremely Large ground-based Telescopes (ELTs) will be able to observe the spectra of large samples of galaxies out to the reionization epoch and measure the rest-frame ultraviolet emission from bright but also fainter distant sources.

The *JWST*, which is scheduled for launch in 2018, will collect data about the distant Universe for at least five years. The various instruments onboard *JWST* will enable observations at wavelengths in the range 0.6–28 μm with different cameras and spectroscopic capabilities, which will probe the rest-frame optical and ultraviolet emission of large samples of distant galaxies. In particular, the NIRSpec spectrograph will cover the wavelength range between 0.6 and 5 μm at resolutions $R \sim 100$ (prism), 1000 and 2700 (gratings). This will allow the detection of a plethora of features in the continuum spectra of high-redshift galaxies, which will reveal the physical conditions of the pristine star-forming gas and also the chemical composition and evolution of the first stars. To interpret the spectral energy distributions of these distant galaxies, we need to build models including not only high-quality models of young stellar populations, but also the transfer of stellar radiation through the interstellar medium. This is required to account for the influence of gas and dust in the different phases of the ISM on the emergent spectra. The work presented in this thesis has precisely this goal: to develop a physically consistent treatment of stellar emission, nebular emission and interstellar absorption to interpret the entangled signatures of stars and the different phases of the ISM in the ultraviolet spectra of star-forming galaxies.

1.8 Outline

In this thesis, I present a new approach to model in a physically consistent way the competing effects of stellar absorption, nebular emission and interstellar absorption in ultraviolet spectra of star-forming galaxies. I achieve this by combining state-of-the-art models for the production of stellar radiation and its transfer through the ISM to investigate ultraviolet-line diagnostics of stars, the ionized and the neutral ISM in star-forming galaxies.

In Chapter 2, I present the main tools I use in this work. These include the latest version of the stellar population synthesis code GALAXEV and the code CLOUDSPEC, which I use to compute the transfer of stellar radiation through the ISM. This code is a combination of the photoionization code CLOUDY and the general spectrum synthesis code SYNSPEC.

In Chapter 3, I present the calibration I performed of the ultraviolet predictions of the new stellar population synthesis model by means of comparisons with the observed strengths of ultraviolet absorption-line indices in the spectra of 10 young globular clusters in the Large Magellanic Cloud.

In Chapter 4, I present the new approach I have developed to model the combined influence of nebular emission and interstellar absorption on the ultraviolet spectra of star-forming galaxies. This approach builds on an idealized description of the main features of the ISM. As a first application, I study in detail the model spectra of a young, metal-poor galaxy and a more mature, metal-rich galaxy to identify the cleanest ultraviolet tracers of young stars, nebular emission and interstellar absorption.

In Chapter 5, I summarize the main features of the statistical inference tool BEAGLE to interpret galaxy spectra and describe the main mode in which I make use of this code. I also present in Chapter 6 the constraints I derive in this way fitting ultraviolet and optical spectra of galaxies observed with the *Hubble Space Telescope* and the Keck I telescope.

Finally, in Chapter 7, I present my conclusions and mention several ongoing and future projects as a natural continuation of this work.

Chapter 2

Modeling spectral energy distributions of galaxies

In this chapter, I present the main tools I use in this work and their physical bases. These include the latest version of the stellar population synthesis code GALAXEV and the code CLOUDSPEC, which I use to compute the transfer of stellar radiation through the ISM. This code is a combination of the photoionization code CLOUDY and the general spectrum synthesis code SYNSPEC.

Contents

2.1 Stellar emission 24
  2.1.1 Stellar population synthesis codes 24
  2.1.2 Evolutionary tracks 25
  2.1.3 IMF 29
  2.1.4 Stellar spectral libraries 30
2.2 Absorption and emission in the ISM 31
  2.2.1 Photoionization code: CLOUDY 31
  2.2.2 General spectrum synthesis code: SYNSPEC 33
  2.2.3 Summary of the modeling 33
2.3 The star formation history of galaxies 34

In the previous chapter, I showed how the spectrum emerging from a galaxy depends on the emission and absorption of photons of different wavelengths arising in different components of the galaxy. I focus in this thesis mainly on the study of galaxy spectra at ultraviolet and optical (occasionally up to near-infrared) wavelengths, where we can observe several nebular emission and absorption features overlapped with the stellar continuum. In this chapter, I describe the modeling techniques used to compute the light emitted by stars and the transfer of this light through the interstellar medium, including the absorption and emission of photons by ionized and neutral gas. In particular, the standard way of computing the emission from stars is to appeal to a stellar population synthesis code. Then, a photoionization code can be used to compute photon transfer through the interstellar medium. Finally, we can compute ISM absorption features using a general spectrum synthesis code to solve the radiative transfer equation given the element opacities previously calculated with the photoionization code. In this work, I make use of the latest version of the GALAXEV (Bruzual & Charlot, 2003) stellar population synthesis code and CLOUDSPEC (Hubeny et al., 2000), which combines the lastest version of the photoionization code CLOUDY (Ferland et al., 2013b) with the spectral-synthesis code SYNSPEC (Hubeny & Lanz, 1995, 2011). In the following sections, I present an overview of these codes and their ingredients.

2.1 Stellar emission

In the wavelength range considered in this work, from ultraviolet to near-infrared wavelengths, stars are the main contributors to the total light emission from a galaxy. The stellar continuum shape and spectral features allow one to characterize diverse physical properties of the stellar population, such as age, metallicity, star formation history, etc. The most common way to interpret the integrated light of a galaxy or a star cluster is to compare it with models of the spectral evolution of stellar populations. These models can be used to compute the emission from simple stellar populations (SSPs; whose stars are all born at the same time) for various ages, metallicities and prescriptions for the stellar Initial Mass Function (IMF, see Section 2.1.3). The spectral evolution of such SSPs can be used to interpret observations of individual star clusters and also be convolved with different star formation histories (SFHs, see Section 2.3) to compute the spectral evolution of entire galaxies.

2.1.1 Stellar population synthesis codes

The first attempts to interpret galaxy spectra in the early 70's relied on fitting observed spectral energy distributions with linear combinations of individual stellar spectra of various spectral types and luminosity classes (Spinrad & Taylor, 1971; Faber, 1972). This technique required one to constrain too many free parameters and therefore was abandoned a decade later. Present-day models are based on an approach called *evolutionary population synthesis*, which invokes a more restricted set of main adjustable parameters: the stellar IMF, the SFH and the chemical enrichment history (Tinsley, 1978; Bruzual A., 1983; Arimoto & Yoshii, 1987; Guiderdoni & Rocca-Volmerange, 1987; Buzzoni, 1989; Bressan et al., 1994; Worthey, 1994; Leitherer & Heckman, 1995; Fioc & Rocca-Volmerange, 1997; Maraston, 1998; Vazdekis, 1999; Bruzual & Charlot, 2003; Conroy & Gunn, 2010). Most recent evolutionary population synthesis models rely on the *isochrone synthesis technique* (Charlot & Bruzual, 1991), based on the principle that any galaxy can be expanded into a series of chemically homogeneous instantaneous bursts, or SSPs, for which isochrones can be computed at any age from stellar evolution tracks in the Hertzsprung-Russell diagram (Section 2.1.2).[1] Evolutionary population synthesis models are the general tool used to interpret galaxy spectra at ultraviolet, optical and near-infrared wavelengths in terms of constraints on stellar population properties.

---

[1] A few models (e.g., Maraston, 1998, 2005) rely on another technique called *fuel consumption theorem* to compute the spectral evolution of SSPs in the Hertzsprung-Russell diagram.

In this work, I adopt the latest version of the GALAXEV stellar population synthesis code (Charlot & Bruzual, 1991; Bruzual & Charlot, 2003) to compute the spectral evolution of stellar populations using the isochrone synthesis technique. In this approach, the luminosity per unit wavelength per unit mass produced at time t by an SSP of metallicity Z can be expressed as (e.g. Conroy et al., 2009):

$$S_\lambda(t, Z) = \int_{M_{lo}}^{M_{up}} \phi(m)\, \Lambda \left[L_{bol}(m, Z, t),\, T_{eff}(m, Z, t),\, Z\right] dm, \tag{2.1}$$

where m is the initial (zero-age main sequence, ZAMS) stellar mass, $\phi(m)$ is the IMF, M_{lo} and M_{up} are the lower and upper mass cutoffs of the IMF and $\Lambda\left[L_{bol}(m, Z, t),\, T_{eff}(m, Z, t),\, Z\right]$ is a spectrum from the stellar library of mass m, effective temperature $T_{eff}(m, Z, t)$, bolometric luminosity $L_{bol}(m, Z, t)$ and metallity Z. M_{lo} is generally chosen to correspond to the lower mass limit for H-burning ignition in the stellar core (about 0.08–0.09 $\mathrm{M}_\odot$ for $Z = Z_\odot$), while M_{up} can take different values depending on the evolutionary tracks included for massive stars.

Once the spectral evolution of any SSP is known, the luminosity per unit wavelength produced by a galaxy at time t can be computed as:[2]

$$L_\lambda(t) = \int_0^t \psi(t - t')\, S_\lambda[t', Z(t - t')]\, dt', \tag{2.2}$$

where $\psi(t - t')$ and $Z(t - t')$ are the star formation rate and metallicity of newly-born stars at time $t - t'$.

The main ingredients to assemble the SSP models, which consist in a prescription for stellar evolution, the IMF and stellar spectral libraries, are described in the following sections.

2.1.2 Evolutionary tracks

An isochrone locates stars in a full mass range with fixed age and metallicity in the Hertzsprung-Russell (HR) diagram, defined by stellar bolometric luminosity $L_{bol}(m, Z, t)$ and effective temperature $T_{eff}(m, Z, t)$. The construction of isochrones requires a library of stellar evolutionary tracks characterizing the evolution of the luminosity and effective temperature of a star of any given initial mass and chemical composition as a function of age. Figure 2.1 shows the positions of a few known Milky-Way stars on the ZAMS and in more advanced stages of evolution in the HR diagram. Stars of different initial masses evolve in different ways and with different lifetimes, although all stars spend about 90% of their life on the main sequence (MS). Stellar lifetime increases with decreasing initial mass. This is because a more massive star needs to produce a larger amount of thermonuclear energy to counterbalance the gravitational force of its mass and maintain hydrostatic equilibrium. Therefore, it is more luminous and also exhausts its hydrogen reservoir faster than a less massive star. When hydrogen is exhausted, which marks the end of MS evolution, the subsequent evolution of a star depends on its mass.

---

[2] Here we neglect the transfer function of the light through the ISM for the sake of clarity. See Section 4.1.1 for the actual luminosity of the galaxy when accounting for this effect.

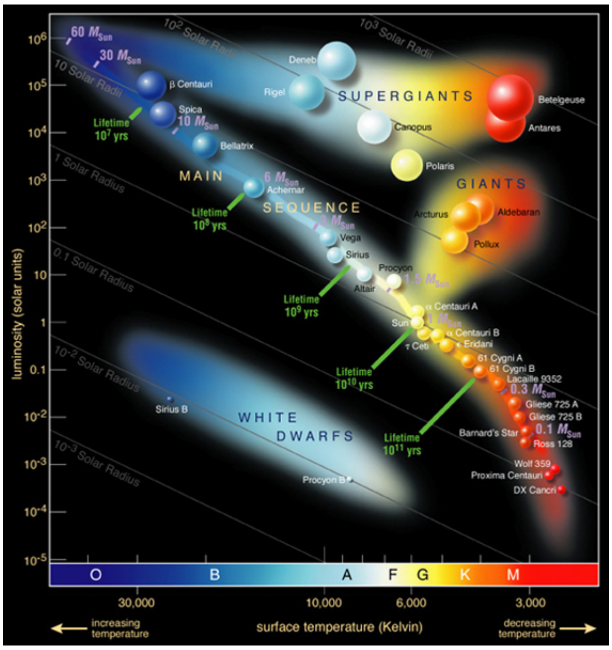

Figure 2.1 – HR diagram showing the positions of several known Milky-Way stars. Credit: Wikipedia.

- **Low-mass stars:** These are stars with masses smaller than the upper mass limit for the formation of an electron-degenerate He-core at the end of MS evolution, i.e. about 2.2 $M_\odot$ at solar metallicity. Among these low-mass stars, we can find stars with masses smaller than the lower mass for H-burning ignition in the stellar core ($M \lesssim 0.08 - 0.09$ $M_\odot$ for $Z = Z_\odot$), which never burn hydrogen and whose luminosity is due to the gravitational energy produced in their slow cooling contraction. They burn light elements, such as Li and D, and when they run out, the pressure from degenerate electrons counterbalances the gravitational force. They are called brown dwarfs and are relevant to the chemical enrichment of galaxies because they do not pollute with metals the cloud of gas out of which they formed.

  Stars with masses in the range $0.09 \lesssim M \lesssim 0.5$ $M_\odot$ ignite core-hydrogen burning, but their helium core becomes electron-degenerate before getting hot enough to burn helium. Their high density prevents radiative transfer of the energy in the star, which is instead transported via thermal conduction. These stars evolve as white dwarfs and have lifetimes much larger than the present age of the universe.

  Stars with masses in the range $0.5 \lesssim M \lesssim 2.2$ $M_\odot$ that have consumed H in their core start to burn it in a shell outside the He core. This is because once a main-sequence star ceases core-H burning, the core begins to collapse, increasing its temperature, and hydrogen is able to fuse in a shell outside the core via the CNO cycle. This occurs in a phase known as *Sub-Giant Branch* (SGB), at almost constant luminosity.

  The He-core mass continues to grow due to external H-burning, and the star very slowly expands as the hydrogen shell migrates outwards. The increase in mass of the core produces a contraction, which translates into an increase of temperature including in the H-burning shell. This causes the hydrogen shell to fuse more rapidly and therefore the star to become more luminous, larger, and somewhat cooler. This is the ascent of the *Red Giant Branch* (RGB). During this phase, an important event occurs, called the *first dredge-up*, when the outer convective envelope becomes deep enough to bring CNO-fusion products to the surface from the formerly convective core. This episode changes the surface abundances of He, C, N and O.

At the end of the RGB phase, stars in this mass range ignite He in an electron-degenerate core in an explosive event called the Helium flash. Helium ignition occurs when the core temperature reaches about 10^8 K. The energy released by helium fusion causes the core to expand, slowing down hydrogen fusion in the surrounding layers and making the radiative pressure drop. The drop in energy production causes the star to contract, making the luminosity also drop until the beginning of the *Horizontal Branch* (HB). During this phase, low-mass stars burn He in their core and H in an outer shell, gradually shrinking in radius and increasing the surface temperature. This happens in a region of the HR diagram populated by two important types of variable stars: RR-Lyrae and Cepheid stars. It is interesting to mention why these stars pulsate: when the star contracts, the density and temperature of the He II layer increases. At a temperature around 35,000–50,000 K, He II can be ionized into He III, which increases stellar opacity and helps the energy flux from the interior to be effectively absorbed. The temperature of the star then rises again, causing it to expand. The expansion makes the temperature drop and He III recombine into He II, reducing stellar opacity, while the outer layers contract, and a new pulsation cycle starts.

When a star in this mass range has consumed all its central helium, the core (now mainly composed by C and O) contracts and heats up, becoming mildly degenerate, while He burning ignites in a shell. This causes an expansion of the shell, which extinguishes the outer H-burning layer, lowering the surface temperature of the star. The star enters the *Asymptotic Giant Branch* (AGB), parallel to the RGB in the HR diagram. During the AGB ascent, a deep convective layer forms (due to the expansion and cooling of the H-rich layer) and brings C from the core to the surface: this is the *second dredge-up*. The He-burning shell keeps moving outwards in search for He, eventually reaching the H/He discontinuity. At this point, He-burning ceases, the star contracts, and gravitational energy re-ignites the H-burning shell. This is the start of the *Thermally-Pulsing AGB* (TP-AGB) phase. The H-burning shell accumulates He above the degenerate CO core, but when the He mass exceeds ~ 0.1 M$_\odot$, a thermonuclear explosion takes place, causing the external layers to expand and suppressing the H-burning shell. Once He is exhausted, the star contracts again and re-ignites the H-burning shell, which starts accumulating He again above the CO core, and so on. This double shell-burning phase produces thermal pulses. There can be from a few to hundreds of pulses, depending on the mass and metallicity of the star. During this phase, stars with masses in the range $1.2 \lesssim M \lesssim 1.5$ M$_\odot$ may also undergo a *third dredge up*. The pulses cause the expulsion of the outer layers of the star, which can drive a strong wind. The expelled gas expands in a shell called *circumstellar envelope* and cools as it moves away from the star, allowing dust particles and molecules to form. Eventually, the star loses most of the H-rich envelope through a *super-wind* phase and ends up burning H only in thin shell near the external layers. This does not produce enough He to trigger new pulses, and the stellar temperature rises. If the temperature is high enough ($T \sim 30,000$ K), the ejected material is ionized, producing a *Planetary Nebula* (PN). When the outer H-burning shell runs out of fuel, nuclear reactions cease because the temperature in the CO core is not high enough to ignite C burning. The PN surrounds a central extremely hot star, which cools down as a white dwarf. Enrichment of the ISM with metals processed by such stars occurs during the HB, AGB and PN phases.

- **Intermediate mass stars:** These are stars with masses high enough to ignite He non degenerately, but too low to avoid the development of an electron-degenerate CO core after He exhaustion. Their masses lie in the range $2.2 \lesssim M \lesssim 8$ M$_\odot$ for $Z = Z_\odot$. After He ignition, these stars evolve in a way similar to that of low-mass stars, only faster,

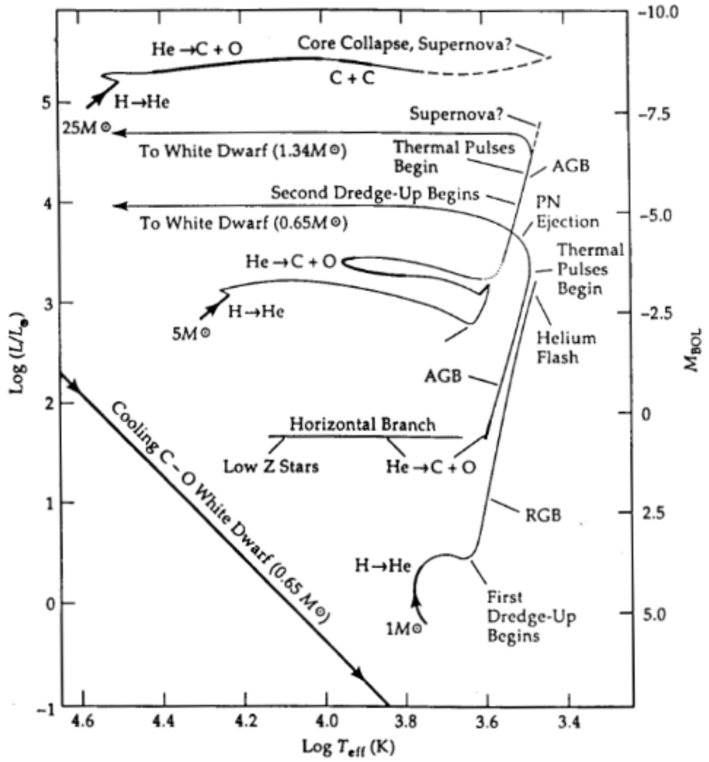

Figure 2.2 – Schematic representation of the evolution of stars with different initial masses in the HR diagram. Credit: Iben & Tutukov (1985)

until they reach the AGB. Then, if the CO core fed by the He-burning shell reaches the Chandrasekhar limit of ~ 1.4 $M_\odot$, the pressure from degenerate electrons can no longer sustain the gravitational force, triggering a thermonuclear explosion. This can lead either to a disintegration of the core or to successive flashes of carbon burning. However, these events are rare, because a large fraction of the mass of even the most massive intermediate-mass stars is lost to the ISM through super-winds at the end of the TP-AGB, which prevents the CO core to reach the Chandrasekhar limit. The evolution ends when a super-wind finally expels the stellar envelope. The pressure of degenerate electrons prevents the contraction of the CO core, inhibiting carbon ignition. Thereafter, all nuclear reactions stop, and the star cools as a CO white dwarf.

- **Massive stars:** Stars with masses $M \gtrsim 8$ $M_\odot$ do not develop an electron-degenerate CO core. Their evolution is similar to that of intermediate- and low-mass stars until core-He exhaustion. As the density of the CO core is smaller than in lower-mass stars, the core is non-degenerate and therefore contracts raising its temperature. At temperatures above 10^9 K, C burning is able to ignite in the core. When central C is exhausted, the core contracts further raising its temperature, until Ne burning eventually ignites, while a C-burning layer moves outward. Subsequent concentric layers of burning elements form during this phase, which sees the production of s-elements, such as Ba and Sr, until the core is composed of Fe. Iron has one of the highest binding energies per nucleon of all elements, implying that fission is more likely than fusion to transform it. When iron forms in the core, therefore, the lack of thermonuclear energy to counterbalance the gravitational force triggers an uncontrolled core collapse, while a shock disintegrates the envelope in a type-II supernova event. This explosion pollutes the medium around the star with α-capture elements (Si, O, Mg, etc.), because the Fe-peak elements remain in the stellar remnant, which can be either a neutron star (for stars with initial masses $M \lesssim 20\ \mathrm{M}_{\odot}$) or a black-hole (for more massive stars). An interesting class of massive stars are Wolf-Rayet stars. These stars undergo huge mass loss and eventually lose their hydrogen/helium envelope during their evolution. They go through the main nuclear burning phases until the formation of an iron core, after which they explode as type-Ib or Ic supernovae. The stellar population synthesis code used in this work incorporates state-of-the-art evolutionary tracks of massive stars from (Bressan et al., 2012; Chen et al., 2015, see Section 3.2.1 for more details).

2.1.3 IMF

The relative numbers of stars of different masses along an isochrone in the HR diagram determine the weights of these stars in the integrated spectral energy distribution of the SSP. The initial mass function $\phi(m)$ is traditionally defined in such a way that $\phi(m)dm$ is proportional to the number of stars born with masses between m and $m + dm$. The first empirical determination of the IMF for stars more massive than the Sun was achieved by Edwin Salpeter (Salpeter, 1955), who approximated this function as a single power law:

$$\phi(m)\,\mathrm{dm} \propto \mathrm{m}^{-\alpha} \tag{2.3}$$

with index $\alpha = 2.35$. Several authors have since proposed other parametrizations of the IMF (e.g. Miller & Scalo, 1979; Kennicutt, 1983; Scalo, 1986; Kroupa et al., 1993; Kroupa, 2001; Baldry & Glazebrook, 2003; Chabrier, 2003). Several of these functions are shown in Fig. 2.3.

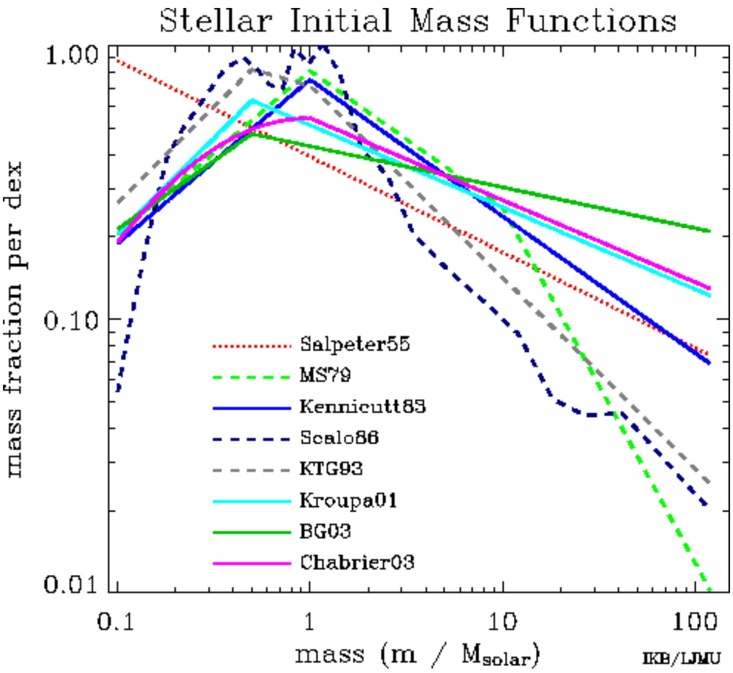

Figure 2.3 – Different IMFs. Credit: http://www.astro.ljmu.ac.uk/ ikb/research/imf-use-in-cosmology.html

In this work, I adopt the Chabrier (2003) IMF, defined as:

$$\phi[\log(m)] \propto \begin{cases} \exp\left[-\frac{(\log m - \log m_c)^2}{2\sigma^2}\right] & \text{for } 0.1 \leq m < 1.0 \ \mathrm{M}_\odot\,; \\ m^{-1.3} & \text{for } m \geqslant 1.0 \ \mathrm{M}_\odot\,, \end{cases}$$

with $m_c = 0.08$ and $\sigma = 0.69$. We also need to specify the lower and upper IMF cutoffs, M_{lo} and M_{hi}. The default value for M_{lo} is of 0.1 $\mathrm{M}_\odot$, close to the lower mass limit for H-burning ignition on the main sequence (Section 2.1.2). For simplicity, M_{up} is often taken to be 100 $\mathrm{M}_\odot$, although here we explore values between 60 and 300 $\mathrm{M}_\odot$, as M_{up} can influence the ultraviolet spectrum of a galaxy, in particular the Hα/ultraviolet luminosity ratio and the profiles of strong wind lines, such as C IV 1550Å and Si IV 1400Å (Bastian et al., 2010, see also Section 4.2.4).

The sampling of the IMF is also important in stellar population synthesis models. For star clusters more massive than 10^4–10^5 $\mathrm{M}_\odot$, the IMF is fully populated up to the highest masses, while in lower-mass clusters, the effects of stochastic IMF sampling can become important (e.g., Bruzual & Charlot, 2003). To compute a stellar population model in this case, we follow the prescription of Bruzual (2002) and construct a probability distribution function $g(N)$, such as the probability of occurrence of the random variable N' within dN equals that of the random variable m' within dm:

$$|\phi(m)dm| = |g(N)dN|\,, \tag{2.4}$$

where N is a single-valued function of m expressed as:

$$N(m) = \int_{m_l}^{m} \phi(m')dm', \tag{2.5}$$

which is a cumulative distribution function giving the probability that the mass m' be lower than or equal to m. Assuming that the function $\phi(m)$ is normalized to unity, it follows that:

$$g(N) = 1, \quad 0 \leq N \leq 1\,. \tag{2.6}$$

Therefore, $g(N)$ is a uniform distribution for which any value in the range $0 \leq N \leq 1$ is equally likely. We can also compute the value of m corresponding to a given N. For example, in the case of the power-law IMF of equation (2.1.3), we have:

$$m = [(1-N)m_l^{1-\alpha} + N m_u^{1-\alpha}]^{-\frac{1}{\alpha-1}}\,. \tag{2.7}$$

If we sample N randomly between 0 and 1, the values of m computed using equation (2.1.3) will provide the desired stochastic sampling of the IMF.

We will return to stochastic IMF sampling (using the Chabrier 2003 IMF) in Section 3.2.3, where we explore how this can affect the ultraviolet, optical and near-infrared spectra of stellar populations, and in Section 3.3.3, where we discuss the consequences for ultraviolet-based estimates of age, metallicity and stellar mass in a small sample of LMC star clusters.

2.1.4 Stellar spectral libraries

The last ingredient we require to compute integrated spectra of stellar populations is a library of individual stellar spectra. There are two classes of libraries, observational and theoretical:

- **Observational libraries:** These are compilations of observed spectra of as many types of stars as possible with different luminosity classes and spectral types. Some of these widely used libraries are PICKLES (Pickles, 1998), ELODIE (Prugniel & Soubiran, 2001), STELIB (Le Borgne et al., 2003), UVES POP (Jehin et al., 2005), MILES (Sánchez-Blázquez et al., 2006; Cenarro et al., 2007; Prugniel et al., 2011), INDOUS/CFLIB (Valdes et al., 2004), NGSL (Gregg et al., 2004), XSL (Chen et al., 2011) and IRTF (Rayner et al., 2009). These observations require good spectral resolution so they are restricted to nearby stars of the Milky Way (isolated and in open or globular clusters) or nearby galaxies such as the LMC. This implies that to extend the library to a wider parameter space, for example including less chemically enriched stars, we need to rely on theoretical models.

- **Theoretical libraries:** A main advantage of these libraries is that they can be computed over full wavelength ranges for large distributions of stellar parameters (for example, at far-ultraviolet wavelengths, where observational libraries are poorly sampled). The computation of a theoretical spectrum requires one to first compute a model atmosphere (providing the solution to the hydrodynamic equations of the gas) and then run a line-synthesis code (to convert the flux coming from the model atmosphere into a stellar spectrum). Popular theoretical spectral libraries include UVBLUE (Bertone et al., 2008), WM-BASIC (Pauldrach et al., 1986), POWR (Gräfener et al., 2002; Hamann & Gräfener, 2003; Hamann et al., 2006; Sander et al., 2012; Hainich et al., 2014), ATLAS9 (Kurucz, 1970), CMFGEN (Hillier & Miller, 1998), MARCS (Gustafsson et al., 1975) and PHOENIX (Hauschildt et al., 1997). These synthetic models also present some disadvantages, for example often the lack of precise spectro-photometric calibration (Martins & Coelho, 2007).

The stellar population synthesis code that I use in this work relies on a combination of several of these spectral libraries. In particular, the code appeals whenever possible to the observational MILES library at optical wavelengths (Sánchez-Blázquez et al., 2006; Cenarro et al., 2007; Prugniel et al., 2011). To extend the predictions at ultraviolet wavelengths, the code appeals to the theoretical spectral libraries UVBLUE (Bertone et al., 2008), TLUSTY (Hubeny & Lanz, 1995; Lanz & Hubeny, 2003, 2007) and POWR (Gräfener et al., 2002; Hamann & Gräfener, 2003; Hamann et al., 2006; Sander et al., 2012; Hainich et al., 2014). In Section 3.2.1, I describe in more detail the stellar spectral libraries adopted in this work.

2.2 Absorption and emission in the ISM

In this thesis, I am interested in computing in a physically consistent way the combined influence of nebular emission and interstellar absorption on the ultraviolet spectra of star-forming galaxies. I achieve this through an idealized description of the main features of the ISM (inspired from Fig. 1.5) and by appealing to a combination of the photoionization code CLOUDY (version 13.3; Ferland et al. 2013a) with the spectral synthesis code SYNSPEC (Hubeny & Lanz, 1995), which allows the computation of interstellar-line strengths based on the ionization structure solved by CLOUDY (in practice, this combination is performed via the program CLOUDSPEC of Hubeny et al. 2000; see also Heap et al. 2001). I describe this approach in Chapter 4. To this end, it is useful here to briefly review the main features of the CLOUDY and SYNSPEC codes.

2.2.1 Photoionization code: CLOUDY

The aim of photoionization codes is to simulate the physical conditions describing the ionization structure of ionized nebulae. In general, codes of this kind include photoionization, recombination, free-free radiation, collisional excitation, collisional ionization and charge exchange reactions. Most codes use static photoionization solvers, which assume that the gas is in both ionization and thermal equilibrium (although some codes are built to study nebulae not in equilibrium; see Tylenda 1979; Marten & Schoenberner 1991). The basic equations on which a photoionization code relies to compute a model are the radiative transfer equation, the ion equilibrium equation and energy conservation.

In this work, I use the CLOUDY code (Ferland et al., 1998, 2013b) to compute the physical conditions in H II and H I regions around young stars. This is one of the most widely used photoionization codes, although other codes have been proposed, among which NEBU (Pequignot et al., 1978), ION (Netzer & Ferland, 1984) and MAPPINGS (Sutherland & Dopita, 1993). These codes differ mainly in their approach to compute the transfer of ionizing photons, in particular to describe: the *on the spot* reabsorption, where the photons are reabsorbed near the location at which they were emitted; the outward-only approximation, which adds the locally-produced diffuse radiation to the incident flux and transfers this in different directions; and the *full treatment*, whereby the inward and outward diffuse radiation are computed in a single averaged direction. Also, some codes include Monte-Carlo techniques to solve the transfer of radiation (Och et al., 1998). Another difference we can find between different codes is in the treatment of geometry. Most codes assume spherical or plane-parallel 1D geometries. However, some other codes are also built in 3D, which increases the number of free parameters, complicating the modeling but treating the distribution of densities in the cloud in a more realistic way (Gruenwald et al., 1997; Morisset, 2006). It is also important for photoionization codes to keep their atomic databases up to date, as measurements of different processes of atomic physics are improved constantly. Finally, we note that several codes were designed to model shocks induced by winds of ionizing stars, which requires to treat simultaneously hydrodynamic and microphysics processes (Schmidt-Voigt & Koeppen, 1987; Marten & Schoenberner, 1991; Frank & Mellema, 1994; Mellema & Frank, 1995; Mellema, 1995; Rodriguez-Gaspar & Tenorio-Tagle, 1998).

The latest version of the CLOUDY code I adopt in this work (Ferland et al., 2013b) presents several improvements over previous versions, in particular, in the techniques used to compute dusty molecular environments, the ionization and chemistry solvers and also the treatment of atomic data (Ferland et al., 2013b). CLOUDY is a microphysics code. Its goal is to simulate physical conditions in clouds covering wide ranges of temperature and density. It calculates in a self-consistent way the physical conditions (distributions of temperature, density and ionization) and the resulting spectrum across a cloud ionized by an input radiation field. This is achieved by simultaneously solving the equations of statistical and thermal equilibrium, which balance ionization-neutralization processes and heating-cooling processes, respectively. I am interested in the emission and absorption spectra of the H II and H I regions surrounding young stellar populations in galaxies. The parameters I use for this modeling are described in Section 4.1.1.

The output of a CLOUDY calculation includes the predicted thermal, ionization, and chemical structures of the cloud. To compute the emergent spectrum, CLOUDY divides the cloud into a set of thin concentric shells chosen to have thicknesses small enough for the physical conditions across them to be nearly constant. In each of these layers, the transmitted radiation field is the net emission emerging from the shielded face of the cloud. It includes both the attenuated incident and the diffuse radiation fields. This is summarized in Fig. 2.4, which displays the scheme of a CLOUDY calculation. I assume spherical geometry in my calculations. In this case, CLOUDY takes into account ionization by the diffuse continua and lines produced on the far side of the nebula (beyond the central object) and does not attenuate the ionizing continuum by pure scattering opacities, such as electron scattering, back scattering by grains and Rayleigh scattering.

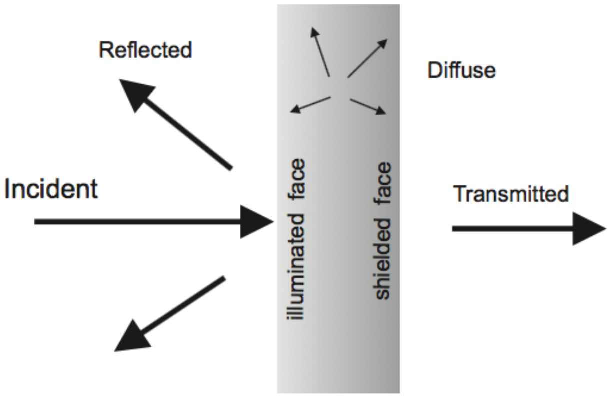

Figure 2.4 – Scheme of CLOUDY calculation in each of the concentric shells modeled around an ionizing source. Credit: Hazy (CLOUDY)

In addition to transmitted continuum radiation and emission-line intensities, CLOUDY computes element opacities in the medium surrounding the ionizing source, which are a key element for a posterior calculation of the absorption spectrum. To compute this spectrum, I rely on the SYNSPEC code, which stores the element opacities computed by CLOUDY in the different layers of the medium and solves the radiative transfer equation along the line of sight. A brief description of this code is given in the following Section.

2.2.2 General spectrum synthesis code: SYNSPEC

SYNSPEC is a general spectrum synthesis code (Hubeny & Lanz, 2011). Other examples of spectrum synthesis codes are SPECTRUM (Gray & Corbally, 1994) and SYNTH3 (which includes a molecular equilibrium solver; Kochukhov 2007). When used as a standalone program, SYNSPEC takes as input a model atmosphere, such as TLUSTY (Hubeny, 1988; Lanz & Hubeny, 2003) or KURUCZ (Kurucz, 1992). Then, it reads a comprehensive line list and selects the lines contributing to the total opacity, based on the physical parameters of the model atmosphere. Finally, SYNSPEC solves the radiative transfer equation in a specified wavelength range at a given spectral resolution. When SYNSPEC is called from CLOUDSPEC, the model atmosphere used is that of TLUSTY and the lines contributing to the opacity are calculated previously with CLOUDY.

For the purpose of this thesis, I call SYNSPEC from CLOUDSPEC and use as input a stellar population spectrum from GALAXEV. I compute the absorption at wavelengths between 1200 and 4000 Å. The code also allows one to convolve absorption-line profiles with a user-supplied velocity field. In Chapter 4, I describe the way in which I compute nebular emission and ISM absorption with these tools. I also mention in Chapter 7 ongoing and future work aiming to study the impact of velocity fields on ultraviolet interstellar absorption features.

2.2.3 Summary of the modeling

To summarize, I model the different components of the galaxies relying on different codes. To model stellar emission, I use GALAXEV. Then, I use CLOUDSPEC to model nebular emission and ISM absorption. In doing so, I can produce different types of output spectra, shown in Fig. 2.5, and described in Chapter 4.

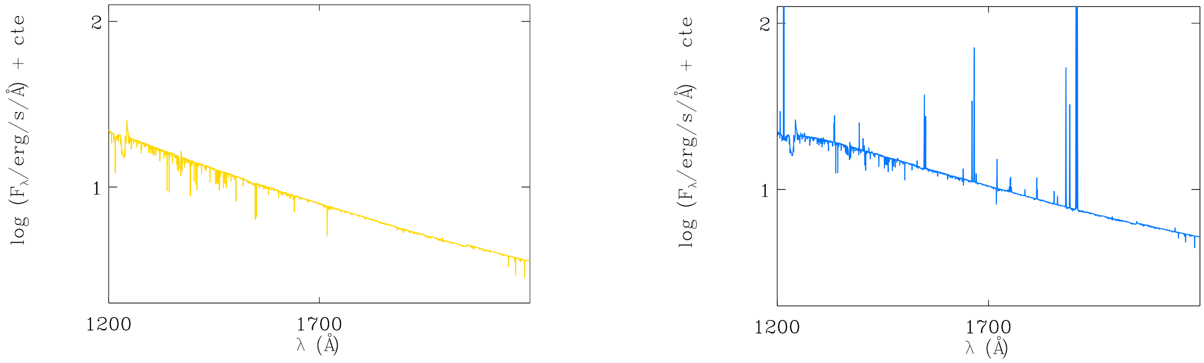

(a) Emission from the stars, computed with GALAXEV.

(b) Nebular emission and stellar continuum, computed with CLOUDY (CLOUDSPEC).

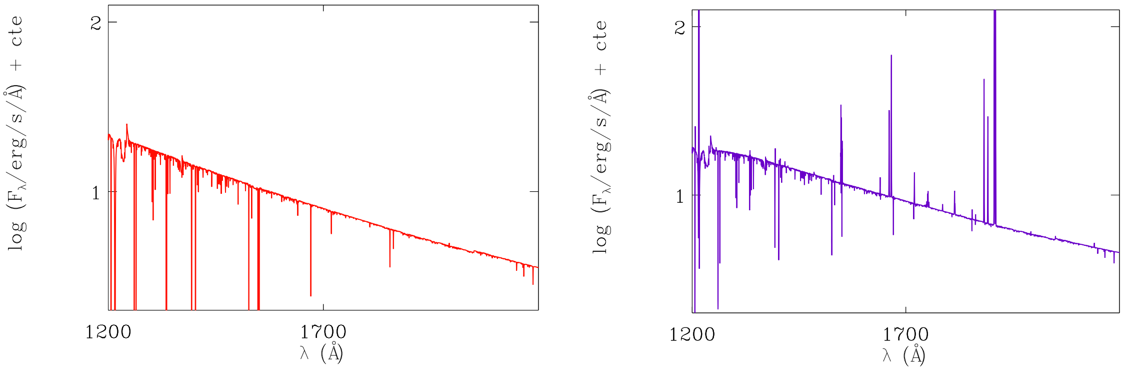

(c) Absorption of the stellar continuum by the ISM, computed with SYNSPEC (CLOUDSPEC).

(d) Nebular emission, ISM absorption and stellar continuum, computed with CLOUDSPEC.

Figure 2.5 – Different models computed with GALAXEV and CLOUDSPEC, the codes used in this work to model stellar emission and its transfer through the ISM.

2.3 The star formation history of galaxies

The appearance of a galaxy at a given time results from a combination of different physical processes acting on different timescales, such as star formation, chemical enrichment of the ISM, mergers and AGN feedback. All these processes are related to the Star Formation History of the galaxy. The SFH is therefore an important ingredient of the interpretation of observed galaxy spectra using spectral evolution models. Some popular analytic functions include:

- Constant star formation rate, $\psi(t)$ =const;

- Exponentially declining star formation rate: $\psi(t) = \exp(-t/\tau)$, where τ is the star formation timescale;

- Delayed star formation rate: $\psi(t) = t\ \exp(-t/\tau)$.

SFHs in spectral analyses may also be taken from sophisticated simulations of galaxy formation (e.g., Pacifici et al., 2012). According to Eq. 2.2, we can describe the spectral evolution of a galaxy with the spectral evolution of simple stellar populations. As an example, we show in Fig. 2.6 the spectrum of a simple stellar population at different ages and solar metallicity computed with GALAXEV. The plot shows how at early ages the emission of young and massive stars dominates the ultraviolet region and how as the population evolves and these stars leave the MS, the peak of emission moves towards the optical and near infrared. After a few Gyr, the emission from hot post-AGB stars makes the ultraviolet emission rise again and remain roughly constant at greater ages.

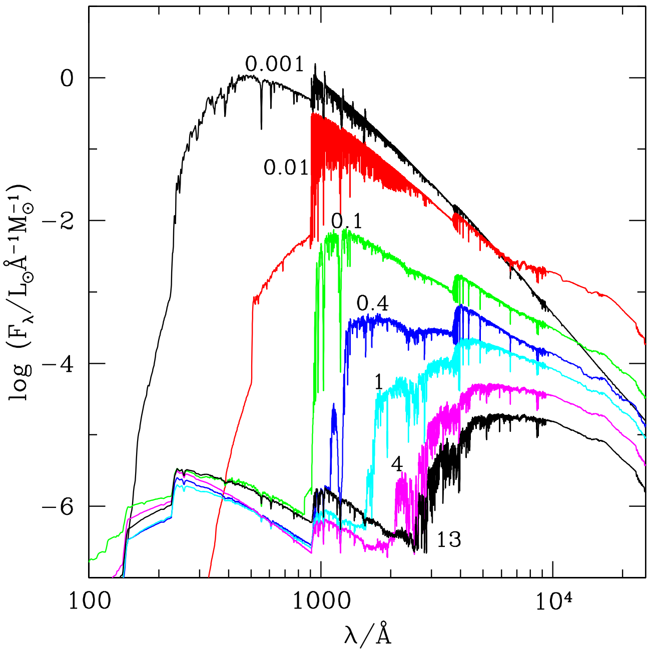

Figure 2.6 – Spectral evolution of the standard SSP model for solar metallicity. Ages are indicated next to the spectra (in Gyr).Credit: Bruzual & Charlot (2003)

In this work, I am primarily interested in the emission at ultraviolet wavelengths, where young massive stars dominate the light. This is why I adopt constant star formation rates and young instantaneous bursts to model galaxies at high redshifts. In Chapter 5, I explain how I use the BEAGLE tool to interpret, in Chapter 6, galaxy spectral distributions and to characterize the SFHs and other physical parameters of these galaxies. In some cases (see Section 6.3) the adoption of a constant star formation rate does not fit the data satisfactorily, and in such cases, the preferred SFH is delayed star formation rate. See Chapter 6 for more details about spectral fitting and the derivation of physical parameter.

Chapter 3

Calibration of the SSP models in the ultraviolet

In this chapter, I present the calibration of the ultraviolet predictions of the new stellar population synthesis models I have adopted in this thesis against the observed strengths of ultraviolet absorption-line indices in the spectra of 10 young globular clusters in the Large Magellanic Cloud. This chapter is extracted from the paper submitted to MNRAS entitled *Modelling ultraviolet-line diagnostics of stars, the ionized and the neutral interstellar medium in star-forming galaxies.*

Contents

3.1 Introduction 38
3.2 Ultraviolet signatures of young stellar populations 40
  3.2.1 Stellar population synthesis modelling 40
  3.2.2 Ultraviolet spectral indices 41
  3.2.3 Dependence of index strength on age, metallicity and integrated stellar mass 41
  3.2.4 Associated broadband magnitudes 46
3.3 Interpretation of ultraviolet star-cluster spectroscopy 46
  3.3.1 Observational sample 46
  3.3.2 Model library 48
  3.3.3 Age, metallicity and stellar-mass estimates 49

3.1 Introduction

The ultraviolet spectral energy distributions of star-forming galaxies exhibit numerous spectral signatures of stars and gas in the ionized and neutral ISM. The ability to interpret these features in the spectra of star-forming galaxies has received increasing interest with the possibility, offered by new-generation ground-based telescope and the future (*JWST*), to sample the rest-frame ultraviolet emission from large samples of young galaxies out to the epoch of cosmic reionization.

Several major observational studies have focused on the interpretation of ultraviolet galaxy spectra in terms of constraints on stellar and interstellar properties. Most studies of low-redshift galaxies are based on data from the *International Ultraviolet Explorer* (*IUE*), the *Hubble Space Telescope* (*HST*), the *Hopkins Ultraviolet Telescope* (*HUT*) and the *Far Ultraviolet Spectroscopic Explorer* (*FUSE*), while those of high-redshift galaxies rely on deep ground-based infrared spectroscopy. Ultraviolet absorption lines from stellar photospheres and winds often used to characterise young stellar populations, chemical enrichment and stellar IMF in galaxies include the prominent Si IV $\lambda\lambda 1394, 1403$ and C IV $\lambda\lambda 1548, 1551$ lines, but also H-Lyβ, O VI $\lambda 1035$, C II $\lambda 1036$ and N V $\lambda\lambda 1238, 1242$ (e.g., González Delgado et al., 1998; Pettini et al., 2000; Mehlert et al., 2002, 2006; Halliday et al., 2008). Fanelli et al. (1992) define around 20 absorption-line indices at wavelengths in the range $1200 \lesssim \lambda \lesssim 3200$ Å in the *IUE* spectra of 218 nearby stars. Leitherer et al. (2011) propose a complementary set of 12 indices over a similar wavelength range based on *HST* observations of 28 local starburst and star-forming galaxies, which also includes interstellar absorption lines (see also Section 1.6). In fact, interstellar absorption lines are routinely used to characterise the chemical composition and large-scale kinematics of the ionized and neutral ISM in star-forming galaxies, among which Si II $\lambda 1260$, O I $\lambda 1302$, Si II $\lambda 1304$, C II $\lambda 1335$, Si IV $\lambda\lambda 1394, 1403$, Si II $\lambda 1526$, and C IV $\lambda\lambda 1548, 1551$, but also Fe II $\lambda 1608$, Al II $\lambda 1671$, Fe II $\lambda 2344$ and Fe II $\lambda 2383$ (e.g., Pettini et al., 2000, 2002; Sembach et al., 2000; Shapley et al., 2003; Steidel et al., 2010; Lebouteiller et al., 2013; James et al., 2014). The physical conditions in the ionized gas can also be traced using the luminosity of emission lines, such as H-Lyα, C IV $\lambda\lambda 1548, 1551$, He II $\lambda 1640$, O III]$\lambda\lambda 1661, 1666$, [Si III]$\lambda 1883$+Si III]$\lambda 1892$ and [C III]$\lambda 1907$+C III]$\lambda 1909$ (e.g., Shapley et al., 2003; Erb et al., 2010; Christensen et al., 2012; Stark et al., 2014, 2015a; Sobral et al., 2015). So far, however, combined constraints on the neutral and ionized components of the ISM derived from the ultraviolet emission of a galaxy have generally been performed using independent (and hence potentially inconsistent) estimates of the chemical compositions of both components (e.g., Thuan et al., 2002, 2005; Aloisi et al., 2003; Lebouteiller et al., 2004, 2009; Lee & Skillman, 2004; Lebouteiller et al., 2013).

On the theoretical front, the ultraviolet spectral modelling of galaxies has been the scene of important progress over the past two decades. Early spectral synthesis models relied on libraries of observed *IUE* and *HST* spectra of O and B stars in the Milky Way, the Small and the Large Magellanic Clouds (LMC; e.g., Leitherer et al., 1999; Leitherer et al., 2001). The restricted range in stellar (in particular, metallicity and wind) parameters probed by such spectra triggered the development of increasingly sophisticated libraries of synthetic spectra (e.g., Hauschildt & Baron, 1999; Hillier & Miller, 1999; Pauldrach et al., 2001; Lanz & Hubeny, 2003, 2007; Hamann & Gräfener, 2004; Martins et al., 2005; Puls et al., 2005; Rodríguez-Merino et al., 2005, see Section 2 of Leitherer et al. 2010 for a description of the different types of model atmosphere calculations). These theoretical libraries have enabled the exploration of the dependence of selected ultraviolet spectral indices on stellar effective temperature, gravity, metallicity and, for massive stars, wind parameters (controlling P-Cygni[1] line profiles). Chavez et al. (2007, 2009) identify 17 near-ultraviolet spectral diagnostics in the wavelength range $1900 \lesssim \lambda \lesssim 3200$ Å, which they exploit to constrain the ages and metallicities of evolved Galactic globular clusters. Other studies have focused on the exploration of a small number of stellar metallicity diagnostics of star-forming galaxies at far-ultraviolet wavelengths, over the range $900 \lesssim \lambda \lesssim 2100$ Å (Rix et al., 2004; Sommariva et al., 2012, see also Faisst et al. 2016). A challenge in the application of these metallicity diagnostics to the interpretation of observed spectra is the required careful determination of the far-ultraviolet continuum in a region riddled with absorption features. This difficulty is avoided when appealing to indices defined by two 'pseudo-continuum' bandpasses flanking a central bandpass (e.g., Fanelli et al., 1992; Chavez et al., 2007). Maraston et al. (2009) compare in this way the strengths of the Fanelli et al. (1992) indices predicted by their models for young stellar populations (based on the stellar spectral library of Rodríguez-Merino et al. 2005) with those measured in the *IUE* spectra of 10 LMC star clusters observed by Cassatella et al. (1987). Maraston et al. (2009) however do not account for the fact that these clusters have small stellar masses, between about 3×10^3 and 7×10^4 $M_\odot$ (Mackey & Gilmore, 2003; McLaughlin & van der Marel, 2005), and hence, that stochastic IMF sampling can severely affect integrated spectral properties (e.g., Fouesneau et al., 2012). A more general limitation of the use of ultraviolet spectral diagnostics to interpret observed galaxy spectra is that no systematic, quantitative estimate of the contamination of these diagnostics by interstellar emission and absorption has been performed yet.

---

[1] See Appendix C for an explanation of the formation of a P-Cygni profile.

In this work, I use a combination of state-of-the-art models for the production of radiation by young stellar populations and its transfer through the ionized and the neutral ISM to investigate diagnostics of these three components in ultraviolet spectra of star-forming galaxies. I start by using the latest version of the Bruzual & Charlot (2003) stellar population synthesis code (Charlot & Bruzual, in preparation; which incorporates the ultraviolet spectral libraries of Lanz & Hubeny 2003, 2007; Hamann & Gräfener 2004; Rodríguez-Merino et al. 2005; Leitherer et al. 2010) to investigate the dependence of the Fanelli et al. (1992) ultraviolet spectral indices on age, metallicity and integrated stellar mass, for simple (i.e. instantaneous-burst) stellar populations (SSPs). I demonstrate the ability of the models to reproduce observations and assess the extent to which accounting for stochastic IMF sampling can change the constraints on age, metallicity and stellar mass derived from the *IUE* spectra of the Cassatella et al. (1987) clusters. On these grounds, I develop a simple approach to compute in a physically consistent way the combined influence of nebular emission and interstellar absorption on the ultraviolet spectra of star-forming galaxies. I achieve this through an idealized description of the main features of the ISM (inspired from the dust model of Charlot & Fall 2000) and by appealing to a combination of the photoionization code CLOUDY (version 13.3; Ferland et al. 2013a, see also Section 2.2.1 for a summary of the novelties included in this last release) with the spectral synthesis code SYNSPEC[2] (see, e.g. Hubeny & Lanz, 2011, and also Section 2.2.2), which allows the computation of interstellar-line strengths based on the ionization structure solved by CLOUDY (in practice, this combination is performed via the program CLOUDSPEC of Hubeny et al. 2000; see also Heap et al. 2001 and also Section 2.2). I use this approach to investigate the ultraviolet spectral features individually most sensitive to young stars, the ionized and the neutral ISM. I find that, aside from a few notable exceptions, most standard ultraviolet indices defined in the spectra of ISM-free stellar populations can potentially suffer significant contamination by the ISM, especially at high metallicity. I also identify several nebular-emission and interstellar-absorption features, which stand out as particularly clean tracers of the different phases of the ISM. Beyond an a posteriori justification of the main spectral diagnostics useful to characterise young stars, the ionized and the neutral ISM, the models presented in this thesis provide a means of simulating and interpreting in a versatile and physically consistent way the entangled contributions by these three components to the ultraviolet emission from star-forming galaxies.

I present the model I adopt to compute the ultraviolet emission from young stellar populations in Section 3.2, where I investigate the dependence of the Fanelli et al. (1992) ultraviolet spectral indices on age, metallicity and integrated stellar mass for SSPs. In Section 3.3, I use this model to interpret the *IUE* spectra of the 10 LMC star clusters observed by Cassatella et al. (1987) and assess potential biases in age, metallicity and stellar-mass estimates introduced through the neglect of stochastic IMF sampling. I present a new approach to model the influence of nebular emission and interstellar absorption on the ultraviolet spectra of star-forming galaxies in Section 4. I analyse in detail two representative models of star-forming galaxies: a young, metal-poor galaxy and a more mature, metal-rich galaxy. I use these models to identify ultraviolet spectral indices individually most sensitive to stars, the ionized and the neutral ISM.

---

[2] `http://nova.astro.umd.edu/Synspec49/synspec.html`

3.2 Ultraviolet signatures of young stellar populations

In this Section, I start by describing the main features of the stellar population synthesis code I adopt to compute ultraviolet spectral signatures of young stellar populations (Section 3.2.1). Then, I briefly review the main properties of the Fanelli et al. (1992) ultraviolet spectral indices (Section 3.2.2). I examine the dependence of index strengths on age, metallicity and integrated stellar mass for simple stellar populations (Section 3.2.3), along with the dependence of ultraviolet, optical and near-infrared broadband magnitudes on integrated stellar mass (Section 3.2.4).

3.2.1 Stellar population synthesis modelling

I adopt the latest version of the Bruzual & Charlot (2003) stellar population synthesis code (Charlot & Bruzual, in preparation; see also Wofford et al. 2016) to compute emission from stellar populations of ages between 10^4 yr and 13.8 Gyr at wavelengths between 5.6 Å and 3.6 cm, for metallicities in the range $0.0001 \leq Z \leq 0.04$ (assuming scaled-solar heavy-element abundance ratios at all metallicities). This version of the code incorporates updated stellar evolutionary tracks computed with the PARSEC code of Bressan et al. (2012) for stars with initial masses up to 350 $\mathrm{M}_\odot$ (Chen et al., 2015), as well as the recent prescription by Marigo et al. (2013) for the evolution of thermally pulsing AGB stars (see Section 2.1.2). The present-day solar metallicity in these calculations is taken to be $Z_\odot = 0.01524$ (the zero-age main sequence solar metallicity being $Z^0_\odot = 0.01774$; see Bressan et al. 2012). Note that the inclusion of very low-metallicity, massive stars is important to investigate the properties of primordial stellar populations (Bromm & Yoshida, 2011).

These evolutionary tracks are combined with various stellar spectral libraries to describe the properties of stars of different effective temperatures, luminosities, surface gravities, metallicities and mass-loss rates in the Hertzsprung-Russell diagram (see Section 2.1.4). For the most part (see adjustments below), the spectra of O stars hotter than 27,500 K and B stars hotter than 15,000 K are taken from the TLUSTY grid of metal line-blanketed, non-local thermodynamic equilibrium (non-LTE), plane-parallel, hydrostatic models of Hubeny & Lanz (1995); Lanz & Hubeny (2003, 2007). The spectra of cooler stars are taken from the library of line-blanketed, LTE, plane-parallel, hydrostatic models of Martins et al. (2005), extended at wavelengths shorter than 3000 Å using similar models from the UVBLUE library of Rodríguez-Merino et al. (2005). At wavelengths in the range $3525 \lesssim \lambda \lesssim 7500$ Å, the spectra of stars with effective temperatures in the range $2800 \lesssim T_\mathrm{eff} \lesssim 36,000$ K are taken from the observational MILES library of Sánchez-Blázquez et al. (2006). At wavelengths in the range $900 \lesssim \lambda \lesssim 3000$ Å, the spectra of MS stars with effective temperatures in the range $17,000 \lesssim T_\mathrm{eff} \lesssim 60,000$ K are taken from the theoretical library of Leitherer et al. (2010), computed using the WM-basic code of Pauldrach et al. (2001) for line-blanketed, non-LTE, spherically extended models including radiation driven winds. Finally, for Wolf-Rayet stars, the spectra are taken from the (high-resolution version of the) PoWR library of line-blanketed, non-LTE, spherically expanding models of Hamann & Gräfener (2004, see also Gräfener et al. 2002; Hamann & Gräfener 2003; Hamann et al. 2006; Sander et al. 2012; Hainich et al. 2014). The inclusion of the Leitherer et al. (2010) and Hamann & Gräfener (2004) spectral libraries enables the modelling of P-Cygni line profiles originating from winds of massive OB and Wolf-Rayet stars in the integrated ultraviolet spectra of young stellar populations (for example, for the N V $\lambda1240$, Si IV $\lambda1400$ and C IV $\lambda1550$ lines; e.g. Walborn & Panek 1984). For completeness, the spectra of the much fainter, hot post-AGB stars are taken from the library of line-blanketed, non-LTE, plane-parallel, hydrostatic models of Rauch (2002).

3.2.2 Ultraviolet spectral indices

To investigate the ultraviolet properties of young stellar populations, I appeal to the set of spectral indices originally defined by Fanelli et al. (1992) in the *IUE* spectra of 218 nearby stars spanning spectral type from O through K and iron abundances (available for only 94 stars) in the range $-1.12 \lesssim [\mathrm{Fe/H}] \lesssim 0.56$. I focus on the 19 absorption-line indices defined by means of a central bandpass flanked by two pseudo-continuum bandpasses.[3] This includes 11 far-ultraviolet indices, with central wavelengths in the range $1300 \lesssim \lambda \lesssim 1850\,\text{Å}$, and 8 mid-ultraviolet indices, with central wavelengths in the range $2400 \lesssim \lambda \lesssim 3100\,\text{Å}$. As advanced in Section 1.6 (see eq. 1.19), I compute the equivalent width of an absorption-line index in a spectral energy distribution defined by a flux per unit wavelength F_λ following Trager et al. (1998):

$$EW = \int_{\lambda_1}^{\lambda_2} d\lambda \left(1 - \frac{F_\lambda}{F_{c,\lambda}}\right) , \tag{3.1}$$

where λ_1 and λ_2 are the wavelength limits of the central feature bandpass and $F_{c,\lambda}$ is the pseudo-continuum flux per unit wavelength, defined through a linear interpolation between the average fluxes in the blue and red flanking bandpasses.

For reference, I list in Table 3.1 the definitions by Fanelli et al. (1992) of the 19 ultraviolet absorption-line indices used in this work, along with an indication of the atomic species thought to contribute most to each feature (according to, in particular, Fanelli et al., 1992; Chavez et al., 2007; Maraston et al., 2009; Leitherer et al., 2011). It is worth recalling that the three index definitions for the C IV line, which exhibits a strong P-Cygni profile in O-type stars (Walborn & Panek, 1984), are centred on absorption feature (C IV$^{\mathrm{a}}$), the central wavelength (C IV$^{\mathrm{c}}$) and emission feature (C IV$^{\mathrm{e}}$) of that line. I refer the reader to Appendix A for a more detailed description of the properties of these indices and of the dependence of their strengths on stellar spectral type and luminosity class. In general, far-ultraviolet indices tend to be dominated by hot O- and B-type stars, while near-ultraviolet indices tend to be stronger in cooler, A- to K-type stars.

3.2.3 Dependence of index strength on age, metallicity and integrated stellar mass

Chavez et al. (2007) and Maraston et al. (2009) have investigated the dependence of the Fanelli et al. (1992) index strengths on stellar effective temperature, gravity and metallicity, as well as on the age and metallicity of the integrated spectra of SSPs. It is useful to start by examining the predictions of the new stellar population synthesis models described in Section 3.2 for the dependence

---

[3] The use of a pseudo-continuum in the definition of these indices is dictated by the ~ 6Å resolution of *IUE* spectra (Boggess et al., 1978), which does not enable reliable measurements of the true continuum.

Table 3.1 – Definition of 19 ultraviolet spectral indices in terms of a central bandpass flanked by two pseudo-continuum bandpasses (from tables 4A and 4B of Fanelli et al., 1992). The rightmost column indicates the main atomic species responsible for each feature (Fanelli et al., 1992; Chavez et al., 2007; Leitherer et al., 2011).

Name[a]	Blue bandpass	Central bandpass	Red bandpass	Δ(EW/Å)[b]	Features[c]
Bl 1302	1270–1290	1292–1312	1345–1365	−0.87	Si II, Si III, C III, O I
Si IV 1397	1345–1365	1387–1407	1475–1495	−0.47	Si IV
Bl 1425	1345–1365	1415–1435	1475–1495	0.00	Si III, Fe V, C II, C III
Fe 1453	1345–1365	1440–1466	1475–1495	0.00	Ni II, Co II
C IV^{a}	1500–1520	1530–1550	1577–1597	−0.41	Si II*, C IV
C IV^{c}	1500–1520	1540–1560	1577–1597	−0.65	C IV
C IV^{e}	1500–1520	1550–1570	1577–1597	−0.23	C IV
Bl 1617	1577–1597	1604–1630	1685–1705	0.00	Fe II, C III
Bl 1664	1577–1597	1651–1677	1685–1705	−0.64	C I, C I*, O III], Fe V, Al II
Bl 1719	1685–1705	1709–1729	1803–1823	0.06	Ni II, Fe IV, N IV, Si IV
Bl 1853	1803–1823	1838–1868	1885–1915	−0.11	Si I, Al II, Al III
Fe II 2402	2285–2325	2382–2422	2432–2458	−0.87	Fe I, Fe II, Co I
Bl 2538	2432–2458	2520–2556	2562–2588	0.55	Fe I, Fe II, Mg I, Cr I, N I
Fe II 2609	2562–2588	2596–2622	2647–2673	−0.56	Fe I, Fe II, Mn II
Mg II 2800	2762–2782	2784–2814	2818–2838	−2.24	Mg II, Fe I, Mn I
Mg I 2852	2818–2838	2839–2865	2906–2936	−0.48	Mg I, Fe I, Fe II, Cr II
Mg wide	2470–2670	2670–2870	2930–3130	−2.72	Mg I, Mg II, Fe I, Fe II, Mn I, Cr I, Cr II
Fe I 3000	2906–2936	2965–3025	3031–3051	0.00	Fe I, Fe II, Cr I, Ni I
Bl 3096	3031–3051	3086–3106	3115–3155	0.00	Fe I, Al I, Ni I, Mg I

[a] Indices originally qualified as blends of several species are labelled with 'Bl'.

[b] Term to be added to the measured index strength to correct a posteriori for contamination by Milky-Way ISM absorption lines (Section 3.3.1 and Appendix B). A zero entry indicates that no strong ISM absorption line affects the bandpasses defining this index.

[c] **A * symbol indicates a fine-structure transition.**

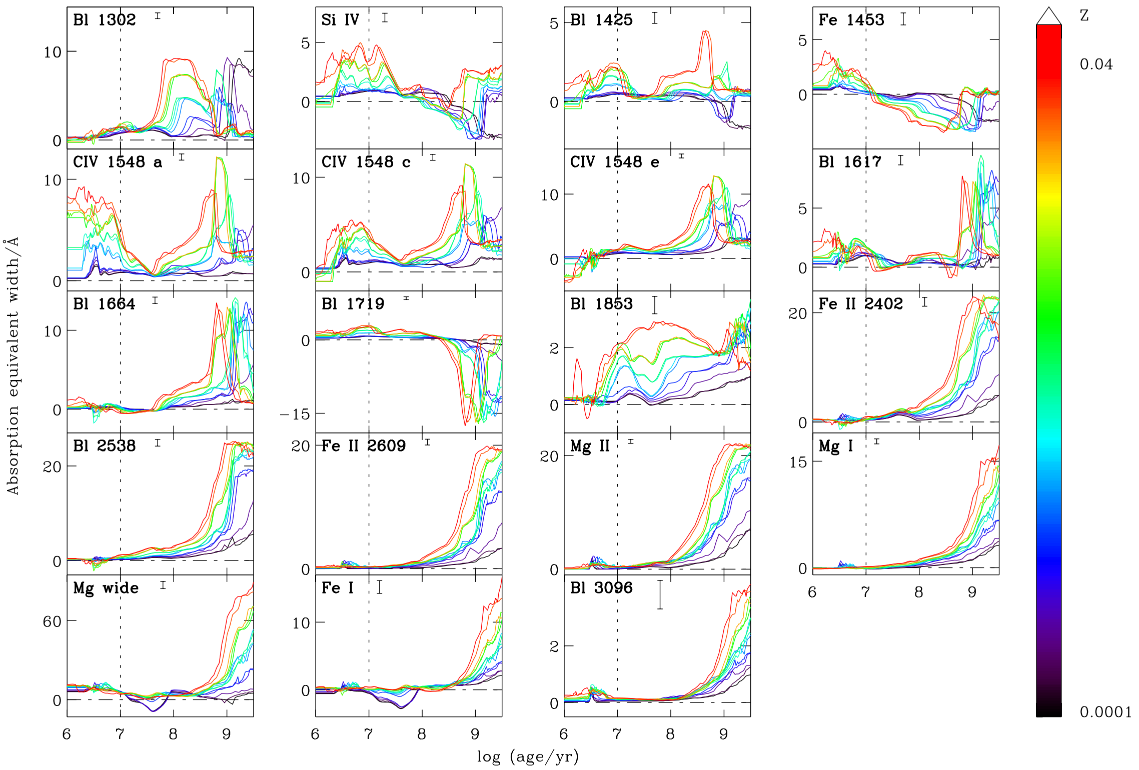

Figure 3.1 – Strengths of the 19 Fanelli et al. (1992) ultraviolet spectral indices defined in Table 3.1 plotted against age, for SSPs with a smoothly sampled Chabrier (2003) IMF and metallicities $Z = 0.0001$, 0.0002, 0.0005, 0.001, 0.002, 0.004, 0.006, 0.008, 0.010, 0.014, 0.017, 0.02, 0.03 and 0.04, colour-coded as indicated on the right-hand scale (for clarity, the ordinate scale in each panel has been adjusted to reflect the dynamic range spanned by the strength of the corresponding index). Also shown next to the index name in each panel is the typical measurement error in the *IUE* spectra of the LMC clusters observed by Cassatella et al. (1987). In each panel, the dotted vertical line marks the age of 10 Myr, before which nebular emission can strongly affect index strengths (see text).

of index strength on SSP age and metallicity. Fig. 3.1 shows the time evolution of the strengths of the 19 ultraviolet spectral indices in Table 3.1, for SSPs with 14 different metallicities in the range $0.0001 \leqslant Z \leqslant 0.04$ and a smoothly sampled Chabrier (2003) IMF. Also indicated in each panel is the typical measurement error in the corresponding index strength in the *IUE* spectra of the LMC star clusters observed by Cassatella et al. (1987, see Section 3.3.1 below). Since star clusters generally form in dense molecular clouds, which dissipate on a timescale of about 10 Myr (e.g. Murray et al., 2010; Murray, 2011), stellar absorption lines of SSPs younger than this limit are expected to be strongly contaminated by nebular emission from the H II regions carved by newly-born stars within the clouds (Section 4.1). I therefore focus for the moment on the evolution of ultraviolet index strengths at ages greater than 10 Myr (i.e. to the right of the dotted vertical line) in Fig. 3.1.

The results of Fig. 3.1 confirm those obtained using previous models by Chavez et al. (2007) and Maraston et al. (2009), in that the strengths of most absorption-line indices tend to increase with metallicity – because of the stronger abundance of absorbing metals – with a few exceptions in some age ranges. The most notable exception is Fe 1453, for which an inversion in the dependence of index strength on metallicity occurs at an age around 10 Myr. This is associated with a transition from positive to negative equivalent widths, induced by the development of a strong absorption blend affecting the red pseudo-continuum bandpass of this index. A similar absorption of the pseudo-continuum flux is also responsible for the negative equivalent widths of, e.g., Si IV 1397, Bl 1425 and Bl 1719 at ages around 1 Gyr. A main feature of Fig. 3.1 is that, overall, the age range during which the dependence of an index strength on metallicity is the strongest tends to increase with wavelength, from ages between roughly 3×10^7 and 3×10^8 yr for Bl 1302 to ages greater than about 1 Gyr for Bl 3096. This is because, as the stellar population ages, stars of progressively lower effective temperature dominate the integrated ultraviolet emission, implying a shift in strong absorption features from the far to the mid ultraviolet (Section 3.2.2). It is also important to note that, at ages greater than about 1 Gyr, the ultraviolet emission from an SSP is dominated by hot post-AGB stars, whose contribution is orders of magnitude fainter than that of massive stars at young ages (see, e.g., fig. 9 of Bruzual & Charlot, 2003).

As mentioned in Section 3.1, an important issue when appealing to SSP models to interpret observations of individual star clusters is that, for integrated stellar masses less than about 10^5 $\mathrm{M}_{\odot}$, stochastic IMF sampling can severely affect the integrated spectral properties of the clusters (e.g., Bruzual & Charlot, 2003; Fouesneau et al., 2012). I investigate this by computing the ultraviolet spectral properties of stellar populations with different integrated stellar masses, using an approach similar to that described by Bruzual (2002, inspired from Santos & Frogel 1997). Given an age and a metallicity, this consists in drawing stars randomly from the IMF until a chosen integrated SSP mass is reached[4] (see Section 2.1.3). Fig. 3.2 shows the dispersion in the strengths of the 19 Fanelli et al. (1992) indices for SSPs with integrated stellar masses $M_{\mathrm{cl}} = 5 \times 10^2$ (cream), 1×10^4 (teal blue) and 2×10^5 $\mathrm{M}_{\odot}$ (indian red) and a stochastically sampled Chabrier (2003) IMF, at ages between 1 Myr and 3 Gyr, for a fixed metallicity $Z = 0.017$. This was obtained by performing, at each age, 1100 realisations of SSPs for each of these three target stellar masses. Note that, because of the large dispersion in some age ranges, the ordinate scale in a given panel in Fig. 3.2 generally spans a wider dynamic range than in the corresponding panel in Fig. 3.1.

Fig. 3.2 shows some important results. Firstly, as expected, the dispersion in index strength generally tends to increase from large to small SSP mass M_{cl}, as the presence of a single massive bright star can affect more strongly the integrated emission from a low-mass than a high-mass stellar population. A most remarkable result from Fig. 3.2 is that, while the dispersion in index

---

[4] In building up the integrated stellar mass of an SSP at a given age, I account for the loss of mass returned to the ISM by evolved stars in the form of winds and supernova explosions (this was not considered by Santos & Frogel 1997 and Bruzual 2002).

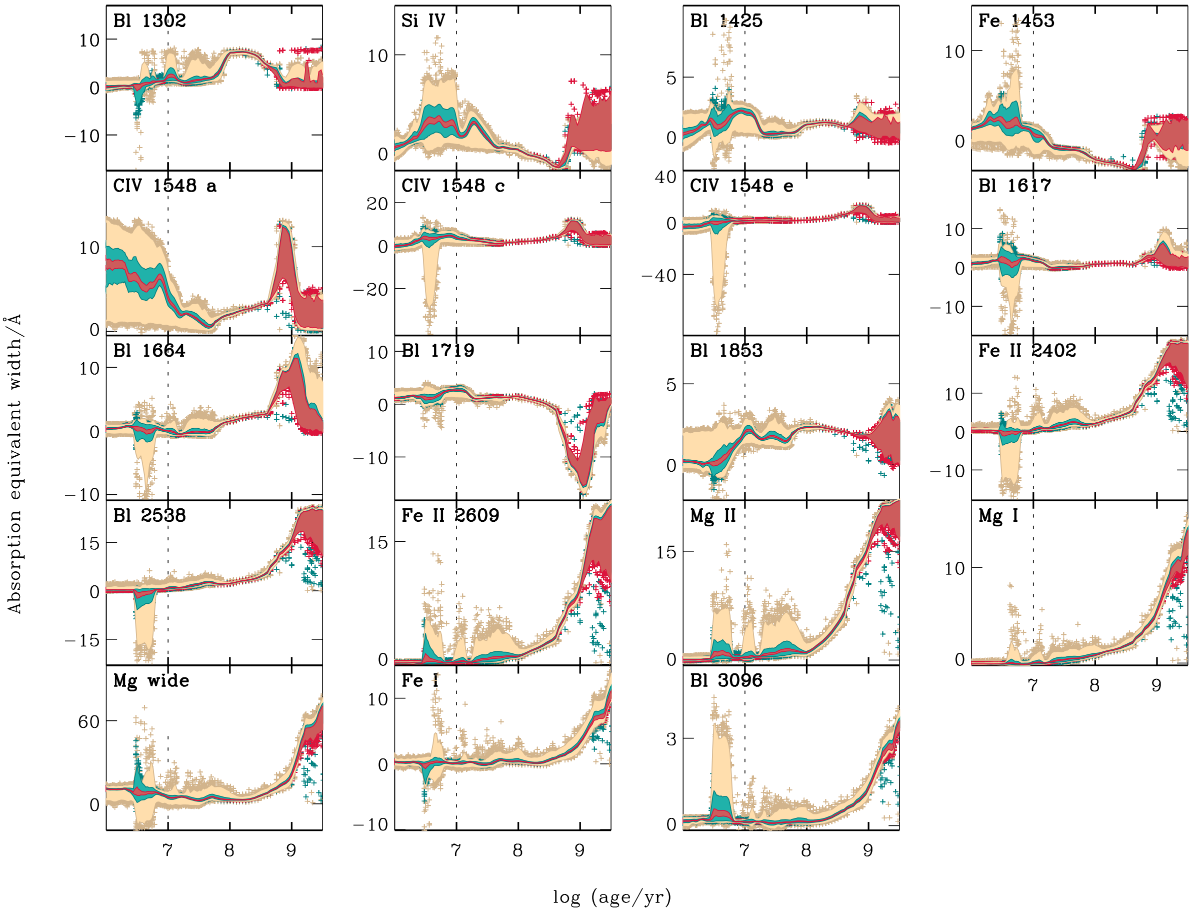

Figure 3.2 – Strengths of the 19 Fanelli et al. (1992) ultraviolet spectral indices defined in Table 3.1 plotted against age, for SSPs with a stochastically sampled Chabrier (2003) IMF and integrated stellar masses $M_{\mathrm{cl}} = 5 \times 10^2$ (cream), 1×10^4 (teal blue) and 2×10^5 $\mathrm{M}_\odot$ (indian red), for the metallicity $Z = 0.017$ (for clarity, the ordinate scale in each panel has been adjusted to reflect the dynamic range spanned by the strength of the corresponding index). In each panel, the filled area shows the range spanned by 99 per cent of 1100 SSP realisations with these three target stellar masses at each age, while crosses show the remaining 1 per cent of most distant outliers. The dotted vertical line has the same meaning as in Fig. 3.1.

strength can be very large at ages below ∼10 Myr and above ∼500 Myr, it is generally more moderate at ages in between. This is because, at the youngest ages, the integrated ultraviolet light can be strongly influenced by the occasional presence of rare, very massive, hot, short-lived stars, while at ages greater than a few hundred million years, it can be strongly influenced by the emergence of more numerous, but extremely short-lived, hot post-AGB stars. At ages in the range from ∼10 Myr to ∼500 Myr, therefore, the impact of stochastic IMF sampling on age and metallicity estimates of star clusters from ultraviolet spectroscopy should be moderate. I find that this is even more true at metallicities lower than that of $Z = 0.017$ adopted in Fig. 3.2 (not shown), since, as illustrated by Fig. 3.1, index strengths tend to rise with metallicity. As I shall see in Section 3.3.3, despite this result, stochastic IMF sampling can affect stellar-mass estimates of star clusters more significantly than age and metallicity estimates at ages between ∼10 Myr to ∼500 Myr.

3.2.4 Associated broadband magnitudes

Mass estimates of observed stellar populations require an absolute flux measurement[5] in addition to that of a spectral energy distribution. For this reason, I show in Fig. 3.3 the broadband magnitudes of the same models as in Fig. 3.2, computed through the *Galaxy Evolution Explorer* (*GALEX*) FUV and NUV, Sloan Digital Sky Survey (SDSS) *ugriz* and Two-Micron All-Sky Survey (2MASS) JHK_{S} filters. Again, as expected, the dispersion in integrated spectral properties induced by stochastic IMF sampling increases from the most massive (indian red) to the least massive (cream) model. Also, consistently with the findings in Fig. 3.2, the dispersion in ultraviolet magnitudes in Fig. 3.3 is largest at ages below ∼10 Myr and above ∼500 Myr, although a difference with respect to ultraviolet spectral indices is that the dispersion in magnitude can still be substantial at ages in between, for small M_{cl}. Fig. 3.3 further shows that the effect of stochastic IMF sampling increases from ultraviolet to near-infrared magnitudes. This is because stars in nearly all mass ranges experience a bright, rapid, cool (red supergiant or AGB) phase at the end of their evolution, whose influence on integrated near-infrared spectral properties can be strongly affected by stochastic IMF sampling. I have also examined the predictions of models with different M_{cl} similar to those in Fig. 3.3, but for metallicities lower than $Z = 0.017$ (not shown). The properties of such models are qualitatively similar to those of the models in Fig. 3.3, except that low-metallicity models run at brighter magnitudes, as the deficiency of metals in stellar atmospheres reduces the ability for stars to cool and hence fade (e.g. Bressan et al., 2012).

3.3 Interpretation of ultraviolet star-cluster spectroscopy

In this Section, I use the stellar population models presented in the previous Section to interpret ultraviolet spectroscopic observations of a sample of young LMC star clusters. My main goals are to assess the ability of the models to reproduce the strengths of the Fanelli et al. (1992) indices in observed cluster spectra and to quantify the influence of stochastic IMF sampling on age, metallicity and stellar-mass estimates.

3.3.1 Observational sample

To assess the reliability of the ultraviolet spectral synthesis models present in Section 3.2, I appeal to the *IUE* spectra of 10 LMC globular clusters observed by Cassatella et al. (1987), in which the

---

[5] See Section 1.6 for the definition of apparent magnitude. The relation between the apparent (m) and absolute (M) magnitudes is given by the *distance modulus* μ: $\mu \equiv m - M = -2.5 \log d - 5$, where d is the distance to the object.

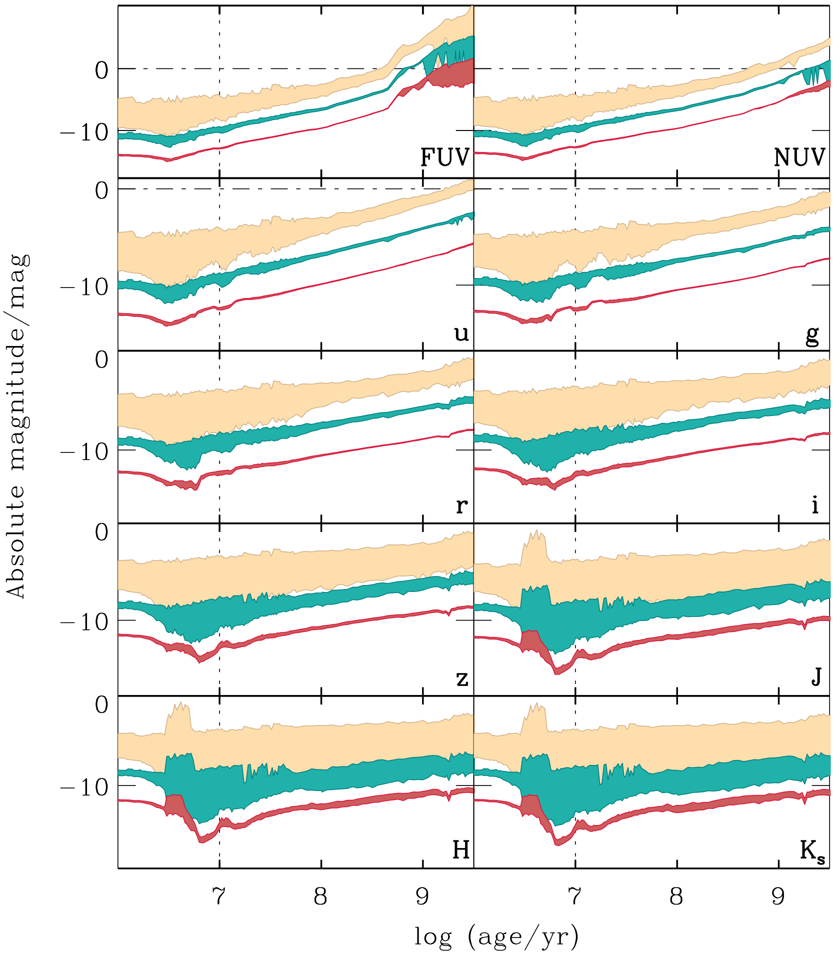

Figure 3.3 – Absolute magnitudes of the same models as in Fig. 3.2, computed through the *GALEX* FUV and NUV, SDSS *ugriz* and 2MASS JHK_s filters (*GALEX* and SDSS magnitudes are on the AB system, while 2MASS ones are on the Vega system).

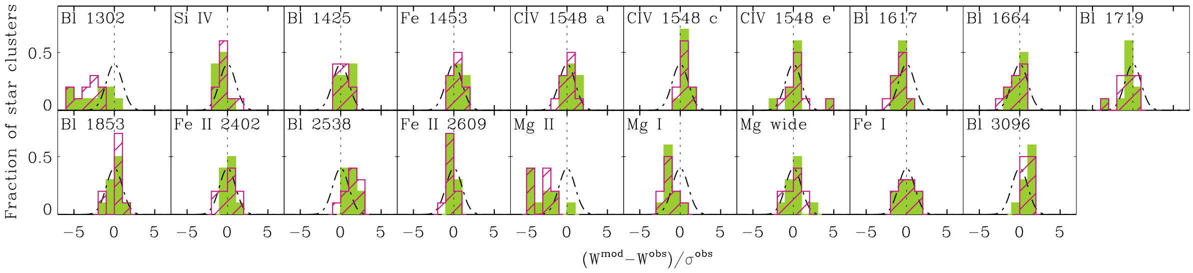

Figure 3.4 – Distribution of the difference in index strength between best-fitting model and observed spectra, in units of the observational error, for the 10 clusters in the Cassatella et al. (1987) sample and the 19 Fanelli et al. (1992) ultraviolet spectral indices defined in Table 3.1 (as indicated). For each index, the filled (green) and hatched (violet) histograms show the distributions obtained using models with stochastically sampled and smoothly sampled IMFs, respectively, while the black dot-dashed line shows a reference Gaussian distribution with unit standard deviation.

strengths of the 19 Fanelli et al. (1992) indices listed in Table 3.1 were measured by Maraston et al. (2009). Although Cassatella et al. (1987) originally corrected their spectra for reddening by dust in the Milky Way and the LMC (using the extinction laws of Savage & Mathis 1979 and Howarth 1983), these smooth corrections do not account for the potential contamination of the spectra by discrete ISM absorption lines arising from resonant ionic transitions (see, e.g., Savage & de Boer, 1979, 1981; Savage et al., 1997). I account for this effect by correcting the index measurements in tables B.1 and B.2 of Maraston et al. (2009), which these authors performed in the reddening-corrected *IUE* spectra of Cassatella et al. (1987), for the strongest interstellar absorption features, as described in Appendix B. In brief, since I do not know the column densities of different ionic species along the lines of sight to individual LMC clusters, I follow Leitherer et al. (2011, see their table 3) and adopt a mean correction based on the median equivalent widths of the 24 strongest Milky Way absorption lines measured in the wavelength range $1150 \lesssim \lambda \lesssim 3200$ Å along 83 lines of sight by Savage et al. (2000). Although this correction does not account for potential extra contamination by LMC absorption lines, I expect such a contribution to be moderate. This is because the Cassatella et al. (1987) clusters are old enough ($\gtrsim 10$ Myr; see Section 3.3.3) to have broken out of their parent molecular clouds (Murray et al., 2010; Murray, 2011), as also indicated by the absence of nebular emission lines in their spectra.

The resulting ISM correction term, Δ(EW/Å), is listed in Table 3.1 for each index (strong interstellar Mg II absorption makes the corrections to the Mg wide and Mg II 2800 indices particularly large). The final corrected index strengths and associated errors for all clusters are listed in Table B.1 of Appendix B (along with the adopted V-band magnitudes of the clusters). For reference, not including these corrections for interstellar line absorption would imply changes of typically 1 (5), 13 (25) and 10 (7) per cent, respectively, in the logarithmic estimates of age, metallicity and stellar-mass of the Cassatella et al. (1987) star clusters using the stochastic (smooth) models presented in Section 3.3.3 below.

3.3.2 Model library

To interpret the observed ultraviolet index strengths of the Cassatella et al. (1987) star clusters, I use the models presented in Section 3.2 to build large libraries of SSP spectra for both a smoothly sampled and a stochastically sampled Chabrier (2003) IMFs (I make the usual assumption that individual star clusters can be approximated as SSPs). Specifically, I compute models at 14 metallicities, $Z = 0.0001$, 0.0002, 0.0005, 0.001, 0.002, 0.004, 0.006, 0.008, 0.010, 0.014, 0.017, 0.020, 0.030 and 0.040, for 67 logarithmically spaced ages between 10 Myr and 1 Gyr. The spectra for a smoothly sampled IMF scale linearly with stellar mass (e.g., Bruzual & Charlot, 2003). For a stochastically sampled IMF, at each of the 67 stellar ages of the grid, I compute 220 realizations of SSP spectra for 33 logarithmically spaced stellar masses between 2×10^2 M$_\odot$ and 3×10^5 M$_\odot$ (as described in Section 3.2.3).

It is important to start by evaluating the extent to which I can expect these models to reproduce the observed ultraviolet index strengths of the Cassatella et al. (1987) star clusters. In particular, the models assume scaled-solar heavy-element abundance ratios at all metallicities, while the relative abundances of different elements (such as the abundance ratio of α elements to iron-peak elements, α/Fe) can vary from cluster to cluster in the LMC (e.g., Colucci et al., 2012, see also Section 1.5 for a physical explanation of this enhancement). A simple way to assess the goodness-of-fit by a model j of the observed index strengths in the ultraviolet spectrum of a given cluster is to compute the χ^2 statistics,

$$\chi_j^2 = \sum_i \left(\frac{W_i^j - W_i^{\mathrm{obs}}}{\sigma_i^{\mathrm{obs}}} \right)^2 , \tag{3.2}$$

where the summation index i runs over all spectral indices observed, W_i^j and W_i^{obs} are the equivalent widths of index i in the model and observed spectra, respectively, and σ_i^{obs} is the observational error.

Fig. 3.4 shows the distribution of the difference in index strength between best-fitting model (corresponding to the minimum χ_j^2 as computed using equation 3.2) and observed spectra, in units of the observational error, for the 10 clusters in the Cassatella et al. (1987) sample. Each panel corresponds to a different spectral index in Table 3.1. In each case, the filled and hatched histograms show the distributions obtained using models with stochastically sampled and smoothly sampled IMFs, respectively, while the dot-dashed line shows a reference Gaussian distribution with unit standard deviation. As expected from the similarity between models with a smoothly sampled and a stochastically sampled IMFs at ages between 10 Myr and 1 Gyr in Figs. 3.1 and 3.2, the filled and hatched histograms are quite similar in all panels in Fig. 3.4. The fact that most histograms in this figure fall within the reference Gaussian distribution further indicates that, globally, the models reproduce reasonably well the ultraviolet index strengths in the observed spectra. Two notable exceptions are the distributions for Bl 1302 and Mg II 2800, which display significant tails relative to a Gaussian distribution. For these features, the implied systematic larger absorption in the data relative to the models could arise from either an enhanced α/Fe ratio in the Cassatella et al. (1987) clusters, or an underestimate of interstellar absorption, or both. To proceed with a meaningful comparison of models with data in the next paragraphs, I exclude Bl 1302 and Mg II 2800 from this analysis.[6]

3.3.3 Age, metallicity and stellar-mass estimates

I use of the library of SSP models computed in the previous Section to estimate the ages, metallicities and stellar masses of the Cassatella et al. (1987) star clusters on the basis of the 17 Fanelli et al. (1992) ultraviolet indices that can be reasonably well reproduced by the models

---

[6] For Bl 1302 and Mg II 2800, the median of the difference $W^{\mathrm{mod}} - W^{\mathrm{obs}}$ in Fig. 3.4 exceeds $1.5\,\sigma^{\mathrm{obs}}$ for models with a stochastically sampled IMF. I use this threshold to define 'badly fitted indices' in Fig. 3.4 and keep the 17 other, better-fitted indices to pursue the analysis.

Table 3.2 – Median estimates of age, metallicity and stellar mass – and associated 68 per cent central credible intervals – for the 10 clusters in the Cassatella et al. (1987) sample, obtained as described in Section 3.3.3 using models with stochastically sampled and smoothly sampled IMFs (the quantity $\chi^{2,\mathrm{sto}}_{\mathrm{min}}/\chi^{2,\mathrm{smo}}_{\mathrm{min}}$ indicates the ratio of minimum χ^2_j's, as computed using equations 3.2 and 3.4, between the two types of models). Literature values, along with ultraviolet-based age and metallicity estimates from Maraston et al. (2009), are also reported for reference.

Cluster	This work: smoothly sampled IMF			This work: stochastically sampled IMF		
	log(age/yr)	$\log(Z/Z_\odot)$	$\log(M_{\mathrm{cl}}/\mathrm{M}_\odot)$	log(age/yr)	$\log(Z/Z_\odot)$	$\log(M_{\mathrm{cl}}/\mathrm{M}_\odot)$
NGC 1711	$7.51^{+0.44}_{-0.26}$	$-0.45^{+0.27}_{-0.73}$	$4.37^{+0.23}_{-0.07}$	$7.49^{+0.46}_{-0.34}$	$-0.57^{+0.39}_{-0.61}$	$4.19^{+0.31}_{-0.19}$
NGC 1805	$7.41^{+0.14}_{-0.06}$	$-0.27^{+0.31}_{-0.32}$	$3.99^{+0.11}_{-0.09}$	$7.43^{+0.12}_{-0.08}$	$-0.29^{+0.34}_{-0.29}$	$3.83^{+0.17}_{-0.13}$
NGC 1818	$7.47^{+0.48}_{-0.22}$	$-0.63^{+0.45}_{-0.85}$	$4.37^{+0.33}_{-0.07}$	$7.46^{+0.49}_{-0.21}$	$-0.73^{+0.55}_{-0.75}$	$4.23^{+0.37}_{-0.13}$
NGC 1847	$7.28^{+0.17}_{-0.03}$	$-0.26^{+0.30}_{-0.15}$	$3.83^{+0.17}_{-0.03}$	$7.28^{+0.17}_{-0.13}$	$-0.28^{+0.33}_{-0.13}$	$3.62^{+0.18}_{-0.22}$
NGC 1850	$7.76^{+0.19}_{-0.21}$	$-0.12^{+0.24}_{-0.16}$	$4.72^{+0.18}_{-0.12}$	$7.76^{+0.29}_{-0.21}$	$-0.18^{+0.29}_{-0.23}$	$4.63^{+0.17}_{-0.23}$
NGC 1866	$7.93^{+0.32}_{-0.28}$	$-0.26^{+0.31}_{-0.62}$	$4.55^{+0.25}_{-0.05}$	$7.97^{+0.28}_{-0.32}$	$-0.28^{+0.33}_{-0.60}$	$4.47^{+0.23}_{-0.17}$
NGC 1984	$7.27^{+0.18}_{-0.12}$	$+0.05^{+0.24}_{-0.23}$	$4.23^{+0.17}_{-0.03}$	$7.29^{+0.16}_{-0.14}$	$+0.01^{+0.28}_{-0.19}$	$4.07^{+0.13}_{-0.17}$
NGC 2004	$7.20^{+0.15}_{-0.05}$	$+0.03^{+0.09}_{-0.06}$	$4.35^{+0.15}_{-0.05}$	$7.18^{+0.17}_{-0.03}$	$+0.00^{+0.12}_{-0.04}$	$4.19^{+0.11}_{-0.09}$
NGC 2011	$7.03^{+0.11}_{-0.09}$	$+0.18^{+0.24}_{-0.14}$	$3.93^{+0.17}_{-0.13}$	$7.06^{+0.19}_{-0.01}$	$+0.06^{+0.23}_{-0.10}$	$3.46^{+0.34}_{-0.26}$
NGC 2100	$7.24^{+0.11}_{-0.09}$	$-0.23^{+0.19}_{-0.06}$	$4.53^{+0.17}_{-0.03}$	$7.24^{+0.11}_{-0.09}$	$-0.25^{+0.21}_{-0.03}$	$4.37^{+0.13}_{-0.07}$

Cluster	$\chi^{2,\mathrm{sto}}_{\mathrm{min}}/\chi^{2,\mathrm{smo}}_{\mathrm{min}}$	Literature			Maraston et al. (2009)	
		log(age/yr)	$\log(Z/Z_\odot)$	$\log(M_{\mathrm{cl}}/\mathrm{M}_\odot)$	log(age/yr)	$\log(Z/Z_\odot)$
NGC 1711	0.864	$7.70 \pm 0.05^{\mathrm{a}}$	$-0.57 \pm 0.17^{\mathrm{a}}$	$4.21^{+0.16}_{-0.16}$ $^{\mathrm{h}}$	7.50	−0.10
NGC 1805	0.909	$7.65 \pm 0.05^{\mathrm{i}}$	$-0.25 \pm 0.25^{\mathrm{b,e}}$	$3.52^{+0.13}_{-0.13}$ $^{\mathrm{h}}$	7.20	−0.33
NGC 1818	0.864	$7.40 \pm 0.30^{\mathrm{b}}$	$-0.25 \pm 0.25^{\mathrm{b,e,l}}$	$4.13^{+0.15}_{-0.14}$ $^{\mathrm{h}}$	7.50	−0.20
NGC 1847	0.918	$7.42 \pm 0.30^{\mathrm{d}}$	$-0.40^{\mathrm{h,j}}$	$3.86^{+0.09}_{-0.10}$ $^{\mathrm{h}}$	6.85	−0.40
NGC 1850	0.995	$7.97 \pm 0.10^{\mathrm{j}}$	$-0.12 \pm 0.20^{\mathrm{f}}$	$4.87^{+0.13}_{-0.14}$ $^{\mathrm{h,m}}$	8.00	−0.10
NGC 1866	0.970	$8.25 \pm 0.05^{\mathrm{k}}$	-0.28^{12}	$4.63^{+0.08}_{-0.08}$ $^{\mathrm{h}}$	8.00	−0.50
NGC 1984	0.882	$7.06 \pm 0.30^{\mathrm{d}}$	$-0.90 \pm 0.40^{\mathrm{g}}$	$3.38^{+0.35}_{-0.28}$ $^{\mathrm{h}}$	7.10	−0.10
NGC 2004	0.966	$7.30 \pm 0.20^{\mathrm{c,j}}$	$-0.56 \pm 0.20^{\mathrm{f,j}}$	$4.43^{+0.24}_{-0.23}$ $^{\mathrm{h}}$	7.20	+0.00
NGC 2011	0.682	$6.99 \pm 0.30^{\mathrm{d}}$	$-0.47 \pm 0.40^{\mathrm{g}}$	$3.47^{+0.38}_{-0.32}$ $^{\mathrm{h}}$	6.70	+0.00
NGC 2100	0.918	$7.31 \pm 0.04^{\mathrm{j}}$	$-0.32 \pm 0.20^{\mathrm{f,j}}$	$4.48^{+0.33}_{-0.30}$ $^{\mathrm{h}}$	7.35	+0.20

References: [a]Dirsch et al. (2000); [b]de Grijs et al. (2002); [c]Elson (1991);[d]Elson & Fall (1988); [e]Johnson et al. (2001); [f]Jasniewicz & Thevenin (1994); [g]Oliva & Origlia (1998); [h]Mackey & Gilmore (2003); [i]Liu et al. (2009); [j]Niederhofer et al. (2015) ; [k]Bastian & Silva-Villa (2013) ; [l]Korn et al. (2000); [m] McLaughlin & van der Marel (2005).

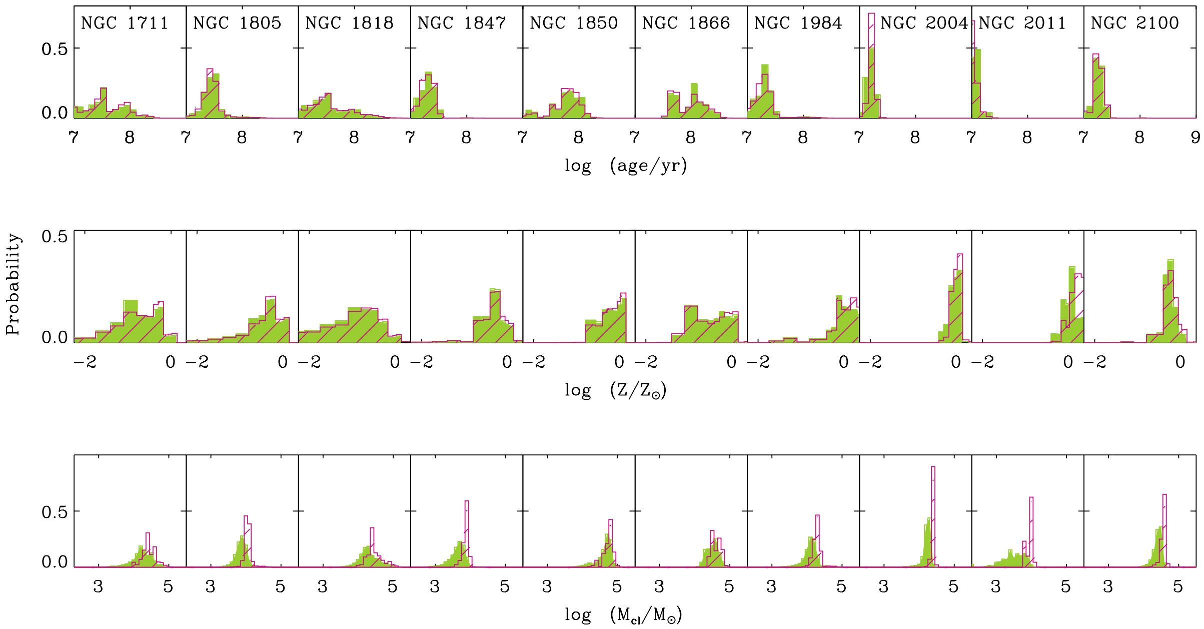

Figure 3.5 – Posterior probability distributions of age (top row), metallicity (middle row) and stellar mass (bottom row) for the 10 clusters in the Cassatella et al. (1987) sample, obtained as described in Section 3.3.3 using models with stochastically sampled (green filled histograms) and smoothly sampled (violet hatched histograms) IMFs.

(footnote 6). I adopt a standard Bayesian approach (see Section 5.1) and compute the likelihood of an observed set of spectral indices $W^{\rm obs}$ given a model j with parameters (age, metallicity and stellar mass) Θ^j as

$$P(W^{\rm obs} \mid \Theta^j) \propto \exp(-\chi_j^2/2)\,, \tag{3.3}$$

where I have assumed that the observed index strengths can be modelled as a multi-variate Gaussian random variable, with mean given by the index strengths of the model with parameters Θ^j and noise described by a diagonal covariance matrix (e.g., Chevallard & Charlot, 2016). For models with a smoothly sampled IMF, the value of χ_j^2 entering equation (3.3) is that given in equation (3.2). In this case, the posterior probability distribution of stellar mass for a given cluster can be derived from that of the mass-to-light ratio and the observed absolute V-band magnitude. For models with a stochastically sampled IMF, the luminosity does not scale linearly with stellar mass (Section 3.3.2), and the fit of the absolute V-band magnitude must be inserted in the definition of χ_j^2, i.e.,

$$\chi_j^2 = \left(\frac{V^j - V^{\rm obs}}{\sigma_V^{\rm obs}}\right)^2 + \sum_i \left(\frac{W_i^j - W_i^{\rm obs}}{\sigma_i^{\rm obs}}\right)^2\,. \tag{3.4}$$

Here V^j and $V^{\rm obs}$ are the model and observed absolute V-band magnitudes, respectively, $\sigma_V^{\rm obs}$ is the associated observational error and the other symbols have the same meaning as in equation (3.2). The combination of the likelihood function in equation (3.3) with the model

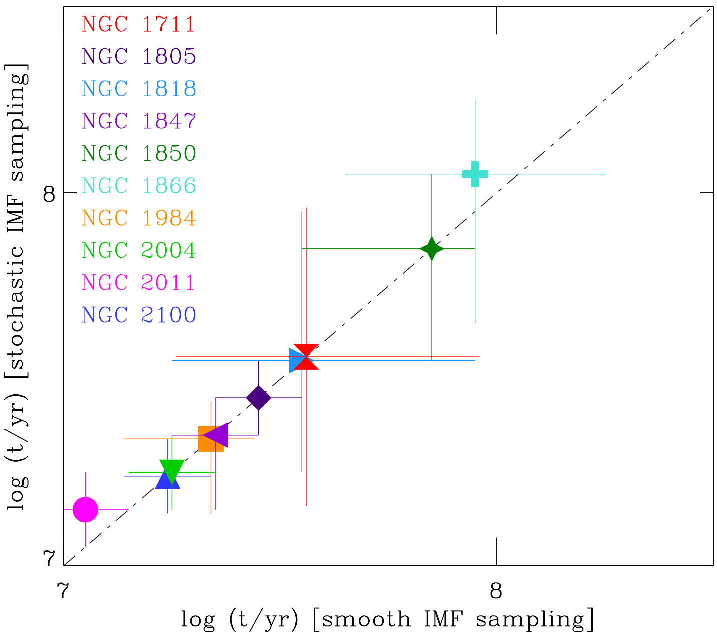

Figure 3.6 – Comparison of median estimates of age – and associated 68 per cent central credible intervals – obtained as described in Section 3.3.3 using models with stochastically sampled and smoothly sampled IMFs, for the 10 clusters in the Cassatella et al. (1987) sample (colour-coded as indicated).

library of Section 3.3.2, which assumes flat prior distributions of age, metallicity and stellar mass, allows us to compute the posterior probability distributions of these parameters for each cluster (see, e.g., equation 3.2 of Chevallard & Charlot, 2016).

Fig. 3.5 shows the posterior probability distributions of age (top row), metallicity (middle row) and stellar mass (bottom row) obtained in this way for the 10 clusters in the Cassatella et al. (1987) sample, using models with stochastically sampled (filled histograms) and smoothly sampled (hatched histograms) IMFs. Table 3.2 lists the corresponding median estimates of age, metallicity and stellar mass – and the associated 68 per cent central credible intervals – along with previous age and metallicity estimates from the literature. In general, I find that the probability distributions in Fig. 3.5 are narrower for clusters with index strengths measured with larger signal-to-noise ratio (Table B.1). The similarity of the constraints derived on age and metallicity using both types of IMF sampling is striking, although expected from Figs. 3.1, 3.2 and 3.4, given that all star clusters turn out to have ages in the range $10 \lesssim t \lesssim 100\,\mathrm{Myr}$ (and hence, in the favourable range between 10 Myr and 1 Gyr; see Section 3.3.2 and Table 3.2). Interestingly, models with a stochastically sampled IMF always fit the data better than those with a smoothly sampled IMF, as reflected by the minimum-χ^2 ratios reported in Table 3.2. This table also shows that the constraints derived here on cluster ages and metallicities (in the range $0.2 \lesssim Z/Z_\odot \lesssim 1.1$) generally agree, within the errors, with previous estimates based on different models and observables.

A notable result from Fig. 3.5 is the systematic lower stellar mass obtained when using models with a stochastically sampled IMF, as appropriate for star clusters with masses in the range $1 \times 10^3 \lesssim M_\mathrm{cl}/M_\odot \lesssim 4 \times 10^4$ (Section 3.2.3 and Table 3.2), relative to a smoothly sampled IMF. The difference reaches up to a factor of 3 in the case of the youngest cluster, NGC 2011. This result, which contrasts with those pertaining to age and metallicity estimates, is visualised otherwise in Figs. 3.6–3.8, in which I compare the median estimates of age, metallicity and stellar

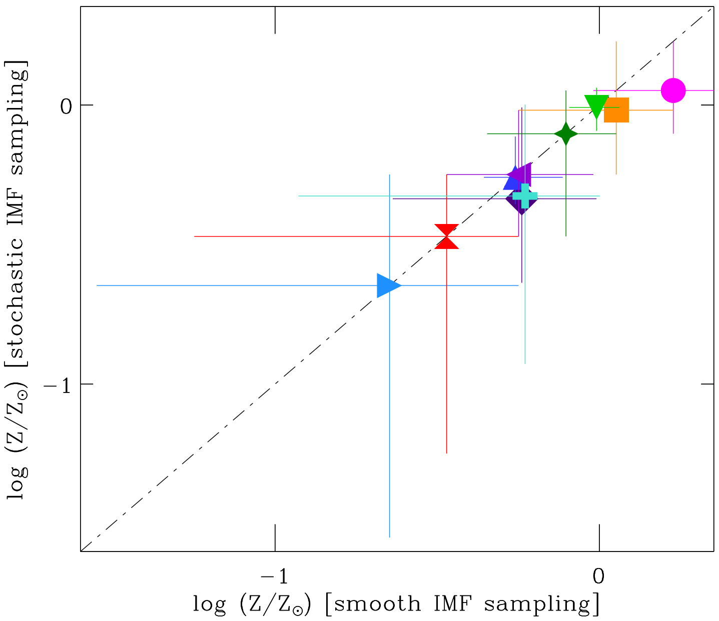

Figure 3.7 – Same as Fig. 3.6, but for metallicity estimates.

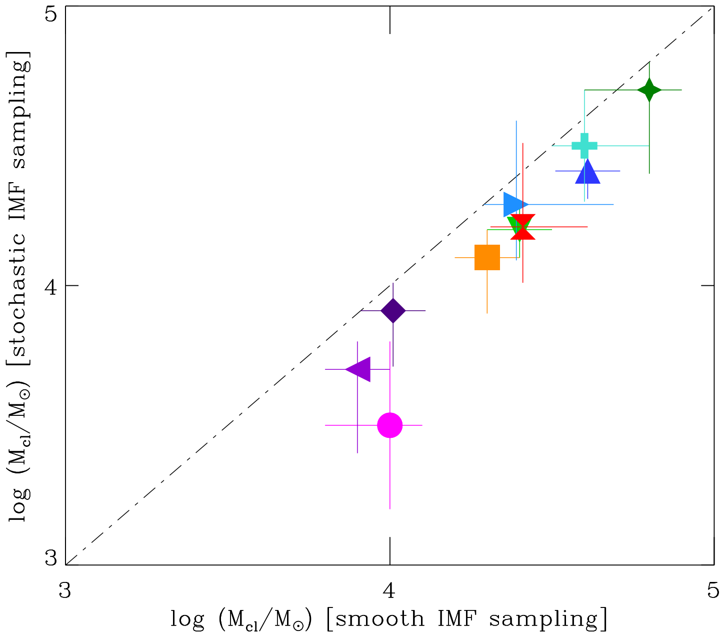

Figure 3.8 – Same as Fig. 3.6, but for stellar-mass estimates.

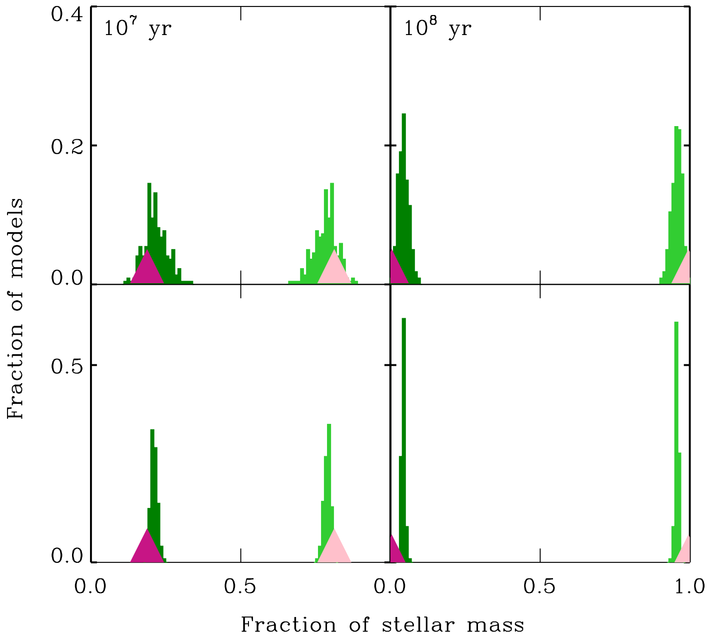

Figure 3.9 – Distribution of the fraction of integrated stellar mass contributed by stars more/less massive than 5 $M_\odot$ (dark/light green) for four sets of 220 realisations of SSPs with a stochastically sampled Chabrier (2003) IMF and target stellar masses 10^3 $M_\odot$ (top) and 10^4 $M_\odot$ (bottom) at the ages of 10 Myr (left) and 100 Myr (right), for the metallicity $Z = 0.008$. Dark/light pink triangles indicate the corresponding values for models with a smoothly sampled Chabrier (2003) IMF.

mass (and the associated 68 per cent central credible intervals) from models with stochastically sampled and smoothly sampled IMFs. While age and metallicity estimates from both types of models are in good general agreement (within the errors) in Figs 3.6 and 3.7, the systematic offset in stellar-mass estimates between stochastically and smoothly sampled IMFs appears clearly in Fig. 3.8. To investigate the origin of this effect, I plot in Fig. 3.9 the contributions by stars more/less massive than 5 $M_\odot$ (roughly the limit between massive and intermediate-mass stars; e.g. Bressan et al., 2012) to the integrated stellar mass of SSPs weighing 10^3 and 10^4 $M_\odot$, at the ages of 10 and 100 Myr, for models with stochastically and smoothly sampled IMFs (in the former case, I show the results of 220 cluster realisations for each combination of stellar mass and age; see the figure caption for details). I adopt the metallicity $Z = 0.008$, typical of the Cassatella et al. (1987) clusters in Table 3.2.

Fig. 3.9 shows that stars more massive than 5 $M_\odot$ account typically for a larger fraction of the total cluster mass when the IMF is stochastically sampled than when it is smoothly sampled, for SSP masses of both 10^3 and 10^4 $M_\odot$ and ages of both 10 and 100 Myr. This is because, when a massive star is drawn in a stochastic model, it can account for a substantial fraction of the cluster mass, while models with a smoothly sampled IMF can contain 'fractions' of massive stars in fixed proportion to the number of less massive stars.[7] This is also why models with smoothly sampled IMFs appear as single triangles in Fig. 3.9, while the histograms for models with stochastically sampled IMFs indicate that the mass fraction in stars more massive

---

[7] For example, a 10^3 $M_\odot$ cluster with a smoothly sampled Chabrier (2003) IMF truncated at 0.1 and 100 $M_\odot$ contains 0.07 stars with masses between 90 and 100 $M_\odot$ (and hence, a total of ~993 $M_\odot$ of lower-mass stars). In contrast, if a 100 Mo star is drawn when stochastically sampling the IMF, only 900 $M_\odot$ can be accounted by lower-mass stars.

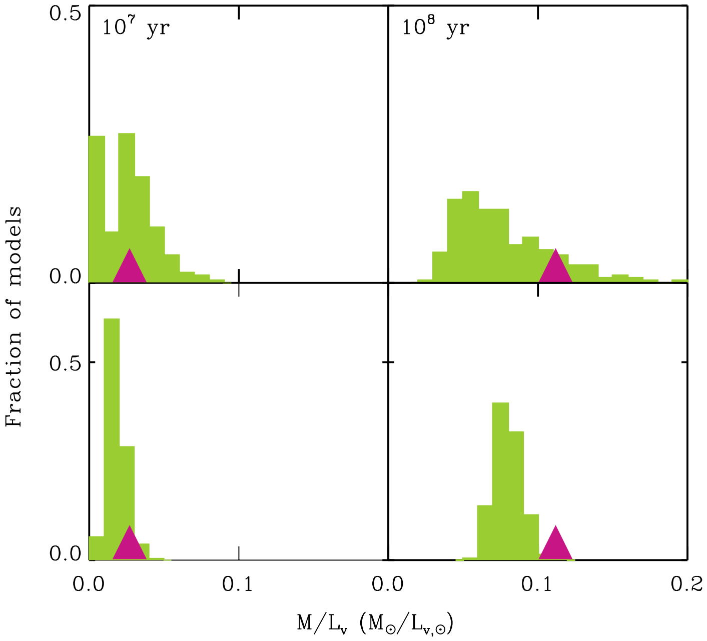

Figure 3.10 – Integrated mass-to-V-band luminosity ratio of the same model SSPs as in Fig. 3.9, with stochastically sampled (green) and smoothly sampled (pink) IMFs.

than 5 M$_\odot$ depends on the actual stellar masses drawn in each cluster realisation. Since the mass-to-light ratio of massive stars is much smaller than that of low- and intermediate-mass stars, the results of Fig. 3.9 have implications for the integrated mass-to-light ratio of young star clusters. This is shown in Fig. 3.10, where I plot the mass-to-V-band luminosity ratio of the same model star clusters as in Fig. 3.9. As anticipated, models with stochastically sampled IMFs have systematically lower mass-to-light ratio than those with smoothly sampled IMFs. This explains the difference in the masses of the Cassatella et al. (1987) star clusters retrieved using both types of models in Fig. 3.8 and Table 3.2. Note that changing the upper mass limit of the IMF by a factor of a few would have no influence on the results of Figs. 3.6–3.8, since the turnoff mass of the youngest cluster (NGC 2011) is already as low as 18 M$_\odot$.

It is also interesting to examine the difference in the absolute broadband magnitudes predicted at ultraviolet, optical and near-infrared wavelengths for the Cassatella et al. (1987) star clusters by the same models with stochastically and smoothly sampled IMFs as shown in Figs. 3.6–3.8. I present this in Fig. 3.11 for the magnitudes predicted in the *GALEX* FUV and NUV, SDSS *ugriz* and 2MASS JHK_S filters. Only for the youngest cluster, NGC 2011, is the difference substantial between the median magnitudes predicted using both types of IMF sampling, particularly in the reddest bands but with a large uncertainty.

I conclude from this Section that the stellar population models presented in Section 3.2 provide reasonable fits to the observed ultraviolet spectral signatures of young stellar populations at ages between 10 Myr and 100 Myr. At these ages, the neglect of stochastic variations in the number of massive stars hosted by individual star clusters does not have a strong influence on age and metallicity estimates. However, such a neglect can introduce a systematic bias in stellar-mass estimates. Given that the spectral evolution predicted at ages younger than 10 Myr by the models presented in Section 3.2 has already been shown to provide reasonable fits of the nebular emission from observed galaxies (e.g., Stark et al., 2014, 2015a; Feltre et al., 2016, see also Section 4.2.2 below), I feel confident that these models represent a valuable means of

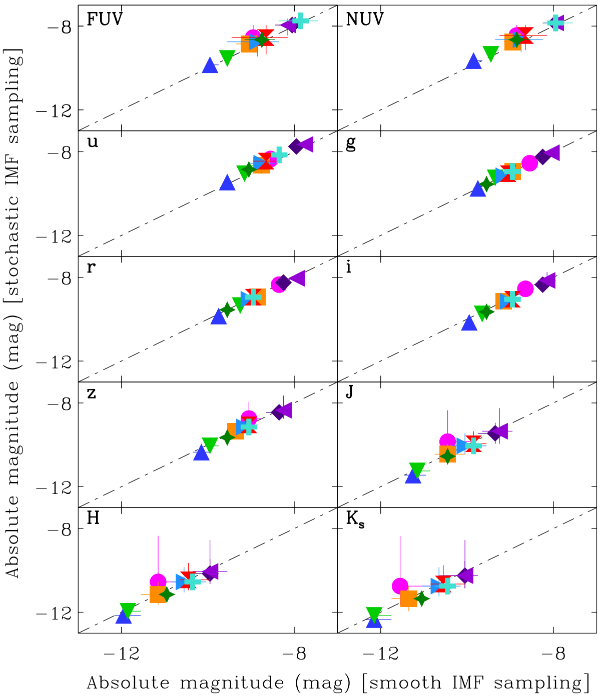

Figure 3.11 – Comparison of the median absolute magnitudes in the *GALEX* FUV and NUV, SDSS *ugriz* and 2MASS JHK_S filters – and associated 68 per cent central credible intervals – predicted by the same models with stochastically and smoothly sampled IMFs as in Figs. 3.6–3.8.

exploring the rest-frame ultraviolet emission from star-forming galaxies. This is my aim in the remainder of this work.

Chapter 4

Influence of the ISM on ultraviolet spectra of star-forming galaxies

In this chapter, I present the new approach I have developed to model the combined influence of nebular emission and interstellar absorption on the ultraviolet spectra of star-forming galaxies. This approach builds on an idealized description of the main features of the ISM. As a first application, I study in detail the model spectra of a young, metal-poor galaxy and a more mature, metal-rich galaxy to identify the cleanest ultraviolet tracers of young stars, nebular emission and interstellar absorption. This chapter is also extracted from the paper submitted to MNRAS entitled *Modelling ultraviolet-line diagnostics of stars, the ionized and the neutral interstellar medium in star-forming galaxies.*

Contents

4.1 ISM modelling 58
  4.1.1 Approach 58
  4.1.2 Examples of model spectra 64
4.2 Ultraviolet tracers of stars and the ISM 67
  4.2.1 Features tracing young stars 67
  4.2.2 Features tracing nebular emission 71
  4.2.3 Features tracing interstellar absorption 72
  4.2.4 Important composite features 72

4.1 ISM modelling

In this section I explore the impact of absorption and emission by the ISM on the ultraviolet spectra of star-forming galaxies. I consider three components: nebular emission from the photoionized ISM; absorption by highly ionized species in the photoionized ISM; and absorption by weakly ionized species in the neutral ISM. I refer to the last two components globally as 'interstellar absorption'. In Section 4.1 below, I start by presenting the approach to describe nebular emission and interstellar absorption in a star-forming galaxy. Then, in Section 4.2, I investigate the extent to which absorption and emission by the ISM can affect the strengths of the stellar absorption-line indices studied in Section 3.2. I identify those ultraviolet spectral features individually most promising tracers of the properties of stars (Section 4.2.1), nebular emission (Section 4.2.2) and interstellar absorption (Section 4.2.3) ISM. Some strong, widely studied ultraviolet features turn out to often be mixtures of stellar and interstellar components. I describe those in Section 4.2.4, where I explore their dependence on metallicity, star formation history and upper mass cutoff of the IMF.

4.1.1 Approach

The influence of the ISM on the luminosity produced by stars in a galaxy can be accounted for by expressing the luminosity per unit wavelength λ emerging at time t from that galaxy as (using the 'isochrone synthesis' technique of Charlot & Bruzual 1991)

$$L_\lambda(t) = \int_0^t dt'\, \psi(t-t')\, S_\lambda[t', Z(t-t')]\, T_\lambda(t,t'), \tag{4.1}$$

where $\psi(t-t')$ is the star-formation rate at time $t-t'$, $S_\lambda[t', Z(t-t')]$ the luminosity per unit wavelength per unit mass produced by a single stellar generation (SSP) of age t' and metallicity $Z(t-t')$ and $T_\lambda(t,t')$ is the transmission function of the ISM. I compute the spectral evolution $S_\lambda[t', Z(t-t')]$ using the stellar population synthesis model described in Section 3.2.1. At galactic stellar-mass scales, corresponding to stellar masses $M_{\rm gal} > 10^6\ {\rm M}_\odot$, fluctuations in integrated spectral properties arising from stochastic sampling of the stellar IMF are no longer an issue (Bruzual & Charlot, 2003, see also Section 3.2.3. in particular Figs. 3.2 and 3.3). Therefore, in all models in this section, I adopt a smoothly sampled Chabrier (2003) IMF. The transmission function $T_\lambda(t,t')$ in equation (4.1) is defined as the fraction of the radiation produced at wavelength λ at time t by a population of stars of age t' that is transferred through the ISM.

Following Charlot & Fall (2000), I express the transmission function of the ISM as the product of the transmission functions of stellar birth clouds (i.e. giant molecular clouds) and the intercloud medium (i.e. diffuse ambient ISM). I assume for simplicity that transmission through the birth clouds depends only on SSP age t', while transmission through the intercloud medium depends on the radiation field from the entire stellar population, of age t. I thus write[1]

$$T_\lambda(t,t') = T_\lambda^{\rm BC}(t')\, T_\lambda^{\rm ICM}(t). \tag{4.2}$$

Furthermore, as in Charlot & Fall (2000), I assume that the birth clouds are all identical and consist of an inner H II region ionized by young stars and bounded by an outer H I region. I thus rewrite the transmission function of the birth clouds as

---

[1] The function $T_\lambda^{\rm ICM}(t)$ in expression (4.2) replaces the function $T_\lambda^{\rm ISM}$ in the notation of Charlot & Fall (2000).

$$T_\lambda^{\rm BC}(t') = T_\lambda^{\rm HII}(t')\, T_\lambda^{\rm HI}(t'). \tag{4.3}$$

Note that, with the assumption that the ionized regions are bounded by neutral material, the function $T_\lambda^{\rm HII}$ will be close to zero at wavelengths blueward of the H-Lyman limit and greater than unity at wavelengths corresponding to emission lines. According to the stellar population synthesis model described in Section 3.2, less than 0.1 per cent of H-ionizing photons are produced at ages greater than 10 Myr by a single stellar generation. This is similar to the typical timescale for the dissipation of giant molecular clouds in star-forming galaxies (e.g., Murray et al., 2010; Murray, 2011). I therefore assume

$$T_\lambda^{\rm HII}(t') = T_\lambda^{\rm HI}(t') = T_\lambda^{\rm BC}(t') = 1\,, \quad \text{for} \quad t' > 10\,{\rm Myr}\,. \tag{4.4}$$

I now need prescriptions to compute the functions $T_\lambda^{\rm HII}(t')$ and $T_\lambda^{\rm HII}(t')$ at earlier ages, along with $T_\lambda^{\rm ICM}(t)$.

Recently, Gutkin et al. (2016) computed the transmission function of ionized gas in star-forming galaxies [$T_\lambda^{+}(t')$ in their notation], using the approach proposed by Charlot & Longhetti (2001, hereafter CL01). This consists in combining a stellar population synthesis model with a standard photoionization code to describe the galaxy-wide transfer of stellar radiation through ionized gas via a set of 'effective' parameters. Gutkin et al. (2016) combine in this way the stellar population synthesis model described in Section 3.2 with the latest version of the photoionization code CLOUDY (c13.03; described in Ferland et al. 2013a, see also Section 2.2.1). The link between the two codes is achieved through the time-dependent rate of ionizing photons produced by a typical star cluster ionizing an effective HII region,

$$Q(t') = \frac{M_*}{hc}\int_0^{\lambda_{\rm L}} d\lambda\, \lambda\, S_\lambda(t'), \tag{4.5}$$

where M_* is the mass of the ionizing star cluster, h and c are the Planck constant and the speed of light, $\lambda_{\rm L} = 912\,$Å the wavelength at the Lyman limit and, for clarity, the dependence of S_λ (and hence Q) on stellar metallicity Z has been dropped. The radius of the Strömgren sphere ionized by this star cluster in gas with effective density $n_{\rm H}$ (assumed independent of t') is given by

$$R_{\rm S}^3(t') = 3Q(t')/(4\pi {n_{\rm H}}^2 \epsilon \alpha_{\rm B})\,, \tag{4.6}$$

where ϵ is the volume-filling factor of the gas (i.e., the ratio of the volume-averaged hydrogen density to $n_{\rm H}$) and $\alpha_{\rm B}$ the case-B hydrogen recombination coefficient. The ionization parameter (i.e., the dimensionless ratio of the number density of H-ionizing photons to $n_{\rm H}$) at the Strömgren radius is then

$$U_{\rm S}(t') = Q(t')/(4\pi R_{\rm S}^2 n_{\rm H} c) = \frac{\alpha_{\rm B}^{2/3}}{3c}\left[\frac{3Q(t')\epsilon^2 n_{\rm H}}{4\pi}\right]^{1/3}. \tag{4.7}$$

In this approach, for a given input spectral evolution of single stellar generation, $S_\lambda(t')$, the galaxy-wide transmission function of the ionized gas can be computed by specifying the zero-age ionization parameter at the Strömgren radius,

$$U_{\rm S} \equiv U_{\rm S}(0), \tag{4.8}$$

along with $n_{\rm H}$ and the abundances of the different metals and their depletions onto dust grains (see below). The effective star-cluster mass M_* in equation (4.5) has no influence on the results other than that of imposing a maximum $U_{\rm S}$ at fixed $n_{\rm H}$ (corresponding to $\epsilon = 1$; CL01). Note that CLOUDY incorporates a full treatment of dust, including, in particular, absorption and scattering of photons, radiation pressure, photoelectric heating of the gas and collisional energy exchange between dust grains and the gas (Ferland et al., 2013a, see also van Hoof et al. 2004).

The computations by Gutkin et al. (2016) of the transmission function $T_\lambda^+(t')$ of ionized gas in star-forming galaxies cannot be used straightforwardly to represent the function $T_\lambda^{\rm HII}(t')$ entering equation (4.3). This is because the transmission function $T_\lambda^+(t')$ calculated by CLOUDY does not include *interstellar-line absorption* in the ionized gas (see Section 1.4.3), even though the code computes the full ionization structure of the nebula to produce the emission-line spectrum (of main interest to Gutkin et al. 2016). It is possible to account for interstellar-line absorption in the spectrum emerging from an HII region by appealing to another code to exploit the ionization structure solved by CLOUDY: the general spectrum synthesis program SYNSPEC (see e.g. Hubeny & Lanz, 2011, see also Section 2.2.2), which computes absorption signatures in the observed spectrum based on an exact radiative transfer solution for a specified structure of the medium (temperature, density, and possibly atomic energy level populations), and for a specified set of opacity sources (continua, atomic and molecular lines).[2] The combination of CLOUDY and SYNSPEC can be achieved via an interactive program called CLOUDSPEC (Hubeny et al., 2000, see also Heap et al. 2001), written in the Interactive Data Language (IDL). The CLOUDSPEC program calls SYNSPEC to solve the radiative transfer equation along the line of sight toward an ionizing source, based on the depth-dependent output of CLOUDY, to compute the strengths and profiles of interstellar absorption lines. This has been used successfully to interpret in detail the observed ultraviolet spectrum of, for example, the metal-poor nearby star-forming galaxy I Zw 18 (Lebouteiller et al., 2013). Note that, while Gutkin et al. (2016) stop their photoionization calculations at the edge of the Strömgren sphere, when the electron density falls below 1 per cent of $n_{\rm H}$ or if the temperature falls below 100 K, the CLOUDY calculations can be carried out further into the outer HI envelopes of the clouds. This has little interest for the computation of emission-line luminosities, since attenuation by dust eventually associated with HI can be included a posteriori (see, e.g., section 2.6 of Chevallard & Charlot 2016), but more interest for that of interstellar absorption lines.

In this work, I use the CLOUDSPEC wrapper of CLOUDY and SYNSPEC to compute in one go the transmission function of an effective (i.e. typical) birth cloud, $T_\lambda^{\rm BC}(t')$, through both the inner HII and outer HI regions [i.e., I do not compute separately $T_\lambda^{\rm HII}(t')$ and $T_\lambda^{\rm HI}(t')$ in equation 4.4]. I achieve this by adopting equations (4.5)–(4.8) above to describe the gas photoionized by stars younger than 10 Myr in terms of the effective zero-age ionization parameter at the Strömgren radius, $U_{\rm S}$, gas density, $n_{\rm H}$, and metal abundances and depletion factors. For the latter, I adopt the self-consistent, versatile prescription of Gutkin et al. (2016) to model in detail the influence of 'gas-phase' and 'interstellar' (i.e., total gas+dust phase) abundances on nebular emission. This prescription is based on the solar chemical abundances compiled by Bressan et al. (2012) from the work of Grevesse & Sauval (1998), with updates from Caffau et al. (2011, see table 1 of Bressan et al. 2012), and small adjustments for the solar nitrogen (−0.15 dex) and oxygen (+0.10 dex) abundances relative to the mean values quoted in table 5 of Caffau et al. (2011, see Gutkin et al. 2016 for details). The corresponding present-day solar (photospheric) metallicity is $Z_\odot = 0.01524$, and the protosolar metallicity (i.e. before the effects of diffusion) $Z^0_\odot = 0.01774$. Both N and C are assumed to have primary and secondary nucleosynthetic components. The abundance of combined primary+secondary nitrogen is related to that of oxygen via equation (11) of Gutkin et al. (2016), while secondary carbon production is kept flexible via an adjustable C/O ratio. For reference, the solar N/O and C/O ratios in this prescription are $({\rm N/O})_\odot = 0.07$ and $({\rm C/O})_\odot = 0.44$.[3] The depletion of heavy elements onto dust grains is computed using the default depletion factors of CLOUDY, with updates from Groves et al. (2004, see their table 2) for C, Na, Al, Si, Cl, Ca and Ni and and from Gutkin et al. (2016, see their table 1) for O. The resulting dust-to-metal mass ratio for solar interstellar metallicity, $Z_{\rm ISM} = Z_\odot$, is $\xi_{\rm d\odot} = 0.36$, with corresponding gas-phase abundances $12 + \log({\rm O/H})_{\odot,{\rm gas}} = 8.68$, $({\rm N/O})_{\odot,{\rm gas}} = 0.10$ and $({\rm C/O})_{\odot,{\rm gas}} = 0.31$. The dust-to-metal mass ratio, $\xi_{\rm d}$, can be treated as an ajustable parameter, along with the interstellar metallicity, $Z_{\rm ISM}$.

---

[2] See `http://nova.astro.umd.edu/Synspec49/synspec.html`

I use the above approach to compute the transmission function $T^{\rm BC}_\lambda(t')$ for given $S_\lambda(t')$, $n_{\rm H}$, $U_{\rm S}$, $Z_{\rm ISM}$, C/O and $\xi_{\rm d}$, tuning the CLOUDY 'stopping criterion' to allow calculations to expand beyond the HII region, into the outer HI envelope of a birth cloud. In the Milky Way, cold atomic gas organized in dense clouds, sheets and filaments has typical temperatures in the range 50–100 K and densities in the range $1 \lesssim n_{\rm H} \lesssim 10^3\,{\rm cm^{-3}}$ (e.g., Ferrière 2001, see also Section 1.4.3; this density range is similar to that of $1 \le n_{\rm H} \le 10^4\,{\rm cm^{-3}}$ considered by Gutkin et al. 2016 for their calculations of effective HII regions). I therefore stop the CLOUDY calculations when the kinetic temperature of the gas falls below 50 K and take this to define the HI envelope of a typical birth cloud. The corresponding HI column density and dust attenuation optical depth depend on the other adjustable parameters of the model, i.e., $S_\lambda(t')$, $n_{\rm H}$, $U_{\rm S}$, $Z_{\rm ISM}$, C/O and $\xi_{\rm d}$. Following Gutkin et al. (2016), I adopt the same metallicity for the ISM as for the ionizing stars, i.e., I set $Z_{\rm ISM} = Z$, and adopt spherical geometry for all models. Note that CLOUDSPEC also allows adjustments of the velocity dispersion of the gas, σ_v, and the macroscopic velocity field as a function of radius, $v(r)$.

Photons emerging from stellar birth clouds, and photons emitted by stars older than the typical dissipation time of a birth cloud (i.e. ∼10 Myr; equation 4.4), must propagate through the diffuse intercloud component of the ISM before they escape from the galaxy. This is accounted for by the transmission function $T^{\rm ICM}_\lambda(t)$ in equation (4.2). Little ionizing radiation is striking this medium since, in the model, the birth clouds are ionization bounded, while less than 0.1 per cent of H-ionizing photons are produced at ages greater than 10 Myr by an SSP. Before proceeding further, it is important to stress that the galaxy-wide intercloud medium considered here should not be mistaken for the 'diffuse ionized gas' observed to contribute about 20–50 per cent of the total H-Balmer-line emission in nearby spiral and irregular galaxies, which appears to be spatially correlated with HII regions and ionized, like these, by massive stars (e.g., Haffner et al., 2009, and references therein; see also Gutkin et al. 2016 and references therein). In this model, this diffuse ionized gas is subsumed in the HII-region component described by the effective, galaxy-wide parameters entering equations (4.5)–(4.8) (see also CL01). Instead, the intercloud medium refers to the warm, largely neutral gas filling much of the volume near the midplane of disc galaxies like the Milky Way (e.g., Ferrière, 2001, see also Section 1.4.3).

---

[3] This implies that, at solar metallicity, C, N and O represent respectively about 24, 4 and 54 per cent of all heavy elements by number (these values differ from those in footnote 3 of Gutkin et al. 2016, computed without accounting for the fine tuning of N and O abundances).

I appeal once more to CLOUDSPEC to compute the transmission function $T_\lambda^{\rm ICM}(t)$ of this component. Since the aim here is to illustrate the signatures of diffuse interstellar absorption in ultraviolet galaxy spectra rather than compute an exhaustive grid of models encompassing wide ranges of parameters, I fix the hydrogen density of the intercloud medium at $n_{\rm H}^{\rm ICM} = 0.3\,{\rm cm}^{-3}$, roughly the mean density of the warm Milky-Way ISM (e.g., Ferrière, 2001, see also Section 1.4.3). Furthermore, for simplicity, I adopt the same interstellar metallicity, dust-to-metal mass ratio and C/O ratio for this component as for the birth clouds ($Z_{\rm ISM}$, $\xi_{\rm d}$ and C/O). The weakness of the ionizing radiation in the intercloud medium argues against a parametrization of the transmission function in terms of the zero-age ionization parameter via a flexible volume-filling factor, as was appropriate for the birth clouds (equations 4.7–4.8). Instead, I fix the volume-filling factor of the intercloud medium at $\epsilon = 1$ and choose as main adjustable parameter the typical HI column density seen by photons in the intercloud medium, $N_{\rm HI}^{\rm ICM}$, which I use as stopping criterion for CLOUDY. The radiation striking this medium is the sum of that emerging from the birth clouds and that produced by stars older than 10 Myr. A subtlety arises from the fact that these sources are distributed throughout the galaxy, hence the radiation striking the intercloud medium in any location is more dilute than if all the sources were concentrated in a single point near that location. I wish to account for this effect in a simple way, without having to introduce geometric dilution parameters. I achieve this by taking the energy density of the interstellar radiation field of the Milky Way at $\lambda_{1500} = 1500\,$Å as reference and assuming that this quantity scales linearly with star formation rate. Specifically, I require that the energy density $u_{1500}(t)$ at time t at λ_{1500} of a galaxy with current star formation rate $\psi(t) = 1\ {\rm M_\odot\,yr^{-1}}$, roughly equal to that of the Milky Way (e.g., Robitaille & Whitney, 2010), be that of the local interstellar radiation field, $u_{1500}^{\rm MW} \approx 3\times10^{-16}\,{\rm erg\,cm^{-3}\,Å^{-1}}$ (e.g., Porter & Strong, 2005; Maciel, 2013), and write

$$u_{1500}(t) = 3\times10^{-16}\,[\psi(t)/1\ {\rm M_\odot\,yr^{-1}}]\,{\rm erg\,cm^{-3}\,Å^{-1}}\,. \tag{4.9}$$

In practice, I meet the above condition by adjusting the inner radius of the ionized nebula in CLOUDY, $r_{\rm in}$, such that

$$\frac{L_{1500}^{\rm BC} + L_{1500,*}^{\rm ICM}(t)}{4\pi r_{\rm in}^2 c} = u_{1500}(t), \tag{4.10}$$

where $L_{1500}^{\rm BC} + L_{1500,*}^{\rm ICM}(t)$ is the 1500-Å luminosity emitted by the birth clouds and stars older than 10 Myr at time t (equations 4.12 and 4.13 below). The gas velocity dispersion and macroscopic velocity field in the intercloud medium, $\sigma_v^{\rm ICM}$ and $v^{\rm ICM}(r)$, can be defined independently of those in the birth clouds.

Table 4.1 summarizes the main adjustable parameters of the stars and ISM in the model. While idealized, this parametrization provides a means of exploring in a physically consistent way those features of the ISM that are expected to have the strongest influence on the ultraviolet spectra of star-forming galaxies. In practice, I compute the luminosity per unit wavelength

Table 4.1 – Main adjustable parameters of stars and the ISM in the model of star-forming galaxies presented in Section 4. For the ISM, the parameters are 'effective' ones describing galaxy-wide properties of gas and dust (see text for details).

Parameter	Physical meaning
	Stars
$\psi(t)$	Star formation rate as a function of time
$Z(t)$	Stellar metallicity as a function of time
m_{up}	Upper mass cutoff of the IMF[a]
	Stellar birth clouds
n_{H}	Hydrogen number density
U_{S}	Zero-age ionization parameter[b]
Z_{ISM}	Interstellar metallicity [$Z_{\mathrm{ISM}} = Z(t)$ by default][c]
ξ_d	Dust-to-metal mass ratio
C/O	Carbon-to-oxygen abundance ratio
σ_v	Velocity dispersion of the gas
$v(r)$	Macroscopic velocity field of the gas
	Diffuse intercloud medium[d]
$n_{\mathrm{H}}^{\mathrm{ICM}}$	Hydrogen number density
$N_{\mathrm{HI}}^{\mathrm{ICM}}$	H I column density
σ_v^{ICM}	Velocity dispersion of the gas
$v^{\mathrm{ICM}}(r)$	Macroscopic velocity field of the gas

[a] The default IMF is that of Chabrier (2003).

[b] At the Strömgren radius, as defined by equations (4.7)–(4.8).

[c] By default, the interstellar metallicity in the birth clouds is taken to be the same as that of the youngest ionizing stars.

[d] By default, Z_{ISM}, ξ_{d} and C/O in the intercloud medium are taken to be the same as those in the birth clouds.

emerging at time t from a star-forming galaxy (equation 4.1) as

$$L_\lambda(t) = T_\lambda^{\mathrm{ICM}}(t)\left[L_\lambda^{\mathrm{BC}} + L_{\lambda,*}^{\mathrm{ICM}}(t)\right], \tag{4.11}$$

where

$$L_\lambda^{\mathrm{BC}} = \int_0^{10\,\mathrm{Myr}} dt'\,\psi(t-t')\,S_\lambda[t', Z(t-t')]\,T_\lambda^{\mathrm{BC}}(t') \tag{4.12}$$

is the luminosity emerging from the birth clouds and

$$L_{\lambda,*}^{\mathrm{ICM}}(t) = \int_{10\,\mathrm{Myr}}^{t} dt'\,\psi(t-t')\,S_\lambda[t', Z(t-t')] \tag{4.13}$$

is the emission from stars older than 10 Myr.

4.1.2 Examples of model spectra

Fig. 4.1 shows two examples of ultraviolet spectra of star-forming galaxies computed using the model described in Section 4.1.1 above, corresponding to a young ($t = 10\,\mathrm{Myr}$), low-metallicity ($Z = 0.002$) galaxy (Fig. 4.1a) and a mature ($t = 5\,\mathrm{Gyr}$), more metal-rich ($Z = 0.017$) galaxy (Fig. 4.1b). Since all the stars in the young-galaxy model are still embedded in their birth clouds, I do not include any intercloud medium in this case. For simplicity, in both models, I adopt constant star formation rate, an IMF upper mass cutoff $m_{\mathrm{up}} = 100\ \mathrm{M}_\odot$, and I assume that all stars in the galaxy have the same metallicity Z. In this approach, the absolute star formation rate must be specified only to determine the rate of ionizing photons striking the intercloud medium in the mature-galaxy model, where I take $\psi(t) = 1\ \mathrm{M}_\odot \mathrm{yr}^{-1}$. For the ISM, I adopt in both models $\xi_{\mathrm{d}} = 0.3$, C/O = $(\mathrm{C/O})_\odot$, $\sigma_v = 50\,\mathrm{km\,s^{-1}}$ and static birth clouds ($v = 0$) with $n_{\mathrm{H}} = 100\,\mathrm{cm^{-3}}$. This value of σ_v is intermediate between the typical velocity dispersion of ionized gas in nearby dwarf galaxies (∼20–30 $\mathrm{km\,s^{-1}}$; Moiseev et al., 2015) and in the Milky-Way ISM (∼50–110 $\mathrm{km\,s^{-1}}$; Savage et al., 2000, see also Leitherer et al. 2011). For reference, the spectral resolution of the stellar population synthesis model of Section 3.2 ranges roughly from 150 $\mathrm{km\,s^{-1}}$ at $\lambda = 1000$ Å (resolving power $R \approx 400$) to 50 $\mathrm{km\,s^{-1}}$ at $\lambda = 3000$ Å ($R \approx 1200$). I also need to specify the zero-age ionization parameter of the birth clouds. I adopt $\log U_{\mathrm{S}} = -2.0$ for the young-galaxy model, i.e. the typical value observed by Stark et al. (2014) in four low-metallicity dwarf star-forming galaxies at redshift $z \sim 2$, and $\log U_{\mathrm{S}} = -3.5$ for the mature-galaxy model. This is consistent with the dependence of U_{S} on Z_{ISM} identified by Carton et al. (in preparation; see equation 25 of Chevallard & Charlot 2016) in a large sample of SDSS galaxy spectra.

To isolate the effect of each model component on the predicted spectrum of the young-galaxy model in Fig. 4.1a, I show four spectra: the spectrum produced by stars (solid grey swath); the spectrum output by CLOUDY when used in a standard way to compute the transmission function of ionized gas [gold curve; this corresponds to, for example, the transmission function $T_\lambda^{+}(t')$ computed by Gutkin et al. 2016]; the same spectrum after accounting with CLOUDSPEC for interstellar-line absorption in the ionized gas [thick light-blue curve; this corresponds to the

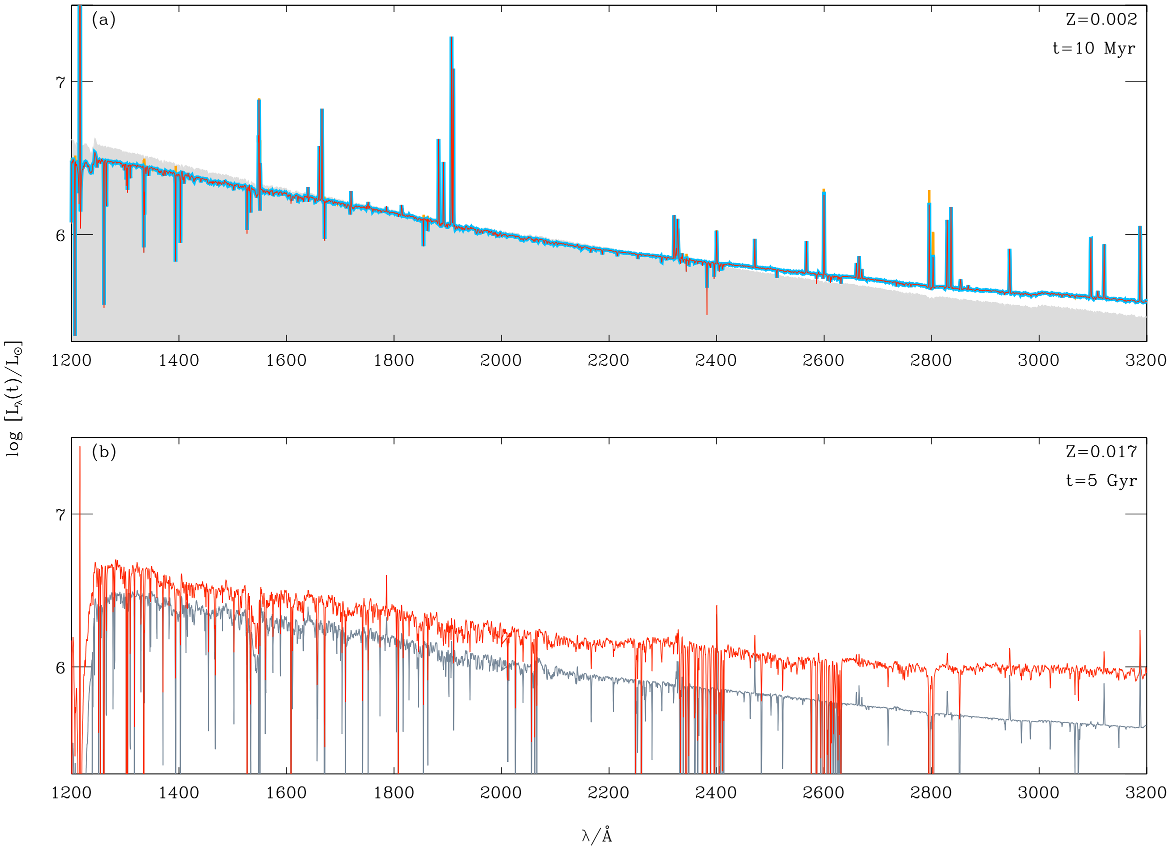

Figure 4.1 – Examples of ultraviolet spectra of star-forming galaxies computed using the model described in Section 4.1.1: (a) low-metallicity ($Z = 0.002$), young galaxy model with constant star formation $\psi(t) = 1\ \mathrm{M_{\odot}yr^{-1}}$ for $t = 10\,\mathrm{Myr}$. The different spectra shown are that produced by stars (solid grey swath), the spectrum output by CLOUDY when used in a standard way to compute the transmission function of ionized gas (gold curve), the same spectrum after accounting with CLOUDSPEC for interstellar-line absorption in the ionized gas (thick light-blue curve) and the spectrum emerging from the outer HI boundaries of birth clouds (red curve); (b) metal-rich ($Z = 0.017$), mature galaxy model with constant star formation $\psi(t) = 1\ \mathrm{M_{\odot}yr^{-1}}$ for $t = 5\,\mathrm{Gyr}$ and an intercloud medium. The two spectra shown are the contribution by stellar birth clouds to the emergent luminosity (grey curve) and the total luminosity emerging from the galaxy (in red). See text Section 4.1.2 for more details about the ISM parameters of these models.

transmission function $T_\lambda^{\rm HII}(t')$ in equation 4.3]; and the spectrum emerging from the outer H I boundaries of birth clouds [red curve; corresponding to the full transmission function $T_\lambda^{\rm BC}(t')$ in equation 4.3 and computed using equation 4.12]. The three spectra transferred through the ionized gas lie above the input stellar population spectrum at wavelengths $\lambda \gtrsim 2500\,\text{Å}$ in Fig. 4.1a. This is because of the contribution by Balmer-recombination continuum photons produced in the nebula (see Section 1.4.3). At shorter wavelengths, the transferred radiation is fainter than that of the input stellar population because of absorption by dust, whose optical depth increases blueward, from $\tau_\lambda \approx 0.2$ at $\lambda = 3200\,\text{Å}$ to $\tau_\lambda \approx 0.4$ at $\lambda = 1200\,\text{Å}$. Note that, for the adopted high $\log U_{\rm S} = -2.0$, the bulk of this absorption occurs in the ionized interiors of birth clouds. This is because the hydrogen column density of the ionized region scales roughly as $\epsilon n_{\rm H} R_{\rm S} \propto U_{\rm S}$; hence the dust optical depth scales also as $U_{\rm S}$ at fixed dust-to-gas ratio $\xi_{\rm d} Z_{\rm ISM}$ (see also Mathis 1986; CL01). For reference, in this low-metallicity, young-galaxy model, the H II and H I column densities of a new birth cloud (i.e. corresponding to an SSP age $t' = 0$ in equation 4.3) are $\sim 3 \times 10^{21} \rm cm^{-2}$ and $\sim 5 \times 10^{19} \rm cm^{-2}$, respectively, implying a much thinner H I envelope (out to a kinetic gas temperature of 50 K) than the interior H II region.

A most remarkable feature of Fig. 4.1a is the prominence of interstellar absorption lines arising from the ionized region, as revealed by the post-processing with SYNSPEC of CLOUDY output using the CLOUDSPEC tool (thick light-blue curve). Among the deepest absorption lines are those corresponding to the Si II $\lambda1260$, O I $\lambda1302$, Si II $\lambda1304$, C II $\lambda1335$, Si IV $\lambda\lambda1394, 1403$, Si II $\lambda1526$, Si II* $\lambda1533$, C IV $\lambda\lambda1548, 1551$ and Al II $\lambda1671$ transitions. Accounting for this absorption is important, as it can influence the net emission luminosity of lines emerging from the ionized gas, as shown by the difference between the gold and light-blue spectra at the wavelengths of, for example, the C II $\lambda1335$, Si IV $\lambda\lambda1394, 1403$ and Mg II $\lambda\lambda2796, 2804$ lines in Fig. 4.1a. The difference between the light-blue and red spectra further shows that, in this example, only a modest contribution to interstellar absorption arises from the thin neutral envelopes of birth clouds. Aside from H-Lyα, the strongest emission lines in the emergent spectrum are C IV $\lambda\lambda1548, 1551$, O III]$\lambda\lambda1661, 1666$, [Si III]$\lambda1883$+Si III]$\lambda1892$ and mainly [C III]$\lambda1907$+C III]$\lambda1909$, with equivalent widths of 2.5, 2.8, 2.0 and 21.3 Å, respectively.

In the case of the mature-galaxy model, I must also specify the typical H I column density seen by photons in the intercloud medium. I adopt $N_{\rm HI}^{\rm ICM} = 5 \times 10^{20} \rm cm^{-2}$, typical of the H I column densities observed through the discs of nearby spiral galaxies (e.g., Warmels, 1988). Furthermore, for simplicity, I assume that gas in the intercloud medium is static ($v^{\rm ICM} = 0$), with a velocity dispersion $\sigma_v^{\rm ICM} = \sigma_v = 50\,\rm km\,s^{-1}$. In Fig. 4.1b, I show two spectra for this model: the contribution by stellar birth clouds to the emergent luminosity [grey curve; this corresponds to the term $T_\lambda^{\rm ICM}(t)\, L_\lambda^{\rm BC}$ in equation (4.11)]; and the total luminosity emerging from the galaxy [in red; corresponding to the quantity $L_\lambda(t)$ in equation (4.11)]. The birth clouds in this high-metallicity, low-ionization ($\log U_{\rm S} = -3.5$) model have zero-age H II and H I column densities of $\sim 1 \times 10^{20} \rm cm^{-2}$ and $\sim 2 \times 10^{20} \rm cm^{-2}$, respectively. This combination yields a dust absorption optical depth similar to that found for the young-galaxy model above (with $\tau_\lambda \approx 0.3$ at λ_{1500}), but with most of the absorption now occurring in the thick neutral envelopes of the clouds. From Fig. 4.1b, I find that the birth clouds contribute from nearly 80 per cent of the total ultraviolet emission of the galaxy at 1500 Å, to less than 50 per cent at 3200 Å. The emission lines in the emergent spectrum are much weaker than in the young-galaxy model of Fig. 4.1a. This is partly because of the higher $Z_{\rm ISM}$ and lower $U_{\rm S}$ (e.g., Gutkin et al., 2016), but also because of strong interstellar absorption.

The total emergent spectrum of the mature-galaxy model in Fig. 4.1b exhibits much stronger absorption features than that of the young-galaxy model in Fig. 4.1a. This is the case for all the interstellar lines mentioned previously, but also additional ones, such as for example

Fe II λ1608, Si II λ1808 and several clusters of metallic lines (involving Co II, Cr II, Fe II, Mg I, Mn II, Zn II and other species) around 2050, 2400 and 2600 Å. While most of the absorption in high-ionization lines, such as N V $\lambda\lambda$1238, 1242 and C IV $\lambda\lambda$1548, 1551, occurs in the hot interiors of the birth clouds, the intercloud medium dominates absorption in low-ionization lines, such as O I λ1302, Si II λ1304, C II λ1335, Fe II λ1608, Al II λ1671, Si II λ1808, a blend of Zn II, Cr II, Co II and Mg I lines at $\lambda = 2026$ Å, Fe II λ2383, Fe II λ2587, Fe II λ2600 and Mg II $\lambda\lambda$2796, 2804. For other lines, such as Si II λ1260 and Mg I λ2852, the neutral envelopes of the birth clouds can contribute up to 30 per cent of the total absorption. Note that interstellar absorption suppresses entirely emission in the Fe II λ2600 and Mg II $\lambda\lambda$2796, 2804 lines in the emergent spectrum of this model. The few emission lines standing out of the continuum in Fig. 4.1b are Fe II λ1786 ('UV 191' multiplet, with an equivalent width of only 0.44 Å), Fe II λ2400, [O II] λ2471, He I λ2829, He I λ2945, He I λ3121 and He I λ3188. Note also the deep H-Lyα absorption feature at 1216 Å, which arises from the resonant scattering of line photons through neutral hydrogen both in the birth-cloud envelopes and in the intercloud medium. For reference, the dust absorption optical depth in the intercloud medium is similar to that in the birth clouds (with $\tau_\lambda \approx 0.4$ at λ_{1500}). The warm, largely neutral intercloud medium produces only 1.2 per cent of the total Hα emission from the galaxy (the total emergent Hα equivalent width being of the order of 130 Å).

Hence, the simple approach outlined in Section 4.1.1 to model the influence of the ISM on starlight, while idealized, provides a unique means of exploring in a quantitative and physically consistent way the competing effects of stellar absorption, nebular emission and interstellar absorption in star-forming galaxy spectra. The prominent emission- and absorption-line features identified in the example ultraviolet spectra of a young, low-metallicity galaxy and a mature, more metal-rich galaxy in Fig. 4.1 are commonly observed in high-quality spectra of star-forming galaxies at various redshifts (e.g., Pettini et al., 2000; Shapley et al., 2003; Lebouteiller et al., 2013; Le Fèvre et al., 2013; James et al., 2014; Stark et al., 2014; Patrício et al., 2016). In the following subsections, I use this simple yet physically consistent model to identify those ultraviolet spectral features individually most sensitive to the properties of stars, the ionized and the neutral ISM in star-forming galaxies.

4.2 Ultraviolet tracers of stars and the ISM

The modeling approach presented in Section 4.1 above offers a valuable means of identifying the features most sensitive to stars, the ionized and the neutral ISM in the spectra of star-forming galaxies. In Section 4.2.1 below, I start by exploring the influence of the ISM on ultraviolet spectral indices commonly used to constrain the ages and metallicities of stellar populations. Then, I use the model to identify potentially good independent tracers of nebular emission (Section 4.2.2) and interstellar absorption (Section 4.2.3). I also investigate the complex dependence of Ill-studied lines, such as O V λ1371, Si IV $\lambda\lambda$1394, 1403 (hereafter simply Si IV λ1400), C IV $\lambda\lambda$1548, 1551 (hereafter simply C IV λ1550), He II λ1640, and N IV λ1719, on stellar absorption, nebular emission and interstellar absorption.

4.2.1 Features tracing young stars

Fig. 4.2 shows the strengths of the 19 Fanelli et al. (1992) indices studied in Sections 3.2 and 3.3 (Fig. 3.1) measured in the emergent spectrum of the mature-galaxy model of Section 4.1.2 at ages between 1×10^7 and 3×10^9 yr (brown dashed curve in each panel). Also shown for comparison in each panel is the index strength measured in the pure stellar population spectrum, i.e., before including the effects of nebular emission and interstellar absorption (salmon curve). For most in-

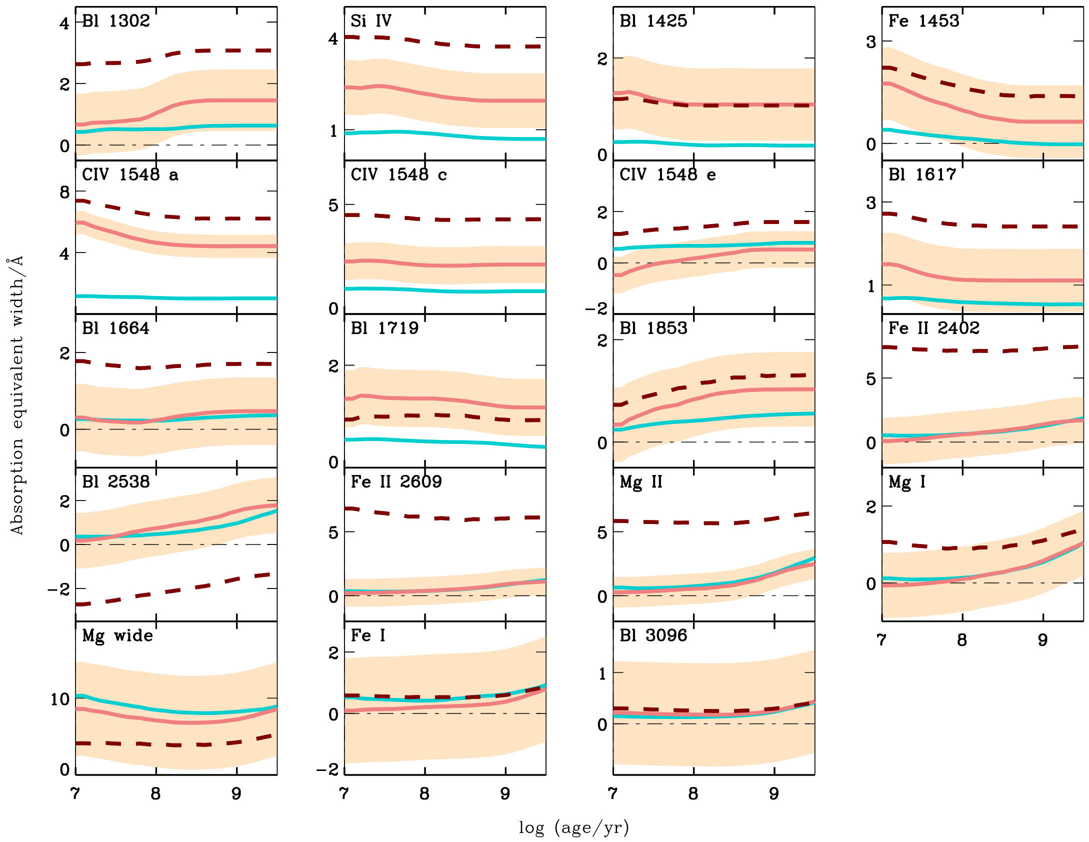

Figure 4.2 – Strengths of the 19 Fanelli et al. (1992) ultraviolet spectral indices defined in Table 3.1 plotted against age, for stellar populations with constant star formation rate and metallicities $Z = 0.002$ (teal blue curve) and 0.017 (salmon curve). The filled cream area around the $Z = 0.017$ model indicates the typical index measurement errors in the *IUE* spectra of the LMC clusters observed by Cassatella et al. (1987). The brown dashed curve shows the effect of accounting for nebular emission and interstellar absorption in the $Z = 0.017$ model (see text Section 4.2 for details).

dices, the brown curve lies above the salmon one in Fig. 4.2, indicating that interstellar absorption in the central index bandpass deepens the stellar absorption feature. For others, such as Bl 1719, Bl 2538, Mg I 2852 and Mg wide, the behaviour is opposite and caused in general, in this example, by contamination of a pseudo-continuum bandpass by interstellar absorption rather than of the central bandpass by nebular emission. A way to gauge the impact of ISM contamination on the interpretation of ultraviolet stellar absorption features is to compare the offsets between the brown and salmon curves in Fig. 4.2 to typical uncertainties in index-strength measurements. In each panel, the filled cream area around the solid salmon curve shows the median measurement uncertainty from Table B.1 for the 10 LMC star clusters observed by Cassatella et al. (1987). Indices for which the salmon curve lies within the cream area may therefore be considered a priori as those whose interpretation will be least affected by ISM contamination. In this example, these include Bl 1425, Fe 1453, Bl 1719, Bl 1853, Mg wide, Fe I 3000 and Bl 3096. In contrast, C IV-based indices (C IV$^{\mathrm{a}}$, C IV$^{\mathrm{c}}$, C IV$^{\mathrm{e}}$), Fe II 2402, Bl 2538, Fe II 2609 and Mg II 2800 appear to be most highly affected by ISM contamination.

It is also of interest to compare the impact of ISM contamination and that of stellar metallicity on the index strengths in Fig. 4.2. This is illustrated by the teal-blue curve, which shows in each panel the index strength measured in the pure stellar population spectrum of a model with constant star formation rate and metallicity $Z = 0.002$. For most indices, the difference between the teal-blue and salmon curves is smaller than that between the salmon and brown curves, indicating that ISM contamination can affect the index strength more than a change by a factor of 8.5 in metallicity. When this is not the case, the change in index strength induced by such a change in metallicity is generally smaller than the typical observational error (cream area in Fig. 4.2; as in the case of Fe 1453 and Bl 1617). Only for Bl 1425, C IV$^{\mathrm{a}}$ and Bl 1719 does the effect of metallicity seem measurable and stronger than that of ISM contamination. Among those, Bl 1425 and Bl 1719 appear to be the least sensitive to ISM contamination, and hence, the most useful to trace stellar population properties.

An alternative to the Fanelli et al. (1992) set of indices was proposed by Leitherer et al. (2001, see also Rix et al. 2004; Sommariva et al. 2012 and Section 1.6), who explored metallicity indicators in the ultraviolet spectra of stellar population synthesis models computed using the Starburst99 code (Leitherer et al., 1999). Unlike Fanelli et al. (1992), who define indices by measuring the fluxes in a central bandpass and two pseudo-continuum bandpasses in a spectrum, Leitherer et al. (2001) firstly normalize the spectrum to unit continuum through the division by a spline curve fitted to sections identified as free of stellar absorption lines in the model spectra. Then, they define line indices as the equivalent widths integrated in specific spectral windows of the normalized spectrum. Metallicity-sensitive indices defined in this way include the '1370' (1360–1380 Å) and '1425' (1415–1435 Å) indices of Leitherer et al. (2001), the '1978' (1935–2020 Å) index of Rix et al. (2004) and the '1460' (1450–1470 Å) and '1501' (1496–1506 Å) indices of Sommariva et al. (2012). Fig. 4.3 shows the emergent spectra of the young- and mature-galaxy models of Section 4.1.2 (dark-blue and brown curves, respectively), along with the input stellar population spectra of these models (light-blue and salmon curves), in the five spectral windows defining these metallicity-sensitive indices. The low-metallicity, young galaxy model shows no strong nebular-emission nor interstellar-absorption line in any of the windows. However, interstellar absorption can contaminate the indices at high metallicity, most notably Ni II λ1370 for 1370, Ni II λ1416, Co II λ1425 and S I λ1425 for 1425, Ni II λ1455, Co II λ1466 and Ni II $\lambda\lambda$1467, 1468 for 1460, Ni II λ1502 for 1501 and Co II λ1941, Si I λ1978 and Co II λ2012 for 1978. In the example of Fig. 4.3, contamination appears to be least severe for 1425, confirming the previous finding with regard to the Bl 1425 index of Fanelli et al. (1992). For the other indices, the potential influence of the ISM should be kept in mind when interpreting index strengths measured in observed galaxy spectra, especially at high metallicity.

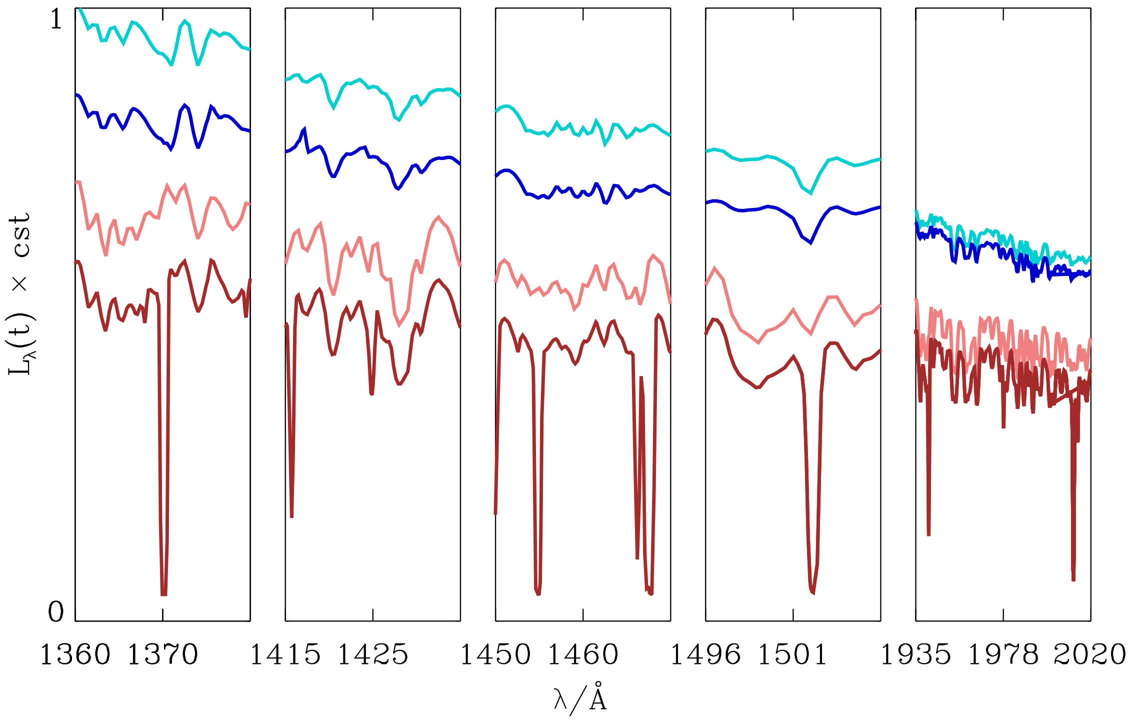

Figure 4.3 – Emergent spectra of the young- and mature-galaxy models of Fig. 4.1 (dark-blue and brown curves, respectively), along with the input stellar population spectra of these models (light-blue and salmon curves), in the five spectral windows defining the metallicity-sensitive indices '1370', '1425', '1460', '1501' and '1978' (Leitherer et al., 2001; Rix et al., 2004; Sommariva et al., 2012).

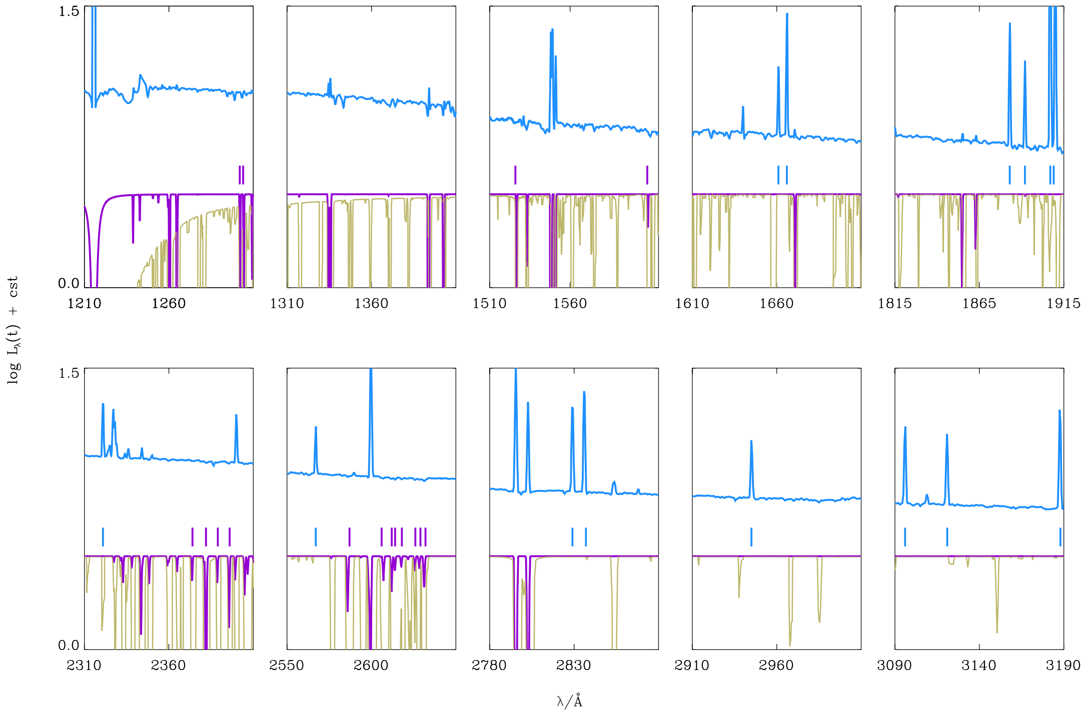

Figure 4.4 – Focus on spectral sections exhibiting the strongest features (marked by vertical bars) in the emission component (blue curve; corresponding to the gold curve in Fig. 4.1a) and the transmission function of the ISM (purple curve) in the 10 Myr-old, $Z = 0.002$ young-galaxy model of Fig. 4.1a. Also shown for reference is the transmission function of the ISM in the mature-galaxy model of Fig. 4.1b (olive-green curve).

4.2.2 Features tracing nebular emission

I now wish to identify those nebular emission lines least contaminated by stellar and interstellar absorption in the ultraviolet spectrum of a star-forming galaxy. To this end, I plot in Fig. 4.4 the emission component of the 10 Myr-old galaxy spectrum of Fig. 4.1a (blue curve; corresponding to the gold curve in Fig. 4.1a), along with the transmission function of the ISM in this low-metallicity model (purple curve). Also shown for reference in Fig. 4.4 is the transmission function of the ISM in the mature-galaxy model of Fig. 4.1b (olive-green curve), which unveils the locations of many more absorption features appearing at high metallicity. I choose to focus on the strongest emission and absorption features and do not show in Fig. 4.4 the wavelength intervals 1410–1510, 1915–2310, 1710–1815, 2410-2510 and 2660–2760 Å, where only a few weak lines appear in the young-galaxy spectrum of Fig. 4.1a.

A simple comparison of the blue and purple spectra in Fig. 4.4 reveals the strongest emission lines expected to be least sensitive to interstellar absorption. These are marked by blue vertical bars and reported in Table 4.2. These features include emission lines routinely observed in the ultraviolet spectra of high-redshift star-forming galaxies, such as O III]$\lambda\lambda$1661, 1666, [Si III]λ1883+Si III]λ1892 and [C III]λ1907+C III]λ1909 (Shapley et al., 2003; Erb et al., 2010; Christensen et al., 2012; Stark et al., 2014, 2015a). Note the appearance at high metallicity of an absorption feature (dominated by C I) just blueward of O III] λ1661, one (dominated by Ti II) underneath C III] λ1907 and another (dominated by Ni I) underneath [O III]λ2321, but these ultraviolet emission lines are anyway expected to be intrinsically much weaker, and hence difficult

Table 4.2 – Uncontaminated tracers of nebular emission and interstellar absorption in the ultraviolet spectra of star-forming galaxies.

Nebular emission lines
O iii]$\lambda\lambda1661, 1666$; [Si iii]$\lambda1883$+Si iii]$\lambda1892$; [C iii]$\lambda1907$+C iii]$\lambda1909$; [O iii]$\lambda2321$; Fe iv $\lambda2567$; Fe iv $\lambda2829$+He i $\lambda2829$; C ii $\lambda2838$; He i $\lambda2945$; Fe iv $\lambda3096$; He i $\lambda3121$; He i $\lambda3188$
Interstellar absorption lines
O i $\lambda1302$; Si ii $\lambda1304$; Si ii $\lambda1526$; Fe ii $\lambda1608$; Fe ii $\lambda2374$; Fe ii $\lambda2383$; Fe ii $\lambda\lambda2389, 2396$; Fe ii $\lambda2587$; Mn ii $\lambda2606$; Fe ii $\lambda2612$–$\lambda2632$ blend

to detect, at high metallicity (Gutkin et al., 2016). I refer the reader to Gutkin et al. (2016) for a comprehensive study on the dependence of the luminosities of the emission lines in Table 4.2 on the parameters of stars and stellar birth clouds in Table 4.1. These and other ultraviolet emission lines can also help discriminate between star formation and nuclear activity in galaxies (Feltre et al., 2016). Note that none of the emission lines listed in Table 4.2 is strongly affected by absorption originating in stellar winds and photospheres (e.g., Leitherer et al., 2011).

4.2.3 Features tracing interstellar absorption

Fig. 4.4 is also useful to identify the strongest interstellar absorption lines expected to be least sensitive to contamination by nebular emission and stellar absorption in the ultraviolet spectrum of a star-forming galaxy. These are marked by purple vertical bars and also reported in Table 4.2. Among these, O i $\lambda1302$, Si ii $\lambda1304$, Si ii $\lambda1526$, Fe ii $\lambda1608$, Fe ii $\lambda2374$ and Fe ii $\lambda2383$ have all been observed in the spectra of high-redshift star-forming galaxies (Pettini et al., 2002; Shapley et al., 2003; Erb et al., 2010; Christensen et al., 2012; Stark et al., 2014, 2015a). I do not include in this list Si ii $\lambda1260$, Si ii* $\lambda1265$, C ii $\lambda1335$, Si ii* $\lambda1533$, Al ii $\lambda1671$, Al iii $\lambda\lambda1855, 1863$, Fe ii $\lambda2600$, Mg ii $\lambda\lambda2796, 2804$ and Mg i $\lambda2852$, which are also observed at high redshift but can be contaminated by nebular emission. Moreover, the strong Si iv $\lambda1400$ and C iv $\lambda1550$ lines, which would be valuable tracers of the ionized ISM, are contaminated by stellar-wind features (these lines are discussed further in the next subsection). Note that Leitherer et al. (2011, their table 7) propose useful definitions of the ultraviolet spectral indices centred on O i $\lambda1302$+Si ii $\lambda1304$, Si ii $\lambda1526$, Fe ii $\lambda1608$ and Fe ii $\lambda2374$ in Table 4.2, based on a study of stellar and ISM features in the spectra of 28 local starburst and star-forming galaxies.

4.2.4 Important composite features

Some of the most prominent, widely studied features in the ultraviolet spectra of star-forming galaxy are blends of stellar (wind or photospheric) absorption, nebular emission and interstellar absorption. This model may also be used to illustrate the dependence of these features on star formation and ISM parameters. In Fig. 4.5, I show zooms around O v $\lambda1371$, Si iv $\lambda1400$, C iv $\lambda1550$, He ii $\lambda1640$ and N iv $\lambda1719$ in the spectrum emerging from a stellar birth cloud of metallicity $Z = Z_{\rm ISM} = 0.017$ (chosen high enough to exhibit prominent metallic lines), at ages between 1 and 10 Myr (the birth-cloud parameters are the same as in the mature-galaxy model of Section 4.1.2). This corresponds to the spectral energy distribution $S_\lambda(t')\,T_\lambda^{\rm BC}(t')$ in the notation of Section 4.1.1, for $1 \leq t' \leq 10$ Myr. In each panel, I show for each age the input stellar population spectrum, $S_\lambda(t')$ (in light blue), together with the emergent spectrum (in black, with the features of interest highlighted in pink). The continuum level in one spectrum relative to

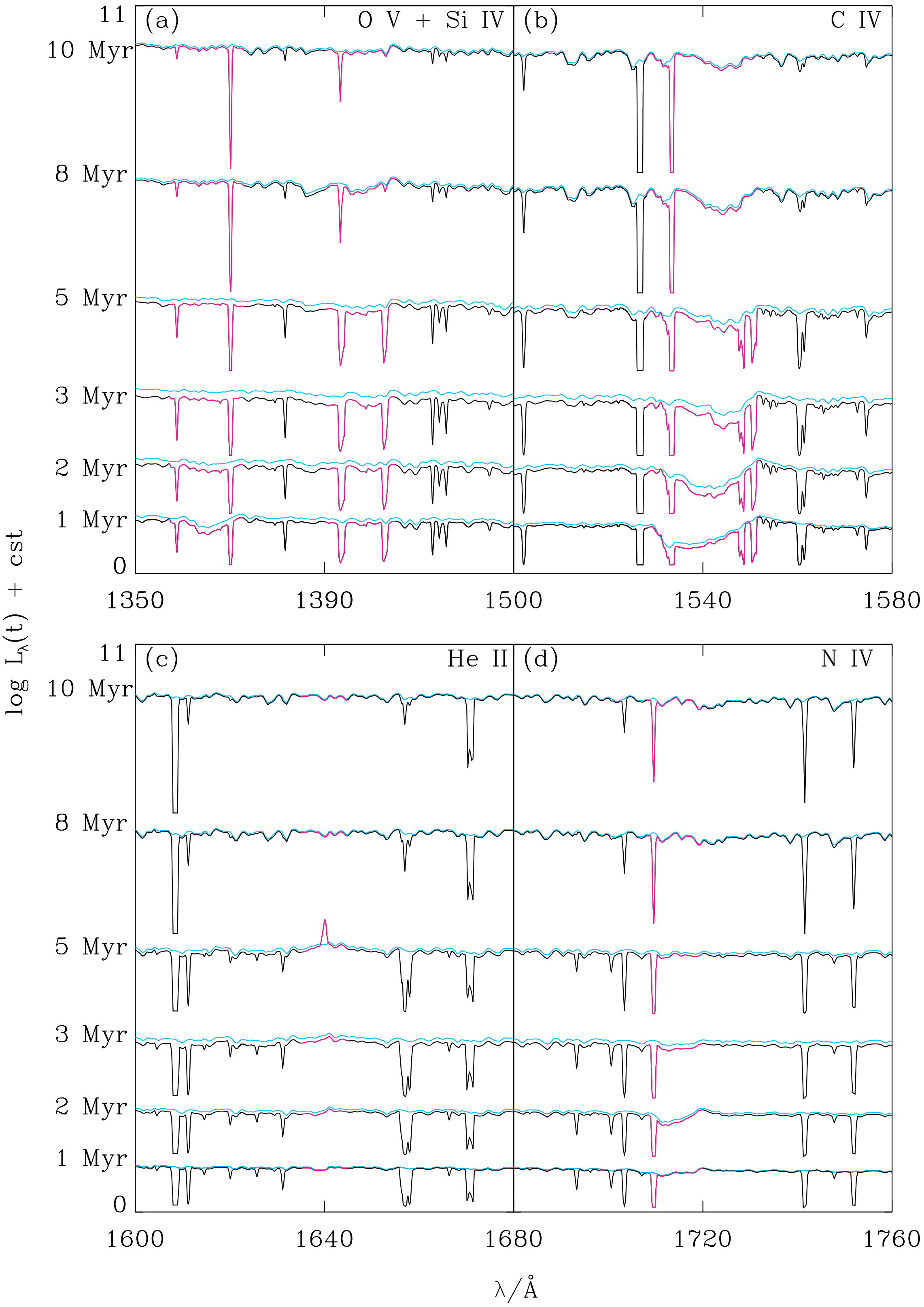

Figure 4.5 – Dependence of selected features on SSP age t' in the spectrum emerging from a stellar birth cloud with metallicity $Z = Z_{\rm ISM} = 0.017$, for $t' = 1, 2, 3, 5, 8$ and 10 Myr (as indicated). The birth-cloud parameters are the same as in the mature-galaxy model of Fig. 4.1b. In each panel and for each t', the light-blue curve shows the input SSP spectrum and the black one the emergent spectrum, with the features of interest highlighted in pink: (a) O V $\lambda1371$+Si IV $\lambda1400$; (b) C IV $\lambda1550$; (c) He II $\lambda1640$; and (d) N IV $\lambda1719$.

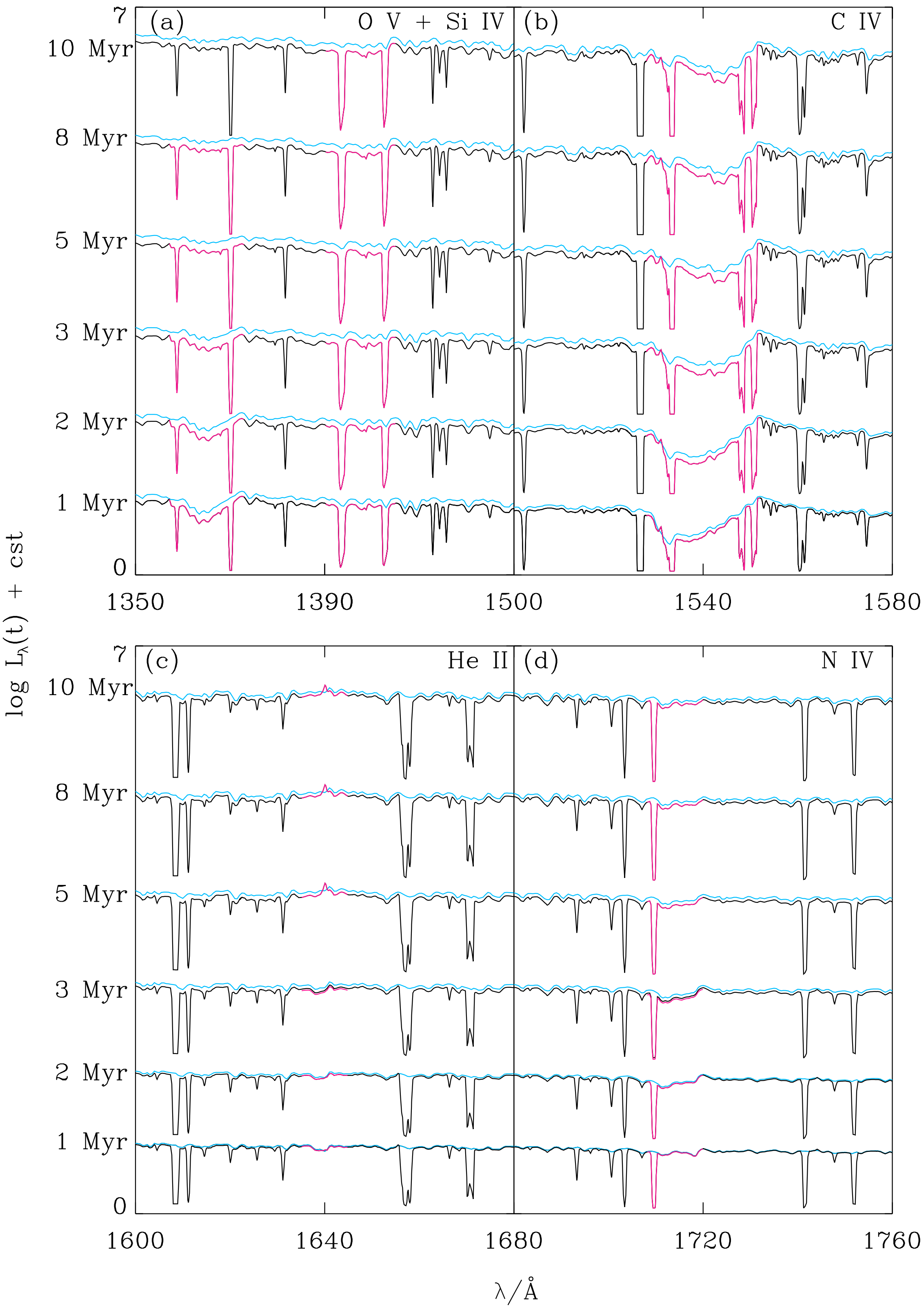

Figure 4.6 – Same as Fig. 4.5, but for a young-galaxy model with constant star formation rate and $Z = 0.017$.

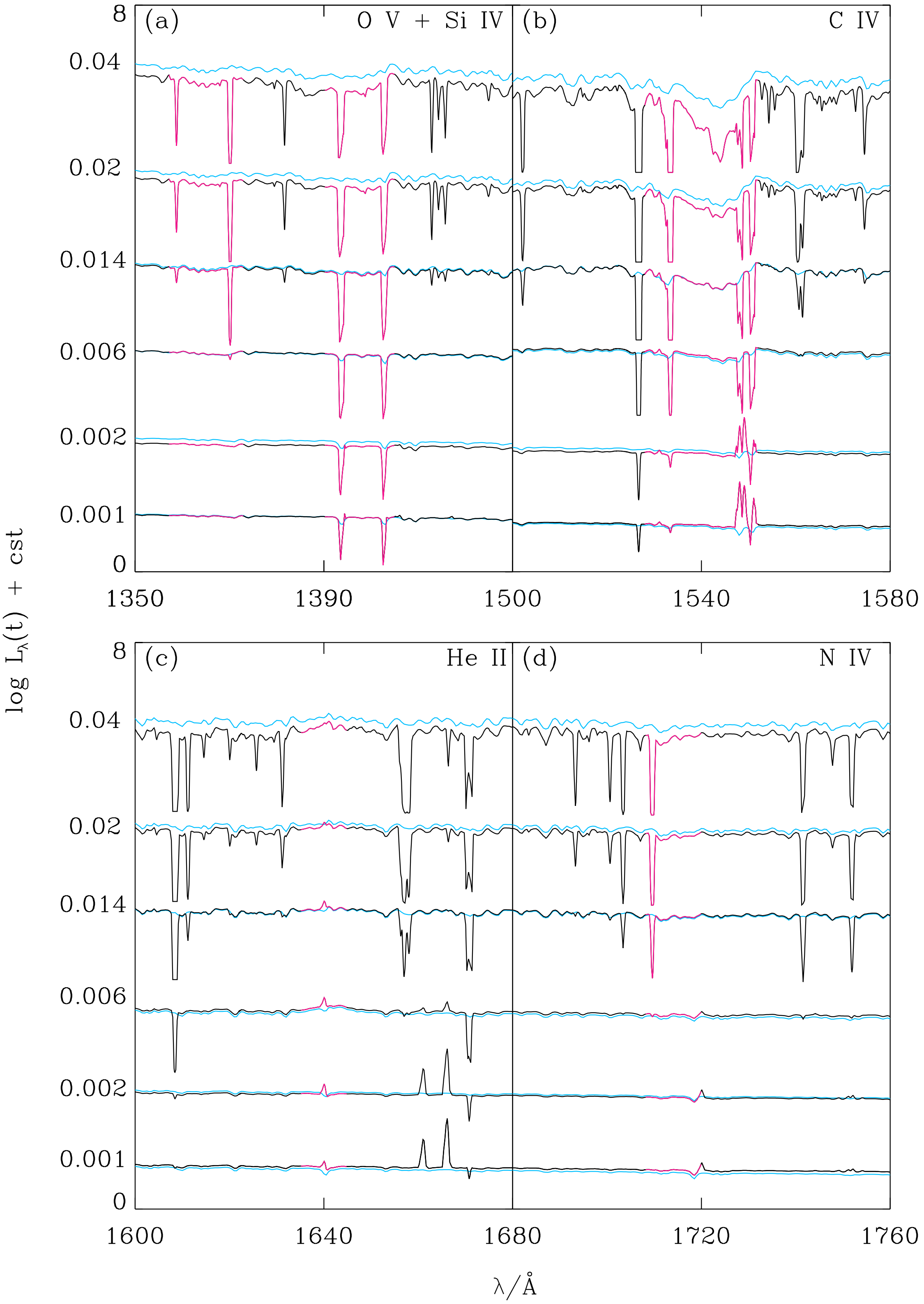

Figure 4.7 – Analog of Fig. 4.6 for young-galaxy models with constant star formation rate and metallicities $Z = 0.001$, 0.002, 0.006, 0.014, 0.02 and 0.04, at fixed age $t' = 10\,\mathrm{Myr}$.

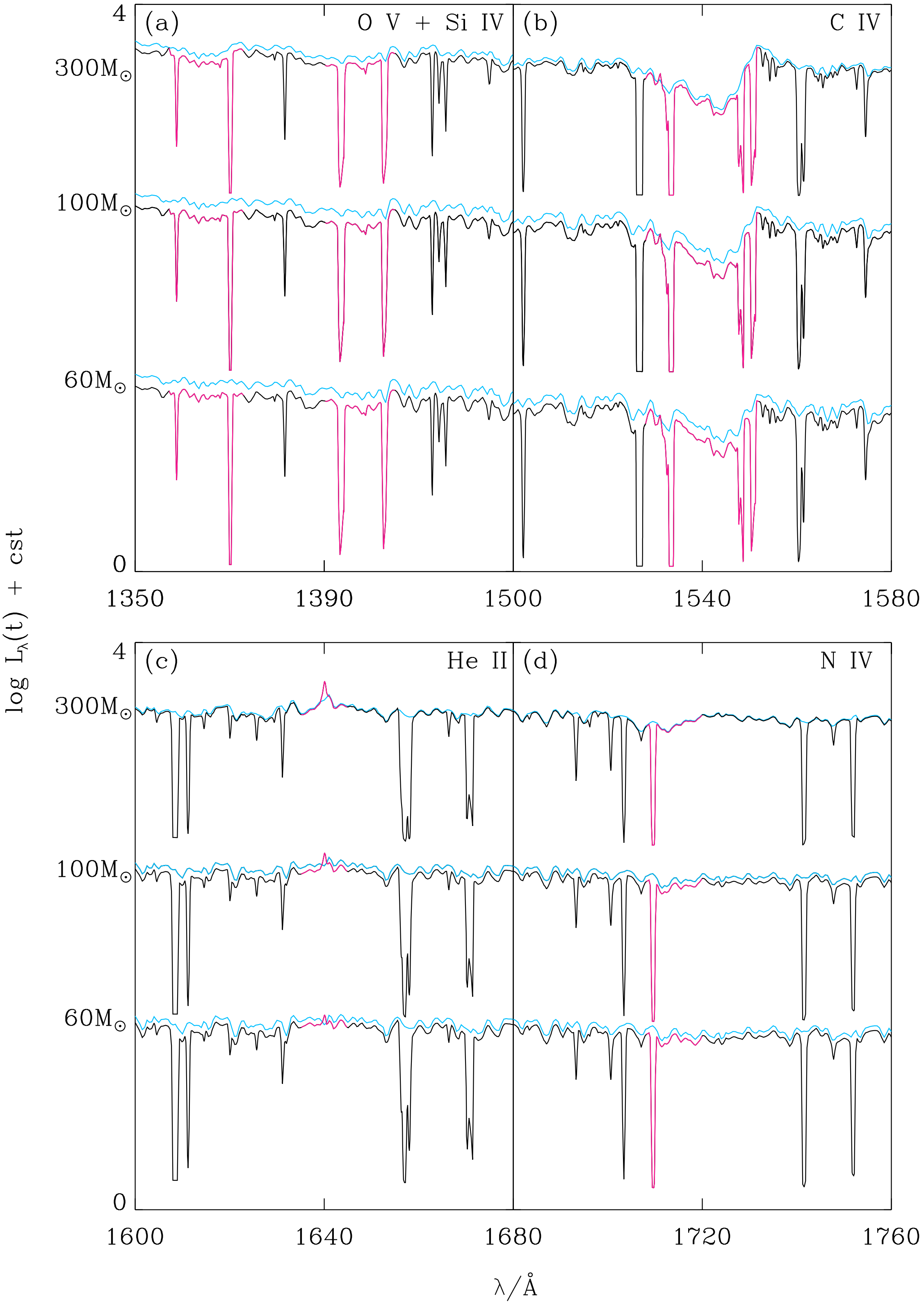

Figure 4.8 – Analog of Fig. 4.6 for young-galaxy models with constant star formation rate and IMF upper mass cutoffs $m_{\rm up} = 60$, 100 and 300 $\mathrm{M}_\odot$, at fixed age $t' = 10\,\mathrm{Myr}$.

the other depends on the competing effects of nebular continuum radiation (most important at 1 Myr) and attenuation by dust (dominating at 3 Myr), the effects of both declining with age. The dependence of stellar features on SSP age t' in Fig. 4.5 confirms previous findings (e.g., Leitherer et al., 1995, see also Wofford et al. 2011 for O V $\lambda1371$). For example, the shape of C IV $\lambda1550$ evolves a strong P-Cygni profile (see Appendix C) characteristic of O-type star winds at early ages to a profile characteristic of B-type star photospheres after 8 Myr (Fig. 4.5b). For Si IV $\lambda1400$, the P-Cygni profile is apparent only at ages between 3 and 8 Myr, consistent with the fact that this line traces high ratios of supergiant-to-main sequence stars (Fig. 4.5a; see Walborn & Panek 1984; Leitherer et al. 1995). Instead, the P-Cygni profiles of O V $\lambda1371$ and N IV $\lambda1719$ are prominent only at ages younger than about 3 Myr, as these lines, which originate from excited energy levels (unlike Si IV $\lambda1400$ and C IV $\lambda1550$), trace the dense winds of the most luminous O and Wolf-Rayet stars (Figs 4.5a,d). Finally, the broad but weak He II $\lambda1640$ emission is formed primarily in fast, dense winds of Wolf-Rayet stars and therefore most visible when these stars are more numerous relative to main-sequence stars, i.e., at SSP ages between roughly 3 and 5 Myr (Fig. 4.5c).

The novelty in Fig. 4.5 relative to previous studies is the ability with the model to compute in a physically consistent way the impact of nebular emission and interstellar absorption on these stellar features. At solar metallicity, nebular emission is weak in the ultraviolet (Fig. 4.1), and the most prominent features arise from interstellar absorption. This includes for example contamination of stellar O V $\lambda1371$ by interstellar Ni II $\lambda1370$ at ages up to 10 Myr, and that of stellar Si IV $\lambda1400$ by interstellar lines of the same element at early ages (in the ionized interior of the birth cloud) and by Ni II $\lambda1393$ up to older ages (in the outer neutral envelope of the cloud; Fig. 4.5a). The most prominent interstellar lines affecting C IV $\lambda1550$ are those of the element itself, which are firstly in emission and then in absorption until they disappear at ages beyond 8 Myr, and absorption by Si II* $\lambda1533$, which remains up to 10 Myr (Fig. 4.5b). He II $\lambda1640$ does not suffer any significant interstellar absorption, and contamination by nebular emission is limited to the brief phase when hot Wolf-Rayet stars are present, between 3 and 5 Myr (Fig. 4.5c). In the case of N IV $\lambda1719$, contamination arises mainly from the off-centred Ni II $\lambda1710$ line, justifying a posteriori the finding in Section 4.2.1 that the Bl 1719 index of Fanelli et al. (1992) may be a useful (although not ideal) tracer of stellar population properties in star-forming galaxies (Fig. 4.5d).

Fig. 4.6 shows the analog of Fig. 4.5 for a young-galaxy model with constant star formation rate and $Z = 0.017$ (the spectrum at age 10 Myr corresponds to the quantity L_λ^{BC} defined by equation 4.12). The transient signatures of evolved supergiant and Wolf-Rayet stars identified in the spectral evolution of an SSP in Fig. 4.5, such as the P-Cygni profile of Si IV $\lambda1400$ and stellar and nebular He II $\lambda1640$ emission, are weaker when the main sequence is constantly replenished in O-type stars (Figs 4.6a,c). In contrast, features found also in O-type stars, such as O V $\lambda1371$, N IV $\lambda1719$ and especially C IV $\lambda1550$, are more pronounced and longer-lived when star formation is maintained at a constant rate (Figs 4.6a,b,d). Perhaps the most noticeable feature in Fig. 4.6 is the steady strength of both high- and low-ionization interstellar absorption lines associated with a steady population of birth clouds at constant star formation rate. This implies a steady contamination of strong stellar lines by neighbouring interstellar lines, in the way described above. Also, in this example, attenuation by dust dominates over nebular recombination radiation at all ages, making the emergent continuum fainter than the input stellar population spectrum.

In Fig. 4.7, I show how the radiation emerging from a 10 Myr-old galaxy with constant star formation rate depends on metallicity, for $0.001 \leq Z \leq 0.04$. I adopt $\log U_{\mathrm{S}} = -2.0$ for $Z = 0.001$ and 0.002, $\log U_{\mathrm{S}} = -3.0$ for $Z = 0.008$ and $\log U_{\mathrm{S}} = -3.5$ for $Z = 0.014$, 0.02 and 0.04 (see Section 4.1.2; the spectrum for $Z = 0.002$ is the same as that shown by the red curve in Fig. 4.1a). The strength of stellar-wind features increases from low to high Z, as expected from the associated enhanced efficiency of radiation pressure on metal lines (e.g., Vink et al., 2001). Lowering Z also leads to a harder ionizing spectrum (since metal-poor stars evolve at higher effective temperatures than metal-rich ones; e.g., fig. 15 of Bressan et al. 2012). Only at the lowest metallicities considered here, $Z \lesssim 0.002$, does nebular recombination radiation make the emergent spectrum slightly brighter than the input stellar-population spectrum, and some nebular lines stand out of the continuum, such as C IV $\lambda1550$ (notched by a small interstellar absorption component; Fig. 4.7b), He II $\lambda1640$ and O III]$\lambda\lambda1661, 1666$ (Fig. 4.7c; the small emission line just blueward of N IV $\lambda1719$ in Fig. 4.7d is in reality the sum of S III] $\lambda\lambda1713, 1729$, which CLOUDY places at 1720 Å). Interstellar absorption develops mainly at high metallicity, although significant Si IV $\lambda1400$ and even Si II $\lambda1526$ absorption arises at $Z \lesssim 0.002$ (Figs 4.7a,b). Fig. 4.7b further shows how, for the ISM parameters chosen here, Si II $\lambda1526$, Si II* $\lambda1533$ and Fe II $\lambda1608$ progressively saturate as metallicity increases.

Fig. 4.8 illustrates the influence of the upper mass cutoff of the IMF on the radiation emerging from a 10 Myr-old galaxy with constant star formation rate and $Z = 0.017$ (for $\log U_\mathrm{S} = -3.5$, as in Fig. 4.6). I show models with $m_\mathrm{up} = 60$, 100 (the standard value adopted throughout this work) and 300 $\mathrm{M}_\odot$. Increasing m_up from 60 to 300 $\mathrm{M}_\odot$ strengthens all wind-line signatures from hot luminous stars, since more massive stars evolve at higher effective temperatures and luminosities than lower-mass stars. This also makes the ionizing spectrum of the stellar population harder, and hence, recombination-continuum and He II $\lambda1640$-line emission stronger. Fig. 4.8 further shows that, in general, interstellar absorption features do not depend sensitively on m_up.

Chapter 5

On statistical tools for galaxy SED-fitting

In this chapter, I summarize the main features of the novel statistical inference tool BEAGLE to interpret galaxy spectra and describe the principal mode in which I make use of this code. Among the comprehensive list of physical parameters that can be constrained, I present the ones I am primarily interested in characterizing.

Contents

5.1 Standard methodology 80
5.2 In this work: BEAGLE. 81

5.1 Standard methodology

In Chapters 2 and 4, we have described how we compute model SEDs of galaxies. Such models are required to interpret the light emitted by galaxies in terms of constraints on physical properties, such as star formation history, chemical enrichment, attenuation by dust, etc. In this chapter, I briefly review the principles of what has now become a standard approach to compare model and observed SEDs: Baeysian statistics. I also describe the main features of the code that I will use in the next chapter to interpret observed galaxy spectra.

Bayes' theorem allows one to perform inference on a set of model parameters by combining information obtained from a given set of data (through the *likelihood function*) with a prior knowledge about these parameters (through the *prior distribution*). We can calculate the posterior probability distribution of the parameters as (e.g., Jeffreys, 1961):

$$P(\Theta \mid D, H) = \frac{P(\Theta \mid H)P(D \mid \Theta, H)}{\int P(\Theta \mid H)P(D \mid \Theta, H)d\Theta}, \tag{5.1}$$

where Θ is a set of parameters of a given model H and D is a set of data. The first term of the numerator is the prior distribution of model H with parameters Θ, the second term is the likelihood distribution (i.e. the probability of observing data D given a model H with parameters Θ) and the denominator is the *evidence* (i.e., the evidence that data D were generated by model H; or marginal likelihood), usually expressed as $P(D \mid H)$.

We already appealed to Bayesian statistics to constrain the ages, metallicities and stellar masses of 10 LMC star clusters in Chapter 3, where we computed the likelihood of an observed set of spectral indices $W^{\rm obs}$ given a model j with parameters Θ^j as expressed by equation (3.3). It is worth noting that the prior probability distribution in equation (5.1) will have a significant impact on the inference results only if the data (entering the equation through the likelihood function) carry poor information. In this case, the prior distribution allows one to propagate ignorance about the parameters in the posterior probability distribution. The constraints derived using equation (5.1) on adjustable parameters are often characterized by the median and 16%–84% credible interval of the posterior probability distribution.

Deriving the posterior probability distribution $P(\Theta \mid D, H)$ favored by a set of observations in the case of a multi-parameter model can be computationally expensive, because of the exponential scaling of computational time with the number of adjustable parameters. A way to reduce computational time is to describe the posterior probability distribution through a set of samples drawn from it. *Markov Chain Monte Carlo* (MCMC) is a general method for sampling from probability distributions. Classical MCMC algorithms are based on the exploration of the parameter space through *random walk*. The random samples are correlated (unlike in conventional Monte Carlo integration) via the construction of a Markov chain with equilibrium distribution $P(\Theta \mid D, H)$. The technique allows a convergence towards the solution in each visited point of the random walk, reducing the computational time considerably.

One of the most widely used methods to explore the parameter space is the *Metropolis-Hastings* algorithm (Metropolis et al., 1953; Hastings, 1970). The algorithm consists in an iterative exploration of the parameter space in a random walk with the goal of converging onto the target distribution. The exploration starts with a set of initial parameters, which are generally drawn randomly from the prior distribution. At each iteration, a new set of parameters is drawn based on the current one (by sampling from a distribution centered around the current parameter values with a predefined width). If the probability $[P(\Theta \mid H)P(D \mid \Theta, H)]$ of the new candidate set of parameters is greater than that of the current one, the candidate set can be accepted and used in the following iteration. Otherwise, the probability of acceptance is determined through the ratio of probabilities of the new and current sets (for example, if the current set is twice as probable, there will be a 50% chance of accepting the new set). The reason for sometimes accepting sets of parameters corresponding to lower probability is to properly sample the posterior probability distribution.

An alternative algorithm to explore the parameter space is called *Nested Sampling* (Skilling, 2006). This consists in exploring the parameter space in a stochastic way by making use of a set of *active points* (each corresponding to a set or parameters Θ). At each iteration, these active points reduce exponentially the volume from which new samples are drawn around the regions of highest probability. Specifically, at each iteration, the algorithm computes the likelihood of N points uniformly drawn from the prior distribution. The point with lowest likelihood is removed, and a new point is drawn from the prior volume with the requirement that its likelihood be greater than that of the removed point. A technical difficulty in this procedure is to efficiently draw points satisfying the likelihood criterion, since the volume occupied by these parameters reduces exponentially with the number of iterations. This issue can be solved by appealing to a method called *simultaneous ellipsoidal nested sampling method* (Feroz et al., 2009). This technique allows the approximation of iso-likelihood surfaces in the prior volume with ellipsoids, whose optimal number and bounds are determined by an expectation-maximisation algorithm.

5.2 In this work: BEAGLE.

In this work, I make use of the recently published spectral interpretation tool BEAGLE (Chevallard & Charlot, 2016) to derive statistical constraints on physical parameters from observations of ultraviolet and optical galaxy spectra. To this end, I briefly summarize the main features of the code in the next paragraphs, while the results of the spectral fits will be presented in Chapter 6.

BEAGLE is a new-generation spectral analysis tool, which can be used both to produce mock catalogs of galaxy spectra and to model and interpret galaxy SEDs. It allows one to combine, in a physically consistent way, different prescriptions for the production of starlight in galaxies and its transfer through the ISM (absorption and emission by gas, attenuation by dust) and the intergalactic medium (IGM; absorption by gas). This tool also allows one to interpret any combination of photometric and spectroscopic galaxy observations in terms of physical parameters. The current version of the tool includes flexible modeling of the emission from stars and photoionized gas, attenuation by dust and accounting for different instrumental effects, such as spectroscopic flux calibration and line spread function. The tool also includes several possible prescriptions to describe the star formation and chemical enrichment histories of galaxies via a set of versatile modules. Other modules to be implemented in the future include infrared emission from dust, emission from an AGN and absorption by interstellar gas (based on the work described in Chapter 4 of this thesis).

The BEAGLE tool performs statistical inference on physical parameters from observed galaxy samples. The adopted Bayesian approach includes: (i) the computation of realistic uncertainties in physical parameters by a rigorous propagation of observational errors; (ii) the proper characterization of correlations among model parameters to deal with parameter degeneracies; and (iii) accounting for instrumental effects to minimize the impact of these on inference results.

Fig 5.1 summarizes the main building blocks of the BEAGLE tool to produce mock catalogs of galaxy spectra and interpret observed galaxy SEDs, the utility in which I am primarily interested in this work. The main ingredients used to define a galaxy model are shown at the top, and the workflow diagram illustrates how the light emerging from a galaxy is processed to include IGM absorption and instrumental effects, before proceeding with spectral interpretation and catalog production.

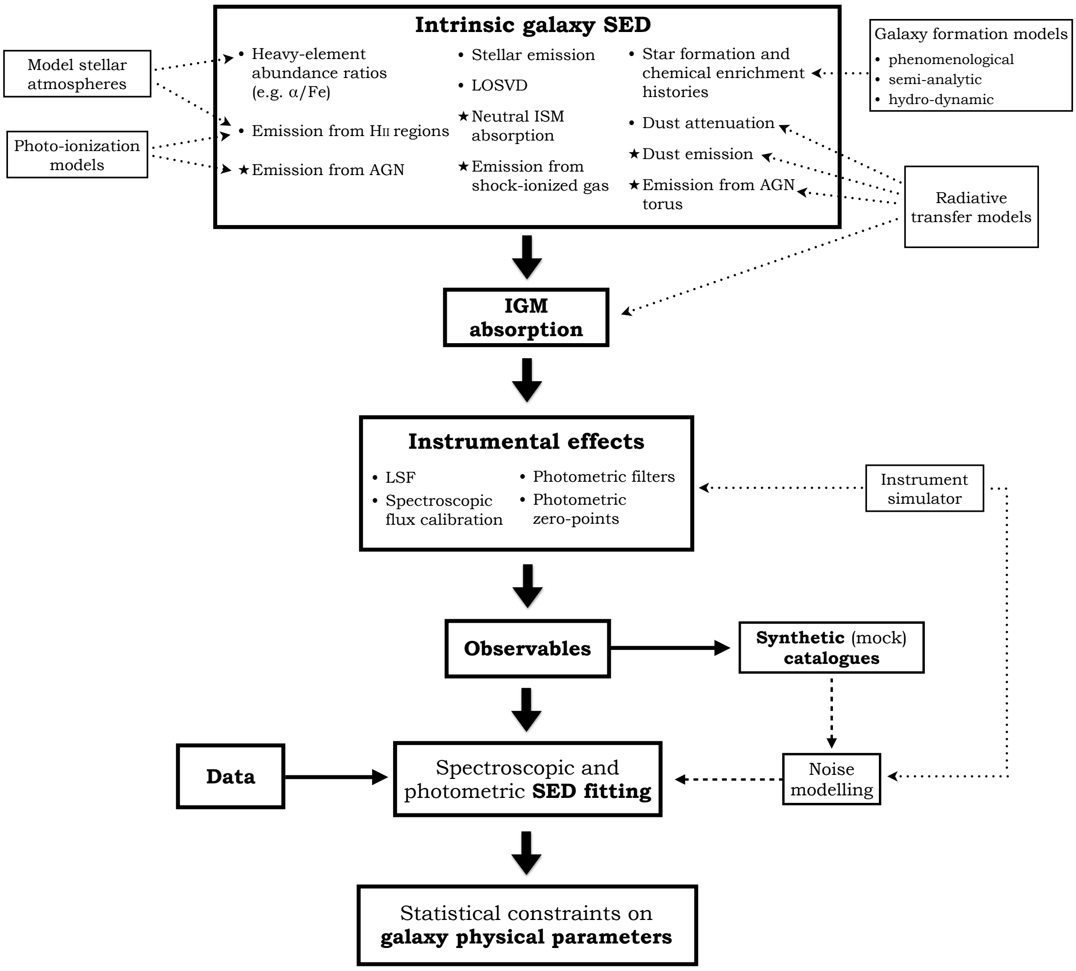
Intrinsic galaxy SED
• Heavy-element abundance ratios (e.g. α/Fe)
• Emission from HII regions
★Emission from AGN
• Stellar emission
• LOSVD
★Neutral ISM absorption
★Emission from shock-ionized gas
• Star formation and chemical enrichment histories
• Dust attenuation
★Dust emission
★Emission from AGN torus
Model stellar atmospheres
Photo-ionization models
Galaxy formation models
• phenomenological
• semi-analytic
• hydro-dynamic
Radiative transfer models
IGM absorption
Instrumental effects
• LSF
• Spectroscopic flux calibration
• Photometric filters
• Photometric zero-points
Instrument simulator
Observables
Synthetic (mock) catalogues
Data
Spectroscopic and photometric SED fitting
Noise modelling
Statistical constraints on galaxy physical parameters

Figure 5.1 – Workflow diagram showing the main ingredients of BEAGLE; dotted arrows indicate how external models can inform the various ingredients. Credit: Chevallard & Charlot (2016)

BEAGLE allows one to constrain different types of galaxy parameters, described in Table 2 of Chevallard & Charlot (2016), to which I refer for details. An adjustable model parameter can be chosen to be either *free*, *fixed* or *dependent*. A free parameter is drawn from a prior probability distribution; a fixed parameter is assumed take a default (standard) value, i.e., corresponding to a δ-Dirac prior probability distribution; and a dependent parameter is assumed to depend on other parameters (for example, through an analytic relation), in which case it is also drawn from a δ-Dirac prior probability distribution, only conditional on the values of other parameters. The adjustable parameters of the BEAGLE tool I will focus on in the next chapter are the following.

Parameters related to the **star-formation** and **chemical enrichment histories**, described as a succession of a flexible number of star formation periods (the time dependence of the star formation and chemical enrichment rates in these components can be drawn from analytic functions or from different flavors of galaxy formation models, such as phenomenological and semi-analytic models and hydro-dynamic simulations):

- $t_{\rm start}$/Gyr and $t_{\rm end}$/Gyr: start/end look-back times of an arbitrary number of star formation periods (the $t_{\rm start}$ value of the first star formation period is also the age of the oldest stars in a model galaxy, called $t_{\rm star}$). These are defined in the range $[0, t_z]$, where t_z is the age of the Universe at redshift z;

- $M/{\rm M}_\odot$: mass of the stars formed during a star-formation period, defined in the range $[0, 10^{12}]$;
- $\tau_{\rm SFR}/{\rm Gyr}$: star formation timescale during a star-formation period (for analytic star formation histories like exponentially declining, delayed, rising, etc.). It can be defined in the range $[0.01, 2 \times t_z]$;
- $\log(Z/Z_\odot)$: metallicity of stars formed during a star formation period, defined in the range $[-2, 0.25]$;
- $\log(\psi_{\rm S}/{\rm yr}^{-1})$: specific star formation rate (averaged over the duration of the 'current' episode of star formation, $\Delta t_{SFR} \in [10^7, 10^8]\,{\rm yr}$), defined in the range $[-12, -7]$.

Parameters related to **nebular emission**:

- $\log U$: effective (i.e. galaxy-wide) ionization parameter, defined in the range $[-4, -1]$;
- ξ_d: effective (i.e. galaxy-wide) dust-to-metal mass ratio, defined in the range $[0.1, 0.5]$.

Parameters related to **dust attenuation** and **kinematics**:

- $\hat{\tau}_V$: V-band attenuation optical depth, defined in the range $[0, 5]$;
- $\sigma/{\rm km\,s^{-1}}$: velocity dispersion (different values can be adopted to describe the line-of-sight velocity dispersions of stellar and nebular emission), defined in the range $[0, 400]$.

To compute the posterior probability distribution of the above parameters favored by a set of observations, the BEAGLE tool appeals to MULTINEST, an efficient Bayesian-inference tool based on the Nested Sampling algorithm (see Section 5.1).

The outputs produced by the code are organized in FITS files with multiple extensions, each of which contains information about a physical module, such as star formation and chemical enrichment histories, dust attenuation, nebular emission and kinematics. Details about the format and a complete set of derived parameters and other useful information to run the code can be found in the user's manual, available from http://www.jacopochevallard.org/beagle/.

Chapter 6

Results from galaxy SED-fitting with BEAGLE

In this chapter, I use the BEAGLE tool described in the previous chapter to derive constraints on physical properties of star-forming galaxies observed in the local and distant Universe with *HST* and the Keck I telescope, using different sets of observables.

Contents

6.1 Lyα and C III] emission in $z = 7-9$ galaxies: accelerated reionization around luminous star-forming systems? 86
6.2 The three most metal-poor nearby galaxies 90
6.3 10 nearby galaxies with hard optical spectra 95

6.1 Lyα and C III] emission in $z = 7 - 9$ galaxies: accelerated reionization around luminous star-forming systems?

This Section is extracted from the recently published paper *Lyα and C III] emission in $z = 7 - 9$ galaxies: accelerated reionization around luminous star-forming systems?* by Stark et al. (2016). In this paper, we use the BEAGLE tool to interpret observed spectra of three galaxies at redshifts $z > 7$, which exhibit Lyα in emission. Such emission is quite surprising, because the intergalactic medium is expected to be significantly neutral over the redshift range $7 < z < 9$, leading to the absorption of Lyα photon escaping from young galaxies. The motivation for our study was that observations of ultraviolet metal lines in these galaxies should shed some light on the way in which the ionizing field affects local environment to allow the transfer of Lyα photons. In fact, for the galaxy in which we could detect C III] emission (EGS-zs8-1), the centroid of the line shows that Lyα is redshifted by 340 $\mathrm{km\,s^{-1}}$, a higher velocity offset than that seen in less luminous objects. This finding suggests that the visibility of Lyα is strongly luminosity dependent, with transmission accelerated in systems with intense star formation.

The thee galaxy spectra analyzed with BEAGLE in this study were obtained from observations with the near-infrared multi-object spectrograph MOSFIRE (McLean et al., 2012) on the Keck I telescope of three of the four luminous galaxies at $z = 7 - 9$ selected photometrically in the CANDELS fields by Roberts-Borsani et al. (2016) to have intense optical-line emission (because of contamination of the observed 4.5μm flux by rest-frame [O III]+Hβ emission). The galaxies, and the observations that could be carried out in good weather conditions, are: EGS-zs8-1, observed in the H band to target the [C III]λ1907+C III]λ1909 doublet (hereafter simply C III]), Lyα having already been detected in this object (Oesch et al., 2015); EGS-zs8-2, observed in Y and H bands to target Lyα and C III]; and COS-zs7-1, observed in Y band to target Lyα. The results of these observations can be summarized as follows.

- EGS-zs8-1: bright ($H_{160} = 250$) galaxy with a red IRAC color ([3.6]-[4.5]=0.53 ± 0.09), for which the excess of 4.5μm flux suggests a very large rest-frame equivalent width of [O III]+Hβ emission. Oesch et al. (2015) confirmed its spectroscopic redshift, giving a value $z_{\mathrm{Ly}\,\alpha} = 7.73$. The Ly$\alpha$ line flux ($1.7 \times 10^{-17}\mathrm{erg\,cm^{-2}s^{-1}}$) is one of the largest among $z > 7$ galaxies and suggests an equivalent width $W_{\mathrm{Ly}\alpha} \approx 21$ Å. Its absolute ultraviolet magnitude also indicates an unusually luminous galaxy, roughly 3 times larger than the value of L^*_{UV} derived from the Schechter-parameter fitting functions presented in Bouwens et al. (2015).

  The MOSFIRE H-band spectrum of EGS-zs8-1 covers the wavelength range from 1.5154 to 1.8223 μm. In Fig. 6.1, the narrow spectral window between 1.650 and 1.675 μm is shown, revealing a clean detection of both components of the C III] doublet. The observed fluxes are $4.5 \pm 0.5 \times 10^{-18}$ and $3.6 \pm 0.5 \times 10^{-18}$ $\mathrm{erg\,cm^{-2}s^{-1}}$ for the 1907 and 1909 Å components, respectively. The total flux in the resolved C III] doublet is close to 50% of that of Lyα, nearly 10 times greater than what is seen in the most extreme C III]-emitting galaxies at lower redshift (e.g. Erb et al., 2010; Stark et al., 2014).

- EGS-zs8-2: bright ($H_{160} = 25.1$) galaxy identified in CANDELS imaging by Roberts-Borsani et al. (2016), for which the redder IRAC color ([3.6]-[4.5]=0.96 ± 0.17) reflects even more extreme optical-line emission than in EGS-zs8-1 (the [O III]+Hβ equivalent width being estimated around 1610 ± 302 Å).

  The 7.4 σ emission feature at 1.0305 μm in the Y-band spectrum shown in Fig. 6.2a confirms that this object is a Lyα emitter at $z_{\mathrm{Ly}\alpha} = 7.4774$. The line flux and equivalent width are $7.4 \pm 1.0 \times 10^{-18}\mathrm{erg\,cm^{-2}s^{-1}}$ and $W_{\mathrm{Ly}\alpha} = 9.3 \pm 1.4$ Å, the smallest of the Roberts-Borsani

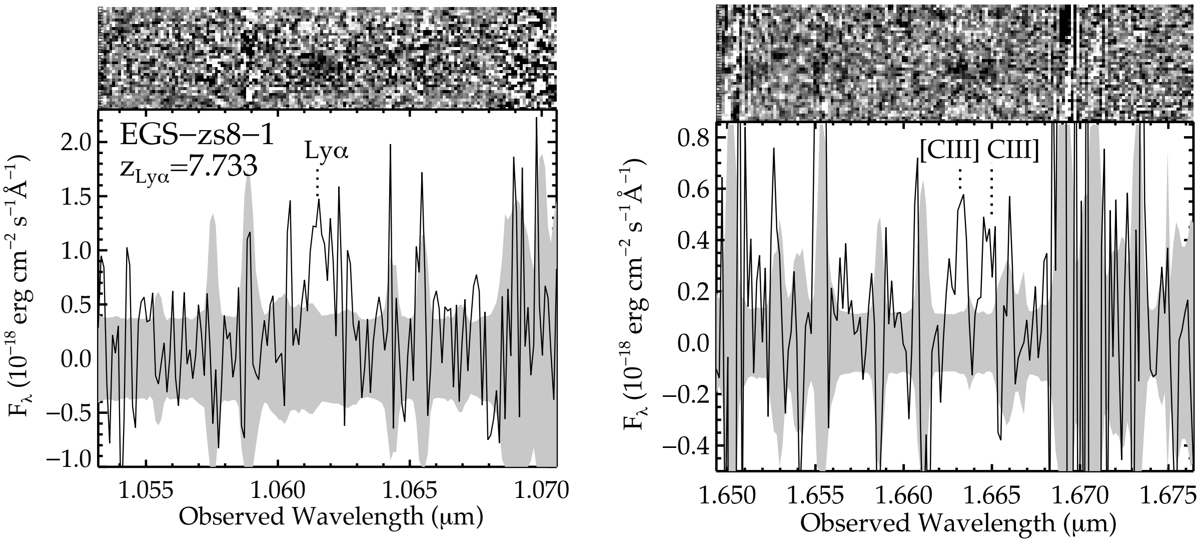

Figure 6.1 – Keck/MOSFIRE spectra of EGS-zs8-1, a $z = 7.733$ galaxy that was originally spectroscopically confirmed in Oesch et al. (2015). (Left:) Two-dimensional and one-dimensional Y-band spectra centered on the Lyα emission line. Data are from Oesch et al. (2015). (Right:) H-band observations showing detection of the [C III]λ1907+C III]λ1909 doublet. The top panels show the two-dimensional signal-to-noise ratio maps (black is positive), and the bottom panels the flux-calibrated one-dimensional extractions. Credit: Stark et al. (2016).

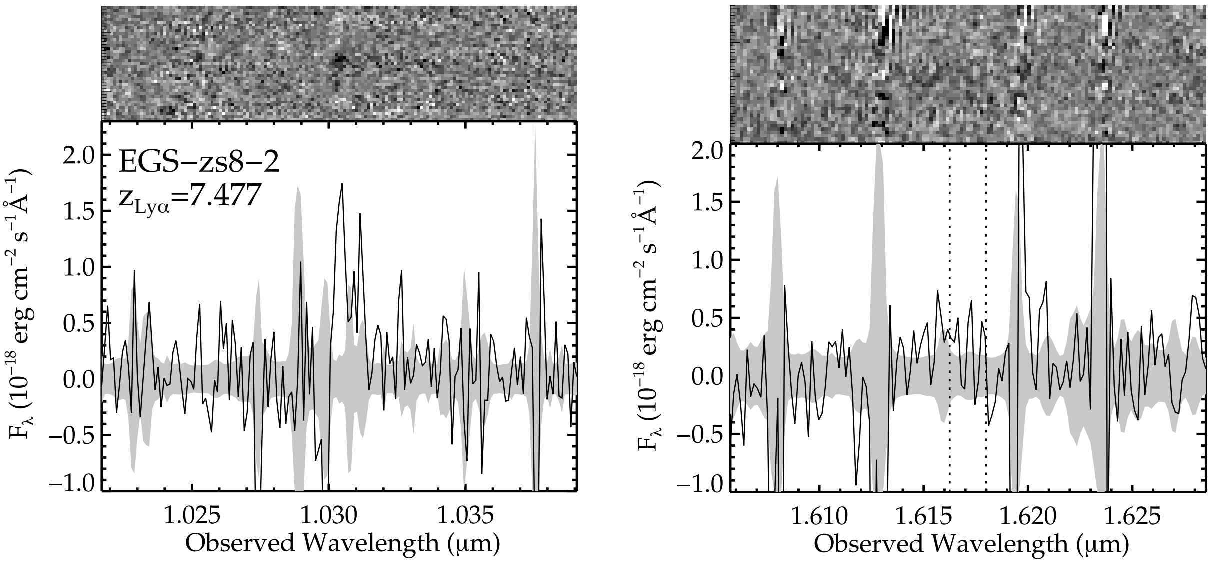

Figure 6.2 – Keck/MOSFIRE spectra of EGS-zs8-2, a $z = 7.477$ galaxy presented in Roberts-Borsani et al. (2016). (Left:) Two-dimensional and one-dimensional Y-band spectra centered on the Lyα emission line, confirming the tentative redshift identification presented in Roberts-Borsani et al. (2016). (Right:) H-band observations showing non-detection of the [C III]λ1907+C III]λ1909 doublet. The top panels show the two-dimensional signal-to-noise ratio maps (black is positive), and the bottom panels the flux-calibrated one-dimensional extractions. Credit: Stark et al. (2016).

et al. (2016) sample. The MOSFIRE H-band spectrum covers rest-frame wavelengths from 1720 to 2113 Å for this object. We show the spectral window in Fig. 6.2b, where no emission line is visible. This non-detection suggests that the flux in the C III] doublet is less than 62% of that in Lyα, corresponding to a $3\,\sigma$ upper limit on the equivalent width $W_{\mathrm{CIII]}} < 14$ Å.

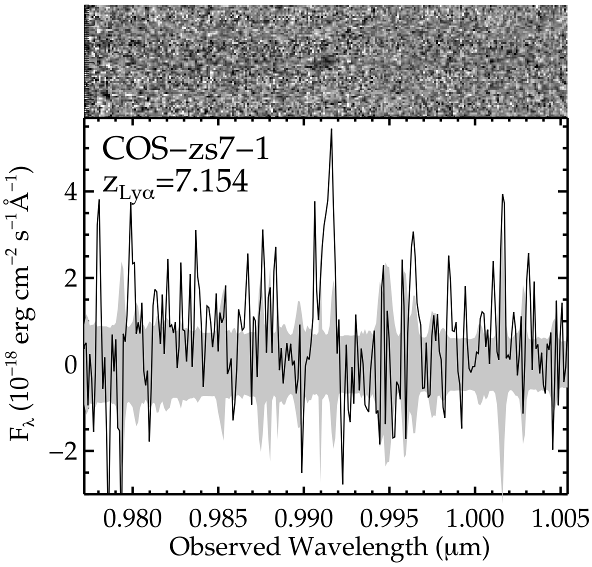

Figure 6.3 – Keck/MOSFIRE Y-band spectrum of COS-zs7-1, a bright ($H = 25.1$) dropout presented in Roberts-Borsani et al. (2016). We identify an emission feature at the spatial position of the dropout at 9913Å, which is likely to be Lyα at $z = 7.154$. The top panel shows the two-dimensional signal-to-noise ratio map (black is positive), and the bottom panel the flux-calibrated one-dimensional extraction. Credit: Stark et al. (2016).

- COS-zs7-1: bright ($H_{160} = 25.1$) galaxy with an extreme IRAC color ([3.6]-[4.5]=1.03±0.15) indicating intense optical-line emission. Based on this excess, the estimated [O III]+Hβ equivalent width of 1854 ± 325 Å makes it the most extreme optical-line emitter in the sample of Roberts-Borsani et al. (2016), at a photometric redshift $z_{\mathrm{phot}} = 7.14 \pm 0.12$.
  We interpret the single emission line in the Y-band spectrum shown in Fig. 6.3 as Lyα at redshift $z_{Ly\alpha} = 7.154$. The derived total flux of this line is $2.5 \pm 0.4 \times 10^{17}$erg cm^{-2}s^{-1}, and the equivalent width $W_{\mathrm{Ly}\alpha} = 28 \pm 4$ Å.

We use the BEAGLE tool to interpret these observations (emission-line and broadband fluxes) in terms of constraints on galaxy physical parameters. The version of the code used in this work relies on the models of Gutkin et al. (2016) to describe stellar and nebular emission (we do not model here interstellar absorption, the ultraviolet continuum not being detected in these objects). The main adjustable parameters of the photoionized gas are the interstellar metallicity, Z_{gas}, the typical ionization parameter of newly ionized H II regions, U_{S}, and the dust-to-metal mass ratio, ξ_{d} (see Section 4.1.1). The models considered here have hydrogen density $n_{\mathrm{H}} = 100\,\mathrm{cm}^{-3}$ and C/O (and N/O) abundance ratios ranging from 1.0 to 0.5 times the standard values in nearby galaxies [$(\mathrm{C/O})_\odot \approx 0.44$ and $(\mathrm{N/O})_\odot \approx 0.07$]. Attenuation by dust is described using the 2-component model of Charlot & Fall (2000), combined with the Chevallard et al. (2013) 'quasi-universal' prescription to account for the effects linked to dust/star geometry (including ISM clumpiness) and galaxy inclination. Finally, the prescription of Inoue et al. (2014) is adopted to include absorption by the IGM.

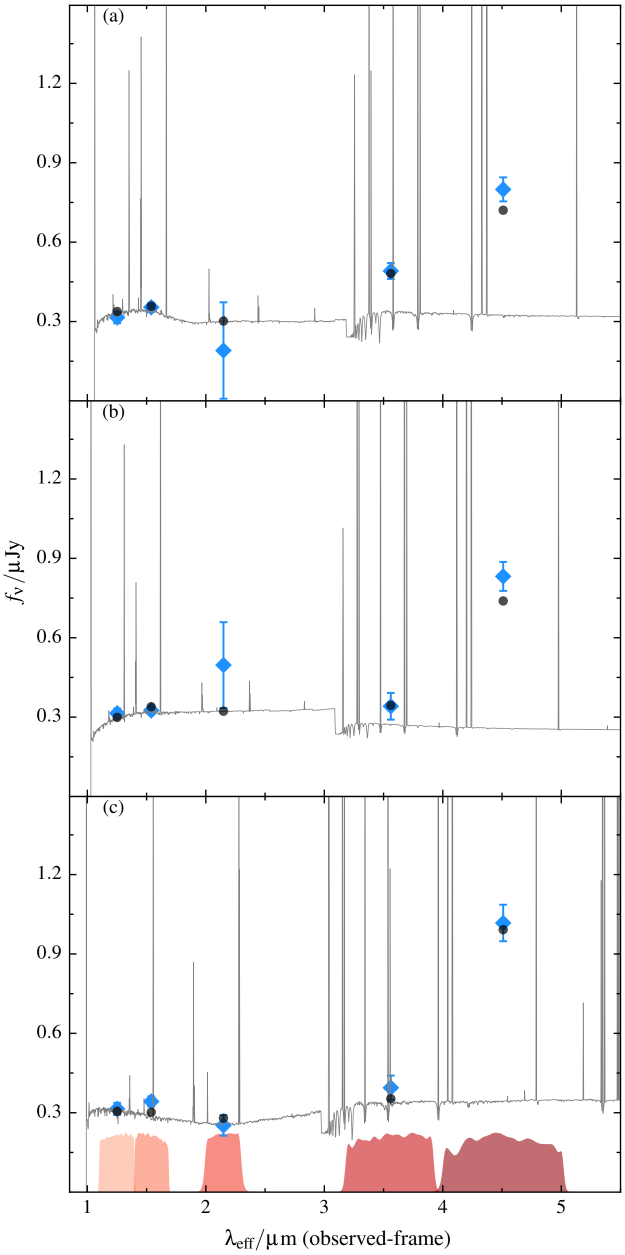

Figure 6.4 – Spectral energy distributions of EGS-zs8-1 (panel a), EGS-zs8-2 (panel b), and COS-zs7-1 (panel c). The best-fitting BEAGLE SED models are overlaid. Blue diamonds show the observed photometry reported in Roberts-Borsani et al. (2016). The black circles show the synthetic photometry from BEAGLE. Credit: Stark et al. (2016).

We parametrize the star formation histories of model galaxies in BEAGLE as exponentially delayed functions (see Sections 2.3 and 5.2), for star formation timescales in the range $7 \leqslant \log(\tau_{\rm SFR}/{\rm yr}) \leqslant 10.5$ and formation redshift in the range $z_{\rm obs} \leqslant z_{\rm form} \leqslant 50$ (where $z_{\rm obs}$ is the observed galaxy redshift). We adopt a standard Chabrier (2003) initial mass function and assume that all stars in a given galaxy have the same metallicity, in the range $-2.2 \leqslant \log(Z/Z_\odot) \leqslant 0.25$. We superpose on this smooth exponential function a current burst with a fixed duration of 10 Myr, whose strength is parametrized in terms of the specific star formation rate, in the range

$-14 \leqslant \log(\psi_S/\mathrm{yr}^{-1}) \leqslant -7$. We adopt the same metallicity for the gas as for the stars ($Z_{\mathrm{gas}} = Z$), a fixed (intermediate) dust-to-metal mass ratio ($\xi_d = 0.3$), and let the ionization parameter freely vary in the range $-4 \leqslant \log U_S \leqslant -1$. We consider V-band dust attenuation optical depths in the range $-3 \leqslant \log \hat{\tau}_V \leqslant 0.7$ and fix the fraction of this arising from dust in the diffuse ISM rather than in giant molecular clouds at $\mu = 0.4$ (Wild et al., 2011).

With this parametrization, we use BEAGLE to fit the available constraints on the Lyα equivalent width (taken as a lower limit, because of the uncertainties related to enhanced absorption induced by resonant scattering), [C III]λ1907+C III]λ1909 equivalent width and broadband F125W, F140W, F160W and IRAC 3.6 μm and 4.5 μm fluxes of the galaxies in the sample. We obtain as output the posterior probability distributions of the above free model parameters, as well as those of a large collection of derived parameters, such as for example the production rate of hydrogen ionizing photons per observed (i.e. attenuated) 1500 Å luminosity, ξ_{ion}. In practice, we find that including the lower limit on the Lyα equivalent width is important to characterize the typically high specific star formation rates of the galaxies.

As Fig. 6.4 shows, this modeling procedure allows us to successfully reproduce the broadband SEDs of the galaxies. The models matching the large flux excess in the IRAC [4.5] filter have very large specific star formation rates ($\psi_S \approx 7$–24 Gyr^{-1}), indicating a population undergoing rapid stellar-mass growth. The implied interstellar metallicities are in the range $Z = 0.0016$–0.0026, i.e. equivalent to 0.10–0.1 $Z_\odot$ when using the present-day solar metallicity value $Z_\odot = 0.01524$ (Bressan et al., 2012). Because of the depletion of metals onto dust grains, the gas-phase metallicity will be lower than the total interstellar metallicity. After accounting for the depleted values using the method described in Gutkin et al. (2016), we find the gas-phase oxygen abundance to be 12+log O/H = 7.76, 7.77 and 7.97 for COS-zs7-1, EGS-zs8-1 and EGS- zs8-2, respectively. These values correspond to a solar C/O ratio. The detection of carbon emission lines in the spectrum of EGS-zs8-1 allows us to consider variations in this ratio, for which we also consider a value of $0.52(\mathrm{C/O})_\odot$. A visual analysis of the maximum-a-posteriori spectral energy distributions, and a comparison of the Bayesian evidence obtained with the two settings, indicates a slight preference of the model corresponding to $0.52(\mathrm{C/O})_\odot$, which exhibits a (marginally) larger specific star formation rate and a lower metallicity than the model with scaled-solar C/O. Finally, as expected for galaxies dominated by such young and sub-solar stellar populations, the models suggest very large Lyman-continuum photon production efficiencies, $\log \xi_{\mathrm{ion}}$ [erg^{-1}Hz] $\simeq 25.6$, indicating that these galaxies have intense radiation fields.

6.2 The three most metal-poor nearby galaxies

The following are some preliminary results obtained in the context of a successful proposal, which our group submitted for the *HST* Cycle 22 observations. This effort, coordinated by Aida Wofford, includes a few people from the NEOGAL team (S. Charlot, A. Feltre, A. Wofford and me) and an external collaborator (D. Stark, Steward Observatory). The complete analysis will be presented in a paper currently in preparation. In this Section, I summarize the science goals we want to achieve and the fitting techniques used to derive the first preliminary results, in which I am actively involved.

We proposed to use the medium-resolution gratings G160M and G185M of the Cosmic Origin Spectrograph (COS) on board *HST* to obtain spectroscopic observations of a combination of the cosmologically important features C IV $\lambda\lambda$1548, 1551, He II λ1640, O III]$\lambda\lambda$1661, 1666, [Si III]λ1883+Si III]λ1892 and [C III]λ1907+C III]λ1909, in the three most metal-poor star-forming dwarf galaxies known within 50 Mpc. These galaxies approach primeval interstellar and stellar conditions. The spectral resolution of these observations (about $20\,\mathrm{km\,s^{-1}}$) represents an order-of-magnitude improvement over existing *HST* data and allows us to disentangle stellar, nebular, and/or shock components to the lines. The high-quality constraints obtained with these data will allow us to assess the reliability of competing spectral models of star-forming galaxies. This will ensure that the best possible studies of early chemical enrichment of the Universe can be achieved. These observations appear necessary to minimize large existing systematic uncertainties in the determination of high-redshift galaxy properties that *JWST* was in large part designed to measure.

As mentioned in Section 6.1, for most star-forming galaxies in the era of reionization (at $z \gtrsim 7$), Lyα is expected to be severely attenuated by the partially neutral IGM, making the detection of a combination of ultraviolet emission features, such as C IV $\lambda\lambda1548, 1551$, O III]$\lambda\lambda1661, 1666$ and [C III]$\lambda1907$+C III]$\lambda1909$, a more promising way to secure redshifts and extract constraints on the physical properties of young metal-poor galaxies (Stark et al., 2014). Even if in the last few years, *HST* imaging has allowed measurements of photometric redshifts of about 200 galaxies above $z > 7$, spectroscopic-redshift measurements through detection of Lyα emission have led to minimal progress. *JWST* will be able to detect rest-frame optical lines in $z \sim 7 - 9$ galaxies, but at $z > 10$, the observations will be limited to the rest-frame ultraviolet. Therefore, to confirm $z \sim 10 - 15$ galaxies with *JWST*, we will need the detection of metal lines. Indeed, dwarf metal-poor star-forming galaxies at redshifts $z \sim 2 - 3$, which can be considered to some extent as reionization-era analogs, nearly always exhibit a combination of these lines (Stark et al., 2014).

Nearby, very low-metallicity dwarf star-forming galaxies are the most natural test ground for new-generation spectral evolution models, whose purpose is to constrain fundamental properties of primeval galaxies. This is because such nearby galaxies have low masses and metallicies similar to those observed in $z \sim 2 - 3$ galaxies (e.g. Stark et al., 2014). In addition, nearby metal-poor galaxies host populations of recently formed hot stars with masses greater than 5 $\mathrm{M}_\odot$, which have all their diagnostic lines in the ultraviolet spectral region.

Our aim in this work is to build an empirical spectroscopic dataset of the three most metal-poor galaxies within ~50 Mpc, namely SBS-0335-052, UGC-5340 and UGCA-166 (mostly known as I Zw 18), covering the spectral range of the features C IV $\lambda\lambda1548, 1551$, He II $\lambda1640$, O III]$\lambda\lambda1661, 1666$, [Si III]$\lambda1883$+Si III]$\lambda1892$ and [C III]$\lambda1907$+C III]$\lambda1909$ at high spectral resolution. We will use this dataset to characterize the properties of the above lines together with the ultraviolet stellar continuum. The properties of these features will be used to pursue the following goals: (i) disentangle stellar, nebular, and/or shock contributions to emission lines and determine the effects of attenuation by dust; (ii) extract fundamental stellar-population and ISM properties; and (iii) test competing stellar population synthesis prescriptions in detail and constrain galaxy spectral evolution models.

We have started to fit the spectrum of one of the three galaxies in the sample, SBS-0335-052, expected to be a very metal-poor galaxy with an oxygen abundance of $12 + \log(\mathrm{O/H}) = 7.33$ (Izotov et al., 1997). After correcting the data for contamination by Galactic interstellar absorption lines, we fitted all the available pixels in the ultraviolet spectral region using the same version of the BEAGLE tool as described in Section 6.1. Since this version does not yet incorporate the ISM absorption prescription described in Chapter 4, we masked the pixels showing prominent interstellar absorption lines in the data, such as C II $\lambda1335$, Si IV $\lambda\lambda1394, 1403$, Si II $\lambda1526$, C IV $\lambda\lambda1548, 1551$ and Al II $\lambda1671$, excluding them from the fit. The models considered here have hydrogen density $n_\mathrm{H} = 100\,\mathrm{cm^{-3}}$ and the standard C/O (and N/O) abundance ratios in nearby galaxies [$(\mathrm{C/O})_\odot \approx 0.44$ and $(\mathrm{N/O})_\odot \approx 0.07$]. As in the previous section, we also account by dust attenuation using the 2-component model of Charlot & Fall (2000), combined with the

Chevallard et al. (2013) 'quasi-universal' prescription to account for the effects linked to dust/star geometry (including ISM clumpiness) and galaxy inclination.

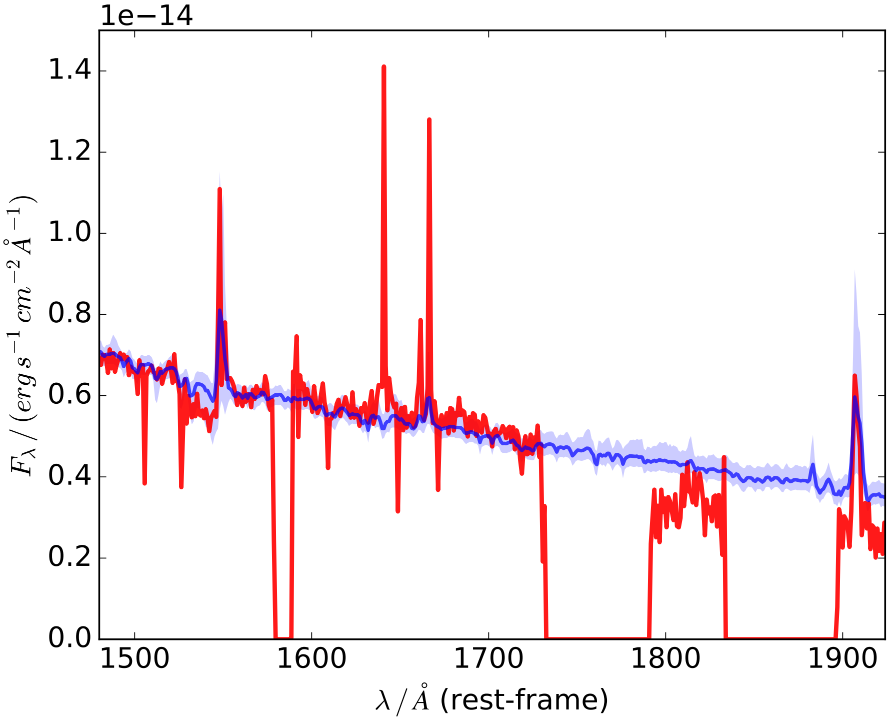

Figure 6.5 – Fitting of the galaxy SBS-0335-052. In red the observed spectrum is shown and in blue the best-fitting model.

As a first try, we may adopt constant star formation rate for the galaxy models in this case, since we consider only ultraviolet emission (see Sections 2.3 and 5.2; I plan to explore more complex star formation histories next). We adopt a standard Chabrier (2003) initial mass function and assume that all stars in a given galaxy have the same metallicity, in the range $-2.2 \leqslant \log(Z/Z_\odot) \leqslant 0.24$. We adopt the same metallicity for the gas as for the stars ($Z_{\mathrm{gas}} = Z$), a fixed (intermediate) dust-to-metal mass ratio ($\xi_{\mathrm{d}} = 0.3$), and let the ionization parameter freely vary in the range $-4 \leqslant \log U_{\mathrm{S}} \leqslant -1$. We consider V-band dust attenuation optical depths in the range $-3 \leqslant \log \hat{\tau}_V \leqslant 0.7$ and fix the fraction of this arising from dust in the diffuse ISM rather than in giant molecular clouds at $\mu = 0.4$ (Wild et al., 2011). Finally we assume that the stellar velocity dispersion is defined in the range $30 \leqslant \sigma(\mathrm{km\,s^{-1}}) \leqslant 200$. With this parametrization, we use BEAGLE to fit the available spectral regions free of interstellar absorption lines. We obtain as output the posterior probability distribution of the above free model parameters.

Fig. 6.5 shows the observed SBS-0335-052 spectrum (in red) along with the best-fitting model spectrum (in blue). The observed spectrum shows clear detections of C IV $\lambda\lambda1548, 1551$ (blend; hereafter C IV $\lambda1550$), He II $\lambda1640$, O III]$\lambda\lambda1661, 1666$ (resolved) and [C III]$\lambda1907$+C III]$\lambda1909$ (blend; hereafter C III] $\lambda1908$) in emission. These features are not all well reproduced by the model, the luminosities of most emission lines in the best-fitting model appearing to be underestimated with respect to the observations (but see below). The posterior probability distribution of model parameters corresponding to the fit in Fig. 6.5 is shown in Fig. 6.6. For reference, the 16–84% credible interval of this distribution suggests a stellar population age $7.8 \leqslant \log(t_{\mathrm{star}}/\mathrm{yr}) \leqslant 8.8$, stellar mass $7.0 \leqslant \log(M/\,\mathrm{M}_\odot) \leqslant 7.8$, metallicity $-2.2 \leqslant \log(Z/Z_\odot) \leqslant -1.8$, gas ionization parameter $-3.5 \leqslant \log U_{\mathrm{S}} \leqslant -2.3$, dust attenuation optical depth $-3 \leqslant \log \hat{\tau}_V \leqslant -2$ and velocity

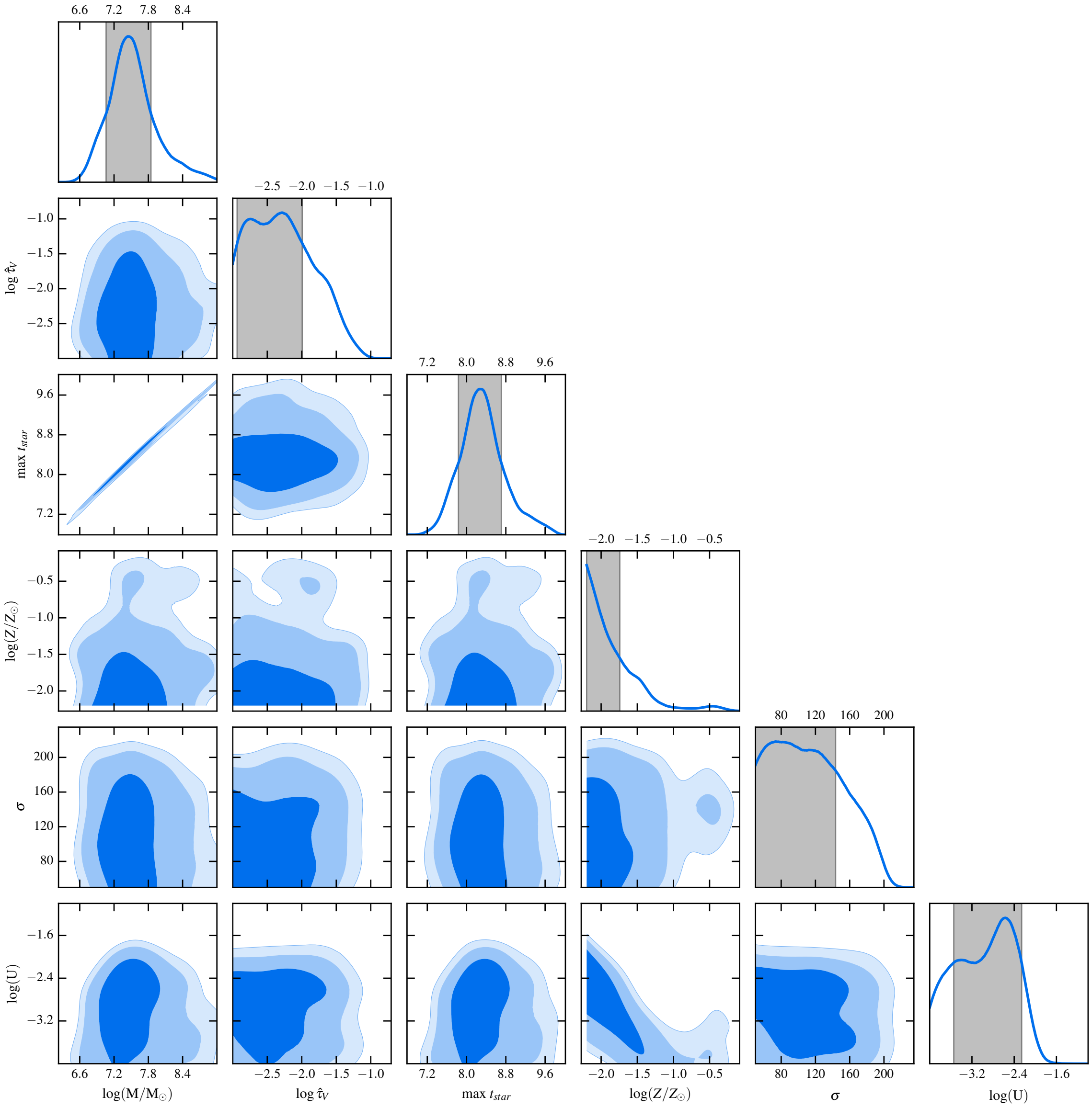

Figure 6.6 – Posterior probability distribution of the fitted parameters for the SBS-0335-052 galaxy. The diagonal panels show the marginal distributions of M, $\hat{\tau}_V$, t_{star}, Z, σ and U_{S} and the off-diagonal panels the joint distribution of every pair of these parameters.

dispersion $50 \leqslant \sigma(\mathrm{km\,s^{-1}}) \leqslant 145$.

To investigate the origin of the poor model match to the observations in Fig. 6.5, we plot in Fig. 6.7 the ratio of the observed C III] λ1908 and He II λ1640 luminosities against the ratio of the observed C IV λ1550 and C III] λ1908 luminosities for SBS-0335-052 (black filled circle). Also shown for reference are the nebular emission models of star-forming galaxies incorporated in BEAGLE (from Gutkin et al., 2016, stars connected with dotted lines) and nebular emission models of narrow-line regions of AGN (from Feltre et al., 2016, colored grids), for three different metallicities, $Z = 0.0005$, 0.001 and 0.017, along with low-metallicity shock models from Allen et al. (2008, in grey). According to Fig. 6.7, the emission-line ratios exhibited by SBS-0335-052 are characteristic of gas heated primarily by an AGN, with a possible contribution by shocks. The non-detection of highly ionized O VI λλ1032, 1038, which traces coronal gas shock-heated up to temperatures of $\sim 10^5 - 10^6$K (Grimes et al., 2009, see Section 1.4.2), suggests that nebular emission in this object is mainly driven by AGN activity. To further confirm this result, this preliminary study is being extended to include a comprehensive exploration of the parameter space of the models, especially exploring different C/O ratios (motivated by the presence of bright C emission lines) and star formation histories. Finally we are also working on fitting the *HST* observations of the other two galaxies in our program, where we also detect various absorption and emission lines, such as Si II $\lambda1526$, C IV $\lambda\lambda1548, 1551$ and Al II $\lambda1671$ (in absorption) and He II $\lambda1640$ and O III]$\lambda\lambda1661, 1666$ (in emission).

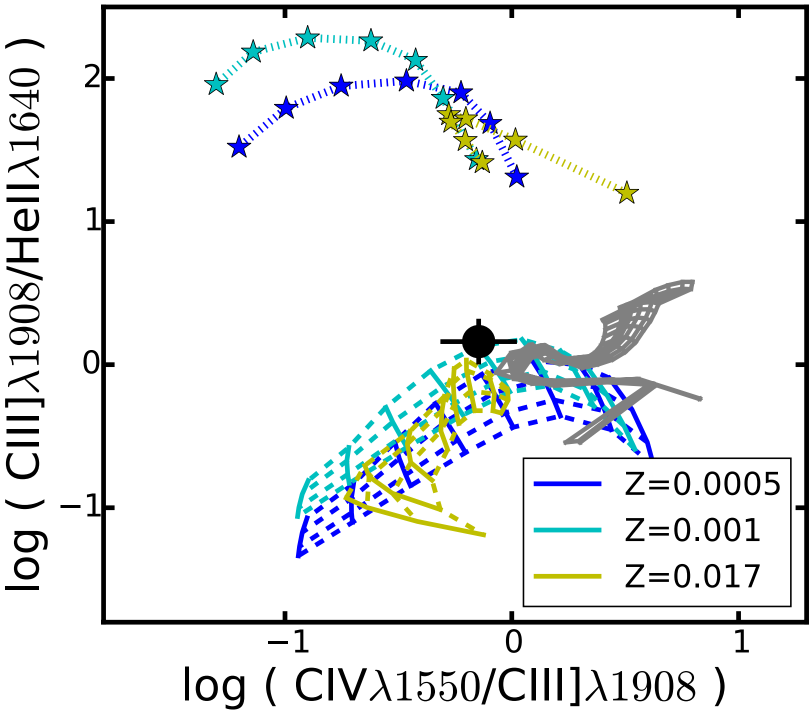

Figure 6.7 – C III] $\lambda1908$/He II $\lambda1640$ versus C IV $\lambda1550$/C III] $\lambda1908$ emission-line diagnostic diagram. The filled black circle indicates the position of SBS-0335-052. Also shown are nebular emission models of star-forming galaxies (from Gutkin et al., 2016, stars connected with dotted lines) and nebular emission models of narrow-line regions of AGN (from Feltre et al., 2016, colored grids), for three different metallicities, $Z = 0.0005$, 0.001 and 0.017 (color-coded as indicated) and ionizing parameters in the range $-4 \leq \log U_{\rm S} \leq -1$, along with low-metallicity shock models from Allen et al. (2008, in grey).

6.3 10 nearby galaxies with hard optical spectra

The following are some preliminary results obtained in the context of a successful proposal led by Dan Stark (Steward Observatory), in narrow collaboration with a few people from the NEOGAL team (S. Charlot, A. Feltre, A. Wofford and me), submitted for the *HST* Cycle 23 observations. The complete analysis will be presented in a paper currently in preparation. In this Section, as in the previous one, I summarize the science goals we want to achieve and the fitting techniques used to derive the first preliminary results, in which I am also actively involved.

The primary motivation for this project is again the preparation for *JWST* observations, which promise to revolutionize our understanding of the first generations of galaxies, by locating galaxies at $z \sim 10 - 15$ via emission-line spectroscopy. Meanwhile, as seen in Section 6.1, the first rest-frame-ultraviolet spectra of galaxies at $z \sim 7$ have revealed prominent nebular emission of C III] λ1908 and C IV λ1550 lines, in contrast to typical galaxy spectra at $z \sim 2 - 3$, pointing to an extreme radiation field in these reionization-era systems (Stark et al., 2015a; Stark et al., 2015b). As mentioned before, ultraviolet metal lines are of primary importance to characterize the properties of galaxies at the highest redshifts ($z > 10$), for which strong rest-optical lines will be shifted out of the spectral window probed by *JWST*/NIRSpec, because aside from a few examples corresponding to extreme conditions (Section 6.1), Lyα is likely not to be detected in the spectra of these galaxies.

To extract useful information from observed ultraviolet spectra, we must understand what physical conditions and stellar populations can produce such high ionization species as C III and C IV. Unfortunately we are not fully prepared yet to interpret these features, mainly because we lack ultraviolet templates of nearby star-forming systems with very hard ionizing spectra. To remedy this issue, we proposed to obtain *HST*/COS ultraviolet spectra of 10 nearby star-forming galaxies known to have hard ionizing spectra from optical spectroscopy (see below), with the goal of characterizing the strength of four diagnostic ultraviolet lines (C IV λ1550, He II λ1640, O III] λ1663 and C III] λ1908). We expect these data to provide new insight into the nature of massive stars that power high-ionization emission lines, demonstrating whether nearby star-forming systems ever produce ultraviolet equivalent widths as large as are now being observed at high redshift. The spectra will allow one to test and calibrate the ultraviolet spectral models that will be mostly used by the community in the *JWST* era.

Recently, Shirazi & Brinchmann (2012) constructed a sample of local star-forming galaxies with hard ionizing continua capable of powering C IV and He II emission. They searched in the SDSS DR7 database for emission-line galaxies and identified systems with nebular He II λ4686 emission. After removing AGNs, they were left with 189 star-forming galaxies, in the more metal-rich of which Wolf-Rayet stars are expected to play a dominant role in powering the He II emission. Among the more metal-poor He II λ4686 emitters ($12 + \log \mathrm{O/H} < 8.2$), Wolf-Rayet features become increasingly absent in the optical spectra. It is these low-metallicity nebular He II λ4686 emitters that provide the ideal sample for comparison to the strong nebular emitters now being discovered at high redshift. Given that this sample lacks spectral observations in the ultraviolet, we proposed to use the *HST*/COS medium-resolution gratings G160M and G185M to characterize the ultraviolet spectra of ten carefully-chosen star-forming galaxies with He II λ4686 detections in their optical spectra and moderately metal-poor gas ($12 + \log \mathrm{O/H} = 7.7 - 8.2$). This choice is motivated by the fact that the galaxies at $z \sim 2$ with prominent ultraviolet nebular lines tend to have low metallicity. We expect the same to be true at $z > 6$. Secondly, in order to assess the impact of different massive stellar populations on the ultraviolet spectral properties, we included objects with and without Wolf-Rayet spectral features. We expect the presence of Wolf-Rayet stars to impact the stellar He II line and the presence/absence of O stars to impact the C IV P-Cygni profile.

To summarize, with these observations, we want to accomplish the following four goals: (i) determine if stars can power strong C IV and He II ultraviolet nebular lines; (ii) characterize the nature of the stars that power high-ionization emission lines; (iii) anchor stellar population synthesis prescriptions; and (iv) prepare for *JWST*, as the 4 ultraviolet lines cited above will be the primary way we study galaxies at $z > 10-11$ with *JWST*.

We have started to fit the spectra of the ten galaxies in this sample using the same version of the BEAGLE tool as used in Sections 6.1 and 6.2. The models considered here have the same hydrogen density and C/O (and N/O) abundance ratios as those in Section 6.1. As in the previous sections, we also account by dust attenuation using the 2-component model of Charlot & Fall (2000), combined with the Chevallard et al. (2013) 'quasi-universal' prescription to account for the effects linked to dust/star geometry (including ISM clumpiness) and galaxy inclination.

We parametrize the star formation histories of model galaxies in BEAGLE as exponentially delayed functions (see Sections 2.3 and 5.2), for star formation timescales in the range $7 \leqslant \log(\tau_{\mathrm{SFR}}/\mathrm{yr}) \leqslant 10.5$. We adopt a standard Chabrier (2003) initial mass function and assume that all stars in a given galaxy have the same metallicity, in the range $-2.2 \leqslant \log(Z/Z_{\odot}) \leqslant 0.25$. We superpose on this smooth exponential function a current burst with a fixed duration of 10 Myr, whose strength is parametrized in terms of the specific star formation rate, in the range $-14 \leqslant \log(\psi_{\mathrm{S}}/\mathrm{yr}^{-1}) \leqslant -7$. We adopt the same metallicity for the gas as for the stars ($Z_{\mathrm{gas}} = Z$) and let the dust-to-metal mass ratio and ionization parameter freely vary in the ranges $0.1 \leqslant \xi_{\mathrm{d}} \leqslant 0.5$ and $-4 \leqslant \log U_{\mathrm{S}} \leqslant -1$. We consider V-band dust attenuation optical depths in the range $-3 \leqslant \log \hat{\tau}_V \leqslant 0.7$ and fix the fraction of this arising from dust in the diffuse ISM rather than in giant molecular clouds at $\mu = 0.4$ (Wild et al., 2011).

With this parametrization, we use BEAGLE to fit the observed emission-line luminosities of the galaxies in our sample, combining the new *HST* observations with existing ones. The lines we consider are C IV $\lambda1548$, C IV $\lambda1550$, He II $\lambda1640$, O III] $\lambda1661$, O III] $\lambda1666$, [C III] $\lambda1907$, C III] $\lambda1909$, [O II] $\lambda3727$, [Ne III] $\lambda3868$, Hδ, Hγ, [O III] $\lambda4363$, Hβ, [O III] $\lambda4959$, [O III] $\lambda5007$, [N II] $\lambda6548$, Hα, [N II] $\lambda6583$, [S II] $\lambda6716$ and [S II] $\lambda6730$. We exclude from the fitting three observed lines ([Ne III] $\lambda3970$, [O II] $\lambda\lambda7320, 7330$) not included in the nebular models. Fig. 6.8 illustrates the result of fitting simultaneously the luminosities of all available ultraviolet and optical and ultraviolet lines for the 10 galaxies in the sample. For each galaxy, we find that the best-fitting model can reproduce successfully the luminosities of most observed lines. The models best matching observations generally have high specific star formation rates, $-7.6 \lesssim \log(\psi_{\mathrm{S}}/\mathrm{yr}^{-1}) \lesssim -7.2$, and metallicities in the range $0.0022 \lesssim Z \lesssim 0.0052$, i.e. corresponding to 0.14–0.34 $Z_{\odot}$ when using the present-day solar metallicity value $Z_{\odot} = 0.01524$ (Bressan et al., 2012). The galaxies are also found to have small stellar masses, between roughly 3×10^5 and 4×10^7 $\mathrm{M}_{\odot}$, fairly high ionization parameters, $-2.70 \lesssim \log U_{\mathrm{S}} \lesssim -1.89$ and lowish dust-to-metal mass ratios, $0.10 \lesssim \xi_{\mathrm{d}} \lesssim 0.37$. As in Section 6.1, the detection of carbon emission lines allows us to compare the performances of models with different C/O ratios, although our preliminary analysis reveals no strong difference in the fits obtained using models with solar and half-solar C/O, for example. Finally, the models suggest large Lyman-continuum photon production efficiencies, $26.5 \lesssim \log(\xi_{\mathrm{ion}}/\mathrm{erg}^{-1}\mathrm{Hz}) \lesssim 28.2$, indicating that these galaxies have intense radiation fields, as expected from the detection of He II $\lambda4686$ in the optical spectra. We are also experimenting with the characterization of galaxy properties using different combinations of emission lines, for example by considering only optical lines, or only ultraviolet ones.

As a complement to Fig. 6.8, Fig. 6.9 shows the posterior probability distribution of model parameters obtained from the emission-line fitting of one of the galaxies in the sample. While

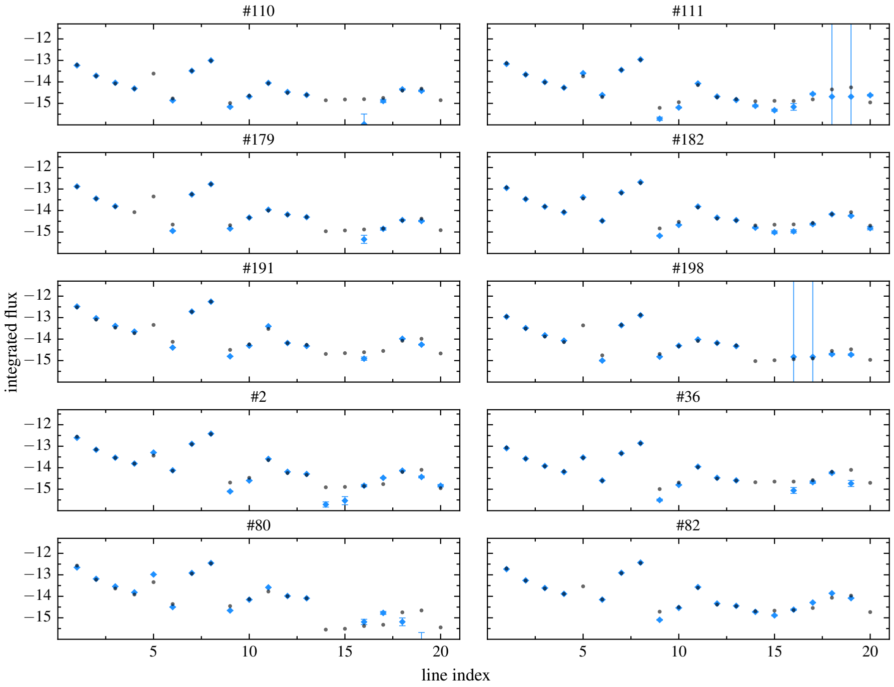

Figure 6.8 – BEAGLE fits of the ultraviolet and optical emission-line luminosities in the spectra of the 10 local galaxies in the sample described in Section 6.3. In each panel, the integrated lines fluxes of the best-fitting model (in black) are compared to the observed ones (in blue). On the abscissa, the lines are coded as follows: 1: Hα, 2: Hβ, 3: Hγ, 4: Hδ, 5: [O II] λ3727, 6: [O III] λ4363, 7: [O III] λ4959, 8: [O III] λ5007, 9: [N II] λ6548, 10: [N II] λ6583, 11: [Ne III] λ3868, 12: [S II] λ6716 and 13: [S II] λ6730, 14: C IV λ1548, 15: C IV λ1550, 16: O III] λ1661, 17: O III] λ1666, 18: [C III] λ1907, 19: C III] λ1909 and 20: He II λ1640.

most of the parameters appear to be already well constrained using emission lines alone, we are also interested in characterizing the properties of the stars responsible for the extreme radiation fields. To this end, I am now extending these fits to include information about the stellar continuum and absorption-line strengths. The results of this new fitting procedure will allow us to better characterize the stellar content of the galaxies.

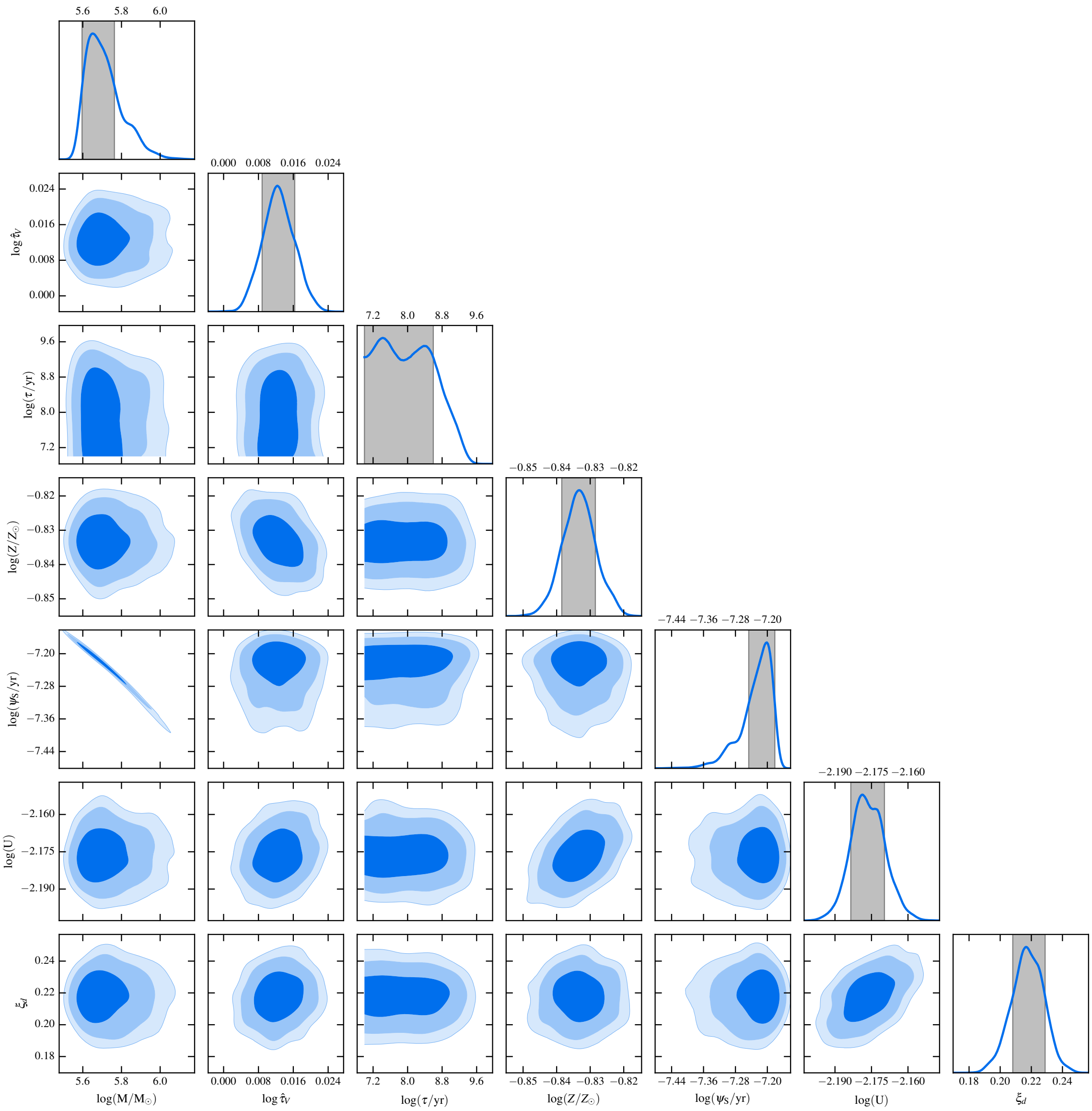

Figure 6.9 – Posterior probability distribution of the fitted parameters for the galaxy SBID 2 in the sample described in Section 6.3. The diagonal panels show the marginal distributions of M, $\hat{\tau}_V$, $\tau_{\rm SFR}$, Z, $\psi_{\rm S}$, $U_{\rm S}$ and ξ_d, and the off-diagonal panels the joint distribution of every pair of these parameters.

Chapter 7

Conclusions and perspectives

In this thesis, I have used a combination of state-of-the-art models for the production of stellar radiation and its transfer through the ISM to investigate ultraviolet-line diagnostics of stars, the ionized and the neutral ISM in star-forming galaxies. I started by assessing the ability for the latest version of the Bruzual & Charlot (2003, see also Wofford et al. 2016) stellar population synthesis code to reproduce pure stellar absorption features in the ultraviolet spectra of ISM-free star clusters in the LMC, from the sample of Cassatella et al. (1987). The fact that these clusters have small stellar masses, between about 3×10^3 and 7×10^4 $\mathrm{M}_{\odot}$, forces one to consider the effects of stochastic IMF sampling on their integrated spectral properties (e.g., Fouesneau et al., 2012). I find that the stellar population models provide reasonable fits to the observed strengths of 17 ultraviolet indices defined by Fanelli et al. (1992) in the spectra of these clusters. In the corresponding age range, between 10 Myr and 100 Myr, the neglect of stochastic variations in the number of massive stars hosted by individual star clusters does not have a strong influence on ultraviolet-based age and metallicity estimates. However, neglecting this effect can lead to systematic overestimates of stellar-mass, up to a factor of ∼3 for the cluster sample considered here.

Based on this success in reproducing stellar absorption features in ultraviolet spectra of young stellar populations, I have developed a new approach to model the combined influence of nebular emission and interstellar absorption on the ultraviolet spectra of star-forming galaxies. This approach builds on an idealized description of the main features of the ISM, inspired from the dust model of Charlot & Fall (2000). This accounts for the ionization of H II regions in the interiors of the dense clouds in which stars form and the dissipation of these clouds on a timescale of typically 10 Myr (e.g. Murray et al., 2010; Murray, 2011). Photons emerging from stellar birth clouds and those produced by longer-lived stars must transfer through the intercloud medium on their way out of the galaxy. The combination of state-of-the-art stellar population synthesis and photoionization codes in this framework has already proven valuable to model and interpret the ultraviolet and optical nebular emission from star-forming galaxies (Charlot & Longhetti 2001, hereafter CL01; see also Gutkin et al. 2016 and references therein). Here, we have expanded on these calculations to incorporate line absorption in the ionized and neutral ISM of a star-forming galaxy, by appealing to the spectrum synthesis code SYNSPEC (e.g., Hubeny & Lanz, 2011). This can be invoked via the program CLOUDSPEC (Hubeny et al., 2000, see also Heap et al. 2001) to compute strengths of interstellar absorption lines based on the ionization structure solved by CLOUDY.

The main physical parameters of the ISM that need to be specified to compute absorption-line strengths in this context are the gas density, ionization parameter (linked to the stellar ionizing radiation), metal abundances and depletion on to dust grains. A simple parametrization of the birth clouds in terms of these physical quantities has been proposed by CL01. This was recently improved by Gutkin et al. (2016) to incorporate a versatile, fully consistent treatment of metals and dust allowing one to relate nebular emission to both gas-phase and dust-phase metal enrichment, over a wide range of chemical compositions. I adopt this parametrization to compute simultaneously nebular emission and interstellar-line absorption in the ionized interiors and outer H I envelopes of birth clouds using CLOUDSPEC. Since the birth clouds in this idealized approach are assumed to be ionization bounded, the parameters above should be regarded as 'effective' ones describing the global physical conditions of the dense gas surrounding young stars throughout the galaxy (see CL01). In the model, we also account for interstellar-line absorption in the diffuse, intercloud medium. This is achieved by relating the 1500-Å energy density of the interstellar radiation field to the star formation rate and by specifying the typical H I column density seen by photons in the intercloud medium.

I have used this approach to explore, in a physically consistent way, the competing effects of stellar absorption, nebular emission and interstellar absorption in ultraviolet spectra of star-forming galaxies. To this end, I have studied in detail the model spectra of a young, metal-poor galaxy and a more mature, metal-rich galaxy to identify the cleanest ultraviolet tracers of young stars, nebular emission and interstellar absorption. I find that most standard ultraviolet indices defined in the spectra of ISM-free stellar populations (e.g., Fanelli et al., 1992; Leitherer et al., 2001; Rix et al., 2004; Sommariva et al., 2012) can potentially suffer from significant contamination by the ISM, which increases with metallicity. Two notable exceptions are spectral regions around 1425 and 1719 Å, for which contamination remains weak even at high metallicity. For the other indices, the potential influence of the ISM should be kept in mind when constraining young-star properties from observed spectra. I also identify 11 nebular-emission features, between O III]$\lambda\lambda$1661, 1666 and He I λ3188, and 10 interstellar-absorption feature, between O I λ1302 and the Fe II λ2612–λ2632 blend, which stand out as clean tracers of the different phases of the ISM (Table 4.2). Finally, I illustrate how this model allows one to explore the complex dependence of prominent, widely studied features, such as O V λ1371, Si IV λ1400, C IV λ1550, He II λ1640 and N IV λ1719, on stellar and ISM properties.

The results presented in this work are only examples of the potential of our approach to investigate in a physically consistent way the entangled signatures of stars, the ionized and the neutral ISM in ultraviolet spectra of star-forming galaxies. The ability to conduct such investigations opens the door to quantitative studies of the influence of the different adjustable model parameters, designed to capture the main features of stellar populations and the ISM, on emission- and absorption-line strengths. Also, while we have considered only static interstellar media in this work, the model allows the exploration of kinematic signatures of gas infall and outflows on the profiles of lines with different ionization potentials tracing different phases of the ISM. Studies of this kind are the key to better understand the interplay between gas infall, star formation, metal and dust production and enrichment of the circumgalactic medium from ultraviolet spectroscopy of star-forming galaxies.

An example of the modeling capabilities of such kinematic signatures is shown in Fig. 7.1, where I illustrate the signatures of four different velocity fields in the absorption-line profiles of both weakly- and highly-ionized species, C II λ1335, Si IV $\lambda\lambda$1394, 1403, Si II λ1526, Si II* λ1533 and C IV $\lambda\lambda$1548, 1551, for the same young galaxy model as in Fig. 4.1a: (i) in black, I draw as a reference the static ISM model (corresponding to the red spectrum in Fig. 4.1a); (ii) in blue, a model in which I have applied a constant velocity field of 400 km s^{-1}; (iii) in green, one in which I let the velocity vary linearly from 70 km s^{-1} in the inner part of the cloud to 680 km s^{-1} at the outer edge of the cloud (corresponding roughly to the values inferred by Steidel et al. 2010 from observations of distant Lyman-break galaxies; see next); and (iv) in magenta, one in which I adopt the empirical radial dependence of velocity proposed by Steidel et al. (2010, see their fig. 24 and explanations therein) to reproduce observations of outflows in the stacked spectrum of a sample of Lyman-break galaxies at redshifts $z \sim 2-3$. Compared to the models with static and constant-velocity fields, those with a linear and empirical radial dependence of velocity show bluer-shifted absorption lines and also wider profiles. The ability to model such kinematic signatures of galactic outflows in the profiles of lines produced in different regions of the ISM represents a valuable means of interpreting observations of distant galaxies.

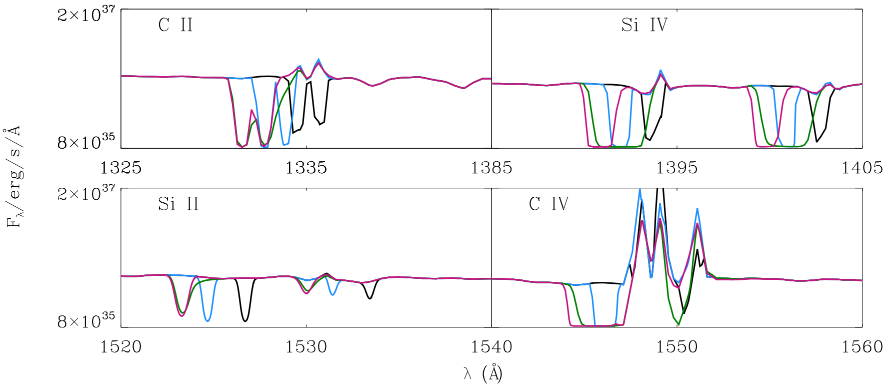

Figure 7.1 – Signatures of four different velocity fields in the absorption-line profiles of the weakly and highly ionized lines C II $\lambda1335$, Si IV $\lambda\lambda1394, 1403$, Si II $\lambda1526$, Si II* $\lambda1533$ and C IV $\lambda\lambda1548, 1551$, for the same young galaxy model as in Fig. 4.1a: (i) in black, reference static-ISM model (corresponding to the red spectrum in Fig. 4.1a); (ii) in blue, constant velocity field of 400 km s^{-1}; (iii) in green, velocity varying linearly from 70 km s^{-1} in the inner part of the cloud to 680 km s^{-1} at the outer edge of the cloud; and (iv) in magenta, empirical radial dependence of velocity proposed by Steidel et al. (2010, see their fig. 24 and explanations therein) to reproduce observations of outflows in the stacked spectrum of a sample of Lyman-break galaxies at redshifts $z \sim 2-3$.

Finally, I have also presented some preliminary results of the constraints I derive fitting ultraviolet and optical spectra of star-forming galaxies at various redshifts observed with the *Hubble Space Telescope* and the Keck I telescope. To fit these spectral signatures, I make use of the novel statistical-inference tool BEAGLE, whose current version allows one to model the emission from stellar populations, the emission from gas ionized by young stars and absorption by dust in the interstellar medium and by (Lyα-forest) gas in the intergalactic medium, each effect being incorporated via a different code module. Fitting different combinations of spectroscopic and photometric observations, such as broadband magnitudes, emission-line luminosities or equivalent widths or the full (pixel-by-pixel) stellar+nebular-emission spectrum, allows one to draw statistical constraints on galaxy physical parameters, such as stellar mass, star formation history, metallicity, and several ionized-gas parameters. The first release of BEAGLE has proven valuable to interpret observed spectral energy distributions of galaxies and the emission from gas photoionized by young stars. In a future release, the inclusion of a module describing the signatures of photoionization by an AGN (based on the models of Feltre et al., 2016) will allow one to better interpret spectra of galaxies with nuclear activity, such as presumably SBS-0335-052.

Beyond simply using the BEAGLE code, I am also leading the development of a new module incorporating the models of interstellar absorption presented in Chapter 4. This module will allow one to model and interpret various physical properties of the absorbing gas, such as kinematics and abundances. With this module, the user will be able to derive physically consistent constraints on the properties of stars, emitting and absorbing gas by fitting all the pixels in an observed galaxy spectrum.

Appendices

Appendix A

Ultraviolet stellar absorption-line indices

I summarize here the information collected from various sources (Fanelli et al., 1992; Chavez et al., 2007; Maraston et al., 2009; Leitherer et al., 2011) about the 19 ultraviolet-line indices defined by Fanelli et al. (1992) in the *IUE* spectra of 218 solar-neighbourhood stars, which I use to calibrate the models from the stellar emission. We refer the reader to Table 3.1 for an indication of the atomic species thought to contribute mainly to these absorption features, according to the same sources.

- Bl 1302: Because it is prominent in B2-B9 stars and weak in O stars, its presence in a spectrum indicates a substantial B star component in hot populations. It does not depend on the luminosity class. A smooth rise with increasing color is also observed.

- Si IV 1397: This index is prominent in early B stars, and reaches its maximum at type B1. It shows a stronger gravity dependence than Bl 1302 because supergiants show the strongest Si IV features, although some of them have the same values as dwarfs. Therefore, a strong Si IV line may indicate a substantial blue supergiant component and can serve as a diagnostic for OB supergiants and late-O to early-B dwarfs. In early supergiants, this line shows a P Cygni profile.

- Bl 1425: This index is present from types O8 to B2 in dwarfs, and until type B5 in supergiants, peaking at type B0. It is not very sensitive to temperature.

- Fe 1453: Originally thought as a blend of Fe lines. A broad-line feature is present from types O2 trough B0. It also shows a strong positive temperature dependence.

- C IV^{a}: This feature displays a P Cygni profile in supergiants earlier than B0 and in dwarfs of types O3-6. The index is defined to sample the blue absorption of the P-Cygni profile. It is prominent in O and early B stars. A strong C IV line would indicate early main-sequence stars or a substantial supergiant population. It shows a well defined temperature dependence. It can be detected at low resolution together with Si IV and can serve to distinguish the presence of starbursts at high-z.

- C IV^{c}: This index is centered in the P Cygni profile, therefore it will include both the absorption and the emission component of the line.

- C IV^{e}: This index is centered to just include the emission part of the the P-Cygni profile. It is only important in the earliest spectral types (early O) whereas a strong absorption would indicate the presence of late-O to early-B stars. The P-Cygni wind feature disappears in the dwarfs at a bluer color than in the supergiants.

- Bl 1617: This is a wide feature present in O to early B supergiants and from O7 trough B0 in dwarfs, but it is stronger in supergiants.

- Bl 1664: This index increases monotonously from spectral types around B5 up to early A stars. Stars of later types than B8 show Al II 1671 in absorption.

- Bl 1719: This index may be present in early O dwarfs and supergiants to B1. This index is not sensitive to temperature and shows a mild surface gravity dependence. Supergiants can exhibit as much as double strength values than dwarfs.

- Bl 1853: This index increases in strength from B2 to mid A types. Its presence in a composite spectrum of a population of star suggests the existence of stars of spectral types B5-F5. It has a similar behavior to Bl 1664 but it shows a better surface gravity separation.

- Fe II 2402: The strength of this index is close to zero until late B spectral types, and it increases toward earlier types, peaking around late F and early G. It displays a similar luminosity-class separation than Bl 2538, being very sensitive to gravity (see below).

- Bl 2538: This index has the highest sensitivity to luminosity class among mid-ultraviolet indices. At the peak, dwarfs have equivalent widths that nearly double those of supergiants. It increases for stars cooler than early A-type, reaching its maximum at late F stars.

- Fe II 2609: This index is dominant for A-F stars. Its qualitative behavior is similar as Fe II 2402.

- Mg II 2800: This is an absorption feature in A to G stars (photospheric absorption), but it becomes an emission feature near K2 (chromospheric emission). It rises linearly from A0 to F8-G1 but it displays a wide range of values at the same type for later spectral types. It is an excellent temperature index for blue stars but shows a slight dependence on gravity.

- Mg I 2852: This index is important for late F through K types. It shows a tighter temperature dependence than Mg II and reaches the maximum strength at K0. Unlike Mg II, it does not show a strong reversal in cool stars and an emission feature is observed only in M supergiants. It also shows a similar qualitative behavior as Fe II 2402 and an enhanced sensitivity to gravity with respect to Mg II.

- Mg wide: This is a composite of various Mg lines. The behavior of this index is qualitatively similar to that of Mg I. It appears to be a good indicator of the average temperature on a stellar population that does not have an appreciable contribution from the light of cool supergiants in the mid-ultraviolet (older than $\approx 10^{8}$ yr). Galaxies with any underlying hot component will suffer from dilution of the magnesium lines, while extremely ”cold” galaxies will have larger indices. It is very sensitive to gravity, lowest gravity ones being the strongest.

- Fe I 3000: This is a wide feature with at least four strong lines observed on G and K stars. Analogous to Mg I, supergiants display weaker values up to mid-K stars. It has a similar qualitative behavior as Fe II 2402 and a similar luminosity-class separation than Bl 2538.

- Bl 3096: This is an important feature for G and K stars, making it an unambiguous marker of stars cooler than F7. It shows the best luminosity segregator of mid-ultraviolet. Supergiants show bigger strengths than dwarfs, though supergiants and giants are not separated among themselves. It also shows a monotonic increase with decreasing temperature.

Appendix B

Correction of ultraviolet index strengths for Galactic absorption

Resonant transitions of different species in the neutral and ionized ISM of the Milky Way produce discrete absorption features in the ultraviolet spectra of the LMC clusters observed by Cassatella et al. (1987). We must correct for these features before fitting the spectra with pure stellar population synthesis models. Savage et al. (2000) measure the absorption equivalent widths of ionized species from the Milky-Way ISM in the ultraviolet spectra of background quasars along 83 different lines of sight observed with the Faint Object Spectrograph on board *HST*. They find that weakly ionized species, such as Si II or C II, are in general stronger (with equivalent widths of up to ~ 0.8Å) than highly ionized species, such as Si IV or C IV (with equivalent widths of up to ~ 0.4Å). Leitherer et al. (2011, see their table 3) compute the median equivalent widths of the 24 strongest absorption lines in this sample (the values listed by these authors in units of km s^{-1} can be converted into Å by dividing by the line frequency). Here, we use these data to correct, a posteriori, the equivalent widths of the 19 Fanelli et al. (1992) indices defined in Table 3.1 measured by Maraston et al. (2009) in the *IUE* spectra of Cassatella et al. (1987). We find that 15 of the 24 strong ISM lines can affect the central and continuum bandpasses of 14 indices. For two indices, Bl 2538 and Fe II 2609, Milky-way lines contaminate both the central and a continuum bandpasses. If a Milky-Way line falls in a central index bandpass, we correct the index equivalent width as

$$\mathrm{EW}^{\mathrm{corr}}_{\mathrm{cluster}} = \mathrm{EW}^{\mathrm{M09}}_{\mathrm{cluster}} - \mathrm{EW}_{\mathrm{MW}}\,, \tag{B.1}$$

where $\mathrm{EW}_{\mathrm{MW}}$ is the equivalent width of the Milky-Way line(s) affecting the central bandpass and $\mathrm{EW}^{\mathrm{M09}}_{\mathrm{cluster}}$ is the index equivalent width measured by Maraston et al. (2009). The term $\Delta(\mathrm{EW}/\text{Å})$ listed in Table 3.1 is in this case simply $-\mathrm{EW}_{\mathrm{MW}}$. We compute the error in $\mathrm{EW}^{\mathrm{corr}}_{\mathrm{cluster}}$ by propagating those in $\mathrm{EW}^{\mathrm{M09}}_{\mathrm{cluster}}$ (Maraston et al., 2009) and $\mathrm{EW}_{\mathrm{MW}}$ (Leitherer et al., 2011). The indices to which we have applied this correction are Bl 1302, Si IV 1397, C IV$^{\mathrm{a}}$, C IV$^{\mathrm{c}}$, C IV$^{\mathrm{a}}$, Bl 1664, Bl 1853, Fe II 2402, Fe II 2609, Mg II 2800, Mg I 2852 and Mg wide.

When a Milky-Way absorption line falls in a pseudo-continuum bandpass, we estimate a mean correction to that index strength for all clusters in the sample as follows. We consider a unit spectrum, in which we carve, in the central index bandpass, an absorption line (with Gaussian profile and unit standard deviation) of equivalent width the median value measured by Maraston et al. (2009) in the Cassatella et al. (1987) cluster spectra. Then, we recompute the index strength after carving the Milky-Way absorption line(s) (with Gaussian profile and unit standard deviation) in the continuum bandpass. The $\Delta(\mathrm{EW}/\text{Å})$ listed in Table 3.1 in this

Table B.1 – Equivalent widths of the 19 Fanelli et al. (1992) indices defined in Table 3.1 in the spectra of the 10 LMC clusters observed by Cassatella et al. (1987), along with the associated measurement errors (both quantities in Å), after correction for contamination by strong Milky-Way absorption lines.

Index	NGC 1711	NGC 1805	NGC 1818	NGC 1847	NGC 1850	NGC 1866	NGC 1984	NGC 2004	NGC 2011	NGC 2100
Bl 1302	3.23 ± 0.49	4.23 ± 0.66	2.93 ± 0.94	3.63 ± 0.66	3.53 ± 0.57	3.23 ± 0.76	3.03 ± 1.04	3.33 ± 0.41	3.03 ± 0.85	3.03 ± 0.49
Si IV 1397	1.33 ± 0.54	2.03 ± 0.73	1.13 ± 0.82	2.33 ± 0.63	0.33 ± 0.63	−0.16 ± 0.73	3.73 ± 0.92	3.23 ± 0.44	3.03 ± 0.73	2.93 ± 0.44
Bl 1425	−0.30 ± 0.50	1.20 ± 1.70	0.40 ± 0.80	0.90 ± 0.70	−0.30 ± 0.60	−0.10 ± 0.70	1.60 ± 1.00	0.60 ± 0.40	0.90 ± 0.70	0.30 ± 0.50
Fe 1453	−0.90 ± 0.70	−0.50 ± 1.10	−1.70 ± 1.10	−0.70 ± 1.00	−2.10 ± 1.00	−2.30 ± 1.20	1.00 ± 1.50	−1.00 ± 0.60	−0.60 ± 1.10	−0.90 ± 0.70
C IV[a]	1.09 ± 0.52	1.39 ± 0.81	0.79 ± 0.91	0.99 ± 0.71	1.29 ± 0.61	−0.01 ± 0.61	1.69 ± 1.11	2.49 ± 0.42	3.69 ± 0.61	1.39 ± 0.52
C IV[c]	0.95 ± 0.43	1.05 ± 0.72	0.75 ± 0.72	1.85 ± 0.62	0.75 ± 0.62	−0.15 ± 0.53	1.75 ± 1.01	2.15 ± 1.51	3.45 ± 0.62	1.45 ± 0.53
C IV[e]	0.67 ± 0.51	0.90 ± 0.80	1.37 ± 0.71	1.37 ± 0.71	1.67 ± 0.61	0.57 ± 0.61	0.97 ± 1.10	0.17 ± 0.41	2.47 ± 0.61	1.47 ± 0.41
Bl 1617	0.80 ± 0.60	−0.70 ± 1.10	0.90 ± 1.10	0.90 ± 0.90	1.20 ± 0.70	1.20 ± 0.70	1.80 ± 1.50	0.90 ± 0.50	1.80 ± 0.80	1.70 ± 0.50
Bl 1664	0.96 ± 0.52	−0.94 ± 0.82	0.26 ± 1.21	0.16 ± 0.82	0.46 ± 0.62	1.16 ± 0.62	−0.14 ± 1.51	−0.54 ± 0.62	0.46 ± 0.82	1.16 ± 0.53
Bl 1719	1.46 ± 0.40	1.26 ± 0.60	1.56 ± 1.00	1.06 ± 0.60	1.56 ± 0.40	1.86 ± 0.40	1.56 ± 1.30	1.96 ± 0.40	1.86 ± 0.60	1.86 ± 0.50
Bl 1853	0.89 ± 0.44	0.89 ± 0.53	1.09 ± 1.02	1.89 ± 0.63	1.69 ± 0.35	1.79 ± 0.63	1.39 ± 1.61	1.29 ± 0.63	0.99 ± 0.92	1.29 ± 0.63
Fe II 2402	1.33 ± 1.52	3.03 ± 2.01	0.63 ± 1.32	0.73 ± 1.72	−0.17 ± 1.82	1.53 ± 1.62	2.83 ± 1.52	−0.07 ± 0.83	2.03 ± 0.74	1.23 ± 1.91
Bl 2538	−0.65 ± 1.41	0.85 ± 1.71	−0.15 ± 1.11	−0.75 ± 1.11	−2.15 ± 1.51	0.45 ± 1.41	−0.25 ± 1.11	−0.75 ± 0.82	1.45 ± 0.53	−1.95 ± 1.51
Fe II 2609	1.04 ± 0.94	1.44 ± 1.23	0.64 ± 0.75	0.84 ± 0.75	0.64 ± 0.94	1.44 ± 0.94	1.04 ± 0.66	0.74 ± 0.66	0.84 ± 0.41	0.34 ± 0.94
Mg II 2800	3.86 ± 0.89	3.26 ± 1.17	2.66 ± 0.72	2.46 ± 0.72	3.86 ± 0.99	4.86 ± 0.64	1.36 ± 0.64	3.96 ± 0.72	3.76 ± 0.72	4.66 ± 0.99
Mg I 2852	1.32 ± 0.91	0.52 ± 1.21	1.12 ± 0.72	0.92 ± 0.62	2.32 ± 0.91	1.92 ± 0.52	1.02 ± 0.42	1.52 ± 0.62	0.02 ± 0.71	1.92 ± 1.11
Mg wide	1.38 ± 6.81	4.98 ± 9.31	3.48 ± 5.52	0.88 ± 5.11	5.88 ± 7.11	9.28 ± 5.22	−4.82 ± 4.82	9.98 ± 4.22	1.68 ± 2.63	−2.42 ± 8.11
Fe I 3000	2.70 ± 2.20	3.20 ± 3.20	0.00 ± 1.50	−2.10 ± 1.90	0.10 ± 2.50	1.40 ± 1.40	1.00 ± 1.30	0.30 ± 1.30	−1.20 ± 1.20	1.10 ± 3.00
Bl 3096	−1.10 ± 1.30	−2.10 ± 2.20	0.10 ± 1.00	−1.30 ± 0.90	−1.40 ± 1.50	−0.80 ± 1.00	−0.30 ± 0.60	−0.70 ± 0.60	−0.40 ± 0.30	0.00 ± 1.40
V mag[a]	10.11 ± 0.03[b]	10.63 ± 0.03[b]	9.85 ± 0.02[b]	11.06 ± 0.02[c]	9.36 ± 0.06[b]	9.89 ± 0.01[b]	9.99 ± 0.04[d]	9.60 ± 0.02[c]	10.58 ± 0.02[c]	9.60 ± 0.04[b]
A_V mag[e]	0.56 ± 0.01	0.32 ± 0.02	0.39 ± 0.02	0.49 ± 0.02	0.33 ± 0.01	0.28 ± 0.06	0.36 ± 0.02	0.33 ± 0.02	0.47 ± 0.02	0.80 ± 0.02

[a] Apparent V-band magnitude not corrected for reddening. To transform to absolute magnitude, we adopt the extinction A_V listed in this table and a distance modulus to the LMC of 18.49±0.05 mag (i.e., a distance of 49.97±1.11 kpc; Pietrzyński et al., 2013).

[b] Apparent V-band magnitude and error from van den Bergh & Hagen (1968).

[c] Apparent V-band magnitude from Bernard & Bigay (1974) and error from Pessev et al. (2008).

[d] Apparent V-band magnitude and error from Pessev et al. (2008).

[e] V-band extinction from Pessev et al. (2008, and references therein).

case is the difference between the first and second estimates. We compute the error in $\mathrm{EW}^{\mathrm{corr}}_{\mathrm{cluster}}$ by repeating the process for Milky Way-line equivalent widths differing by $\pm\sigma_i$, where σ_i is the line-measurement error from Leitherer et al. (2011). The indices to which we have applied this correction are Bl 1719, Bl 1853, Bl 2538 and Fe II 2609. For the last two indices, Bl 2538 and Fe II 2609, the total correction is the sum of that affecting the central bandpass and that affecting the pseudo-continuum bandpass. The final corrected index strengths are presented in Table B.1 and the corrections terms listed in Table 3.1.

Appendix C

P-Cygni profiles

A P-Cygni profile is a characteristic spectral feature that can be detected in the spectra of stars with an ongoing strong wind. A schematic representation of the profile is drawn in the lower panel of Fig. C.1. This consists on an emission-line with a blue-shifted generally broad absorption component. The explanation for the shape of this feature is also illustrated in the top panel of Fig. C.1. In the figure we can see how the star is centered in the concentric expanding shell. This means that an observer will see a red-shifted part of the shell (that is expanding to the opposite sense) and a blue-shifted one (the part that is approaching the observer). The blue absorption is caused because due to its interaction with wind material, photospheric radiation is scattered out of the observer's line of sight. This absorption will be blue-shifted up to a frequency corresponding to the maximum velocity of the wind, known as the *terminal velocity*. The emission component is formed when the photons that have been previously absorbed are scattered into the observer's line of sight. This emission occurs in both hemispheres of the shell, corresponding to an almost symmetrical emission-line profile with respect to the center of the line. This lack of total symmetry arises because there is some material that would emit in the observer's direction that is hidden by the star (grey shaded area in the plot, the occulted region) with the consequence of the distortion of the symmetry induced by a weaker red-shifted emission. The combination of both components gives the final shape of the P-Cygni profile.

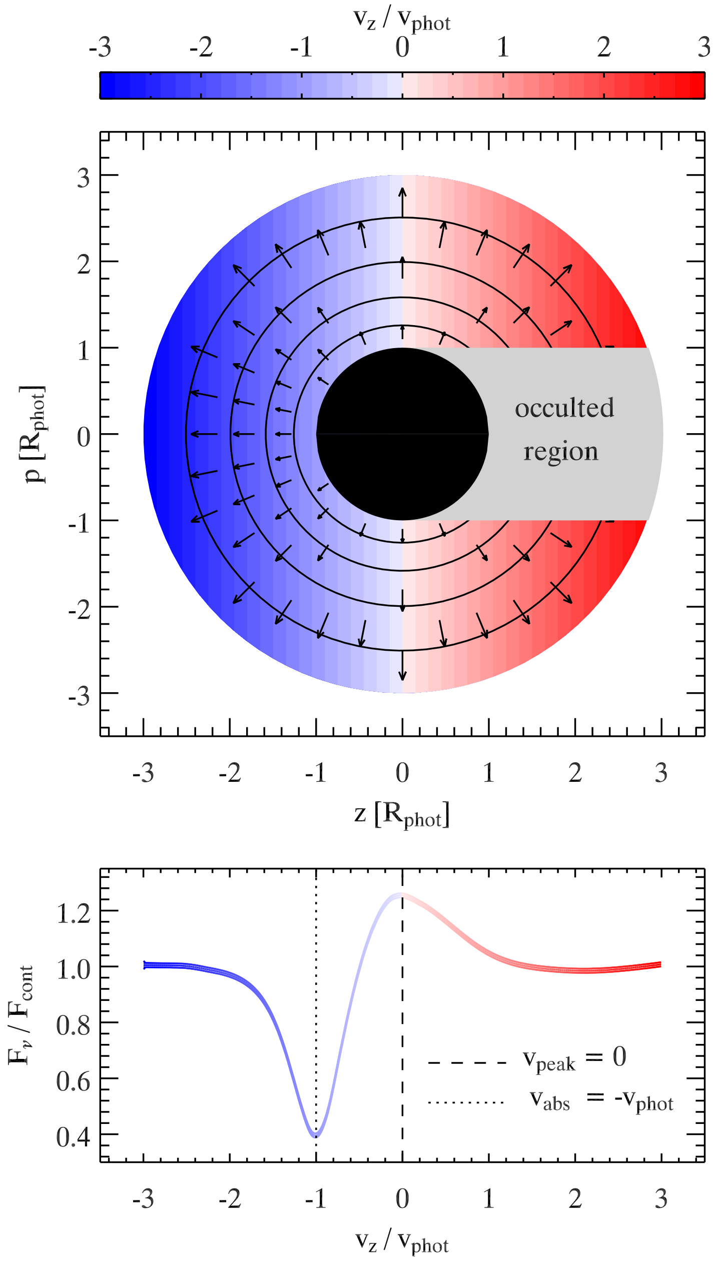

Figure C.1 – Top panel: Schematic representation of the formation of a P-Cygni profile. In the center the star that is losing its envelope is represented. Lower panel: A typical P-Cygni profile where the emission and blue-shifted broad absorption are shown. Credit: Stephane Blondin.

Bibliography

Allen M. G., Groves B. A., Dopita M. A., Sutherland R. S., Kewley L. J., 2008, The Astrophysical Journal Supplement Series, 178, 20 93, 94

Aloisi A., Savaglio S., Heckman T. M., Hoopes C. G., Leitherer C., Sembach K. R., 2003, The Astrophysical Journal, 595, 760 38

Arimoto N., Yoshii Y., 1987, Astronomy & Astrophysics, 173, 23 24

Baldry I. K., Glazebrook K., 2003, The Astrophysical Journal, 593, 258 29

Bastian N., Silva-Villa E., 2013, Monthly Notices of the Royal Astronomical Society, 431, L122 50

Bastian N., Covey K. R., Meyer M. R., 2010, Annual Review of Astron and Astrophys, 48, 339 30

Bernard A., Bigay J. H., 1974, Astronomy & Astrophysics, 33, 123 110

Bertone E., Buzzoni A., Chávez M., Rodríguez-Merino L. H., 2008, Astronomy & Astrophysics, 485, 823 31

Boggess A., et al., 1978, Nature, 275, 372 41

Bouwens R. J., et al., 2015, The Astrophysical Journal, 803, 34 86

Bressan A., Chiosi C., Fagotto F., 1994, The Astrophysical Journal Supplement Series, 94, 63 24

Bressan A., Marigo P., Girardi L., Salasnich B., Dal Cero C., Rubele S., Nanni A., 2012, Monthly Notices of the Royal Astronomical Society, 427, 127 29, 40, 46, 54, 61, 78, 90, 96

Bromm V., Yoshida N., 2011, Annual Review of Astronomy and Astrophysics, 49, 373 40

Bromm V., Coppi P. S., Larson R. B., 1999, The Astrophysical Journal Letters, 527, L5 9

Bruzual G., 2002, in Geisler D. P., Grebel E. K., Minniti D., eds, IAU Symposium Vol. 207, Extragalactic Star Clusters. p. 616 (`arXiv:astro-ph/0110245`) 30, 44

Bruzual G., Charlot S., 2003, Monthly Notices of the Royal Astronomical Society, 344, 1000 24, 25, 30, 35, 39, 40, 44, 49, 58, 99

Bruzual A. G., 1983, The Astrophysical Journal, 273, 105 24

Buzzoni A., 1989, The Astrophysical Journal Supplement Series, 71, 817 24

Caffau E., Ludwig H.-G., Steffen M., Freytag B., Bonifacio P., 2011, Solar Physics, 268, 255 61

Cassatella A., Barbero J., Geyer E. H., 1987, Astrophysical Journal, Supplement, 64, 83 39, 40, 43, 44, 46, 48, 49, 50, 51, 52, 54, 55, 68, 69, 99, 109, 110

Cenarro A. J., et al., 2007, Monthly Notices of the Royal Astronomical Society, 374, 664 31

Chabrier G., 2003, Publications of the Astronomical Society of the Pacific, 115, 763 29, 30, 43, 44, 45, 48, 54, 58, 63, 89, 92, 96

Charlot S., Bruzual A. G., 1991, The Astrophysical Journal, 367, 126 24, 25, 58

Charlot S., Fall S. M., 2000, The Astrophysical Journal, 539, 718 12, 39, 58, 88, 91, 96, 99

Charlot S., Longhetti M., 2001, Monthly Notices of the Royal Astronomical Society, 323, 887 59, 99

Chavez M., Bertone E., Buzzoni A., Franchini M., Malagnini M. L., Morossi C., Rodriguez-Merino L. H., 2007, The Astrophysical Journal, 657, 1046 38, 39, 41, 42, 44, 105

Chavez M., Bertone E., Morales-Hernandez J., Bressan A., 2009, The Astrophysical Journal, 700, 694 19, 38

Chen Y., Trager S., Peletier R., Lançon A., 2011, Journal of Physics Conference Series, 328, 012023 31

Chen Y., Bressan A., Girardi L., Marigo P., Kong X., Lanza A., 2015, Monthly Notices of the Royal Astronomical Society, 452, 1068 29, 40

Chevallard J., Charlot S., 2016, Monthly Notices of the Royal Astronomical Society, 462, 1415 51, 52, 60, 64, 81, 82

Chevallard J., Charlot S., Wandelt B., Wild V., 2013, Monthly Notices of the Royal Astronomical Society, 432, 2061 88, 92, 96

Christensen L., et al., 2012, Monthly Notices of the Royal Astronomical Society, 427, 1973 38, 71, 72

Colucci J. E., Bernstein R. A., Cameron S. A., McWilliam A., 2012, The Astrophysical Journal, 746, 29 49

Conroy C., Gunn J. E., 2010, The Astrophysical Journal, 712, 833 24

Conroy C., Gunn J. E., White M., 2009, The Astrophysical Journal, 699, 486 25

Dirsch B., Richtler T., Gieren W. P., Hilker M., 2000, Astronomy & Astrophysics, 360, 133 50

Draine B. T., 1990, in Blitz L., ed., Astronomical Society of the Pacific Conference Series Vol. 12, The Evolution of the Interstellar Medium. pp 193–205 10

Elson R. A. W., 1991, Astrophysical Journal, Supplement, 76, 185 50

Elson R. A., Fall S. M., 1988, The Astronomical Journal, 96, 1383 50

Erb D. K., Pettini M., Shapley A. E., Steidel C. C., Law D. R., Reddy N. A., 2010, The Astrophysical Journal, 719, 1168 38, 71, 72, 86

Faber S. M., 1972, Astronomy & Astrophysics, 20, 361 24

Faisst A. L., et al., 2016, The Astrophysical Journal, 822, 29 39

Fanelli M. N., O'Connell R. W., Burstein D., Wu C.-C., 1992, Astrophysical Journal, Supplement, 82, 197 19, 38, 39, 40, 41, 42, 43, 44, 45, 46, 48, 49, 67, 68, 69, 77, 99, 100, 105, 109, 110

Feltre A., Charlot S., Gutkin J., 2016, Monthly Notices of the Royal Astronomical Society, 456, 3354 55, 72, 93, 94, 101

Ferland G. J., Korista K. T., Verner D. A., Ferguson J. W., Kingdon J. B., Verner E. M., 1998, Publications of the Astronomical Society of the Pacific, 110, 761 32

Ferland G. J., et al., 2013a, Revista Mexicana de Astronomia y Astrofisica, 49, 137 31, 39, 59, 60

Ferland G. J., Kisielius R., Keenan F. P., van Hoof P. A. M., Jonauskas V., Lykins M. L., Porter R. L., Williams R. J. R., 2013b, The Astrophysical Journal, 767, 123 24, 32

Feroz F., Hobson M. P., Bridges M., 2009, Monthly Notices of the Royal Astronomical Society, 398, 1601 81

Ferrière K. M., 2001, Reviews of Modern Physics, 73, 1031 61, 62

Fioc M., Rocca-Volmerange B., 1997, Astronomy & Astrophysics, 326, 950 24

Fouesneau M., Lançon A., Chandar R., Whitmore B. C., 2012, The Astrophysical Journal, 750, 60 39, 44, 99

Frank A., Mellema G., 1994, Astronomy & Astrophysics, 289, 937 32

González Delgado R. M., Leitherer C., Heckman T., Lowenthal J. D., Ferguson H. C., Robert C., 1998, The Astrophysical Journal, 495, 698 38

Gräfener G., Koesterke L., Hamann W.-R., 2002, Astronomy & Astrophysics, 387, 244 31, 41

Gray R. O., Corbally C. J., 1994, Astronomical Journal, 107, 742 33

Gregg M. D., et al., 2004. p. 94.06, `http://adsabs.harvard.edu/abs/2004AAS...205.9406G` 31

Grevesse N., Sauval A. J., 1998, Nature, 85, 161 61

Grimes J. P., et al., 2009, The Astrophysical Journal Supplement Series, 181, 272 93

Groves B. A., Dopita M. A., Sutherland R. S., 2004, Astrophysical Journal, Supplement, 153, 75 61

Gruenwald R., Viegas S. M., Broguière D., 1997, The Astrophysical Journal, 480, 283 32

Guiderdoni B., Rocca-Volmerange B., 1987, Astronomy & Astrophysics, 186, 1 24

Gustafsson B., Bell R. A., Eriksson K., Nordlund A., 1975, Astronomy & Astrophysics, 42, 407 31

Gutkin J., Charlot S., Bruzual G., 2016, Monthly Notices of the Royal Astronomical Society, 462, 1757 59, 60, 61, 64, 66, 72, 88, 90, 93, 94, 99

Haardt F., Salvaterra R., 2015, Astronomy & Astrophysics, 575, L16 6

Haffner L. M., et al., 2009, Reviews of Modern Physics, 81, 969 61

Hainich R., et al., 2014, Astronomy & Astrophysics, 565, A27 31, 41

Halliday C., et al., 2008, Astronomy & Astrophysics, 479, 9 38

Hamann W.-R., Gräfener G., 2003, Astronomy & Astrophysics, 410, 993 31, 41

Hamann W.-R., Gräfener G., 2004, Astronomy & Astrophysics, 427, 697 38, 39, 41

Hamann W.-R., Gräfener G., Liermann A., 2006, Astronomy & Astrophysics, 457, 1015 31, 41

Hastings W. K., 1970, Biometrika, 57, 97 80

Hauschildt P. H., Baron E., 1999, Journal of Computational and Applied Mathematics, 109, 41 38

Hauschildt P. H., Baron E., Allard F., 1997, The Astrophysical Journal, 483, 390 31

Heap S. R., Hubeny I., Lanz T. M., 2001, Astrophysics and Space Science Supplement, 277, 263 31, 39, 60, 99

Hillier D. J., Miller D. L., 1998, The Astrophysical Journal, 496, 407 31

Hillier D. J., Miller D. L., 1999, The Astrophysical Journal, 519, 354 38

Howarth I. D., 1983, Monthly Notices of the Royal Astronomical Society, 203, 301 48

Hubble E. P., 1926, Astrophysical Journal, 64 6

Hubble E., 1929, Proceedings of the National Academy of Science, 15, 168 5

Hubeny I., 1988, Computer Physics Communications, 52, 103 33

Hubeny I., Lanz T., 1995, The Astrophysical Journal, 439, 875 24, 31, 40

Hubeny I., Lanz T., 2011, Synspec: General Spectrum Synthesis Program, Astrophysics Source Code Library (ascl:1109.022) 24, 33, 39, 60, 99

Hubeny I., Heap S. R., Lanz T. M., 2000, in American Astronomical Society Meeting Abstracts #196. p. 718 24, 31, 39, 60, 99

Iben Jr. I., Tutukov A. V., 1985, Astrophysical Journal Supplement Series, 58, 661 28

Inoue A. K., Shimizu I., Iwata I., Tanaka M., 2014, Monthly Notices of the Royal Astronomical Society, 442, 1805 88

Izotov Y. I., Lipovetsky V. A., Chaffee F. H., Foltz C. B., Guseva N. G., Kniazev A. Y., 1997, The Astrophysical Journal, 476, 698 91

James B. L., Aloisi A., Heckman T., Sohn S. T., Wolfe M. A., 2014, The Astrophysical Journal, 795, 109 38, 67

Jasniewicz G., Thevenin F., 1994, Astronomy & Astrophysics, 282, 717 50

Jeffreys H., 1961, Theory of probability. Oxford University Press 80

Jehin E., Bagnulo S., Melo C., Ledoux C., Cabanac R., 2005. pp 261–262, doi:10.1017/S1743921305005739, `http://adsabs.harvard.edu/abs/2005IAUS..228..261J` 31

Johnson R. A., Beaulieu S. F., Gilmore G. F., Hurley J., Santiago B. X., Tanvir N. R., Elson R. A. W., 2001, Monthly Notices of the Royal Astronomical Society, 324, 367 50

Kennicutt Jr. R. C., 1983, The Astrophysical Journal, 272, 54 29

Kochukhov O. P., 2007, in Romanyuk I. I., Kudryavtsev D. O., Neizvestnaya O. M., Shapoval V. M., eds, Physics of Magnetic Stars. pp 109–118 (`arXiv:astro-ph/0701084`) 33

Korn A. J., Becker S. R., Gummersbach C. A., Wolf B., 2000, Astronomy & Astrophysics, 353, 655 50

Korn A. J., Maraston C., Thomas D., 2005, Astronomy & Astrophysics, 438, 685 19

Kroupa P., 2001, Monthly Notices of the Royal Astronomical Society, 322, 231 29

Kroupa P., Tout C. A., Gilmore G., 1993, Monthly Notices of the Royal Astronomical Society, 262, 545 29

Kurucz R. L., 1970, SAO Special Report, 309, 309 31

Kurucz R. L., 1992, in Barbuy B., Renzini A., eds, IAU Symposium Vol. 149, The Stellar Populations of Galaxies. p. 225 33

Lanz T., Hubeny I., 2003, Astrophysical Journal, Supplement, 146, 417 31, 33, 38, 39, 40

Lanz T., Hubeny I., 2007, Astrophysical Journal, Supplement, 169, 83 31, 38, 39, 40

Le Borgne J.-F., et al., 2003, Astronomy & Astrophysics, 402, 433 31

Le Fèvre O., et al., 2013, Astronomy & Astrophysics, 559, A14 67

Lebouteiller V., Kunth D., Lequeux J., Lecavelier des Etangs A., Désert J.-M., Hébrard G., Vidal-Madjar A., 2004, Astronomy & Astrophysics, 415, 55 38

Lebouteiller V., Kunth D., Thuan T. X., Désert J. M., 2009, Astronomy & Astrophysics, 494, 915 38

Lebouteiller V., Heap S., Hubeny I., Kunth D., 2013, Astronomy & Astrophysics, 553, 32 38, 60, 67

Lee H., Skillman E. D., 2004, The Astrophysical Journal, 614, 698 38

Lee H.-c., Worthey G., 2005, The Astrophysical Journal Supplement Series, 160, 176 19

Leitherer C., Heckman T. M., 1995, The Astrophysical Journal Supplement Series, 96, 9 24

Leitherer C., Robert C., Heckman T. M., 1995, Astrophysical Journal, Supplement, 99, 173 77

Leitherer C., et al., 1999, Astrophysical Journal, Supplement, 123, 3 38, 69

Leitherer C., Leão J. R. S., Heckman T. M., Lennon D. J., Pettini M., Robert C., 2001, The Astrophysical Journal, 550, 724 38, 69, 70, 100

Leitherer C., Ortiz Otálvaro P. A., Bresolin F., Kudritzki R.-P., Lo Faro B., Pauldrach A. W. A., Pettini M., Rix S. A., 2010, Astrophysical Journal, Supplement, 189, 309 38, 39, 40, 41

Leitherer C., Tremonti C. A., Heckman T. M., Calzetti D., 2011, The Astronomical Journal, 141, 37 19, 38, 41, 42, 48, 64, 72, 105, 109, 111

Liu Q., de Grijs R., Deng L. C., Hu Y., Beaulieu S. F., 2009, VizieR Online Data Catalog, 350 50

Maciel W. J., 2013, Astrophysics of the Interstellar Medium, doi:10.1007/978-1-4614-3767-3. 62

Mackey A. D., Gilmore G. F., 2003, Monthly Notices of the Royal Astronomical Society, 338, 85 39, 50

Maraston C., 1998, Monthly Notices of the Royal Astronomical Society, 300, 872 24

Maraston C., 2005, Monthly Notices of the Royal Astronomical Society, 362, 799 24

Maraston C., Colmenárez L. N., Bender R., Thomas D., 2009, Astronomy & Astrophysics, 493, 20 19, 39, 41, 44, 48, 50, 105, 109

Marigo P., Bressan A., Nanni A., Girardi L., Pumo M. L., 2013, Monthly Notices of the Royal Astronomical Society, 434, 488 40

Marten H., Schoenberner D., 1991, Astronomy & Astrophysics, 248, 590 32

Martins L. P., Coelho P., 2007, Monthly Notices of the Royal Astronomical Society, 381, 1329 31

Martins L. P., González Delgado R. M., Leitherer C., Cerviño M., Hauschildt P., 2005, Monthly Notices of the Royal Astronomical Society, 358, 49 38, 40

Mathis J. S., 1986, Publications of the Astronomical Society of the Pacific, 98, 995 66

McLaughlin D. E., van der Marel R. P., 2005, Astrophysical Journal, Supplement, 161, 304 39, 50

McLean I. S., et al., 2012, in Ground-based and Airborne Instrumentation for Astronomy IV. p. 84460J, doi:10.1117/12.924794 86

Mehlert D., et al., 2002, Astronomy & Astrophysics, 393, 809 38

Mehlert D., Tapken C., Appenzeller I., Noll S., de Mello D., Heckman T. M., 2006, Astronomy & Astrophysics, 455, 835 38

Mellema G., 1995, Monthly Notices of the Royal Astronomical Society, 277, 173 32

Mellema G., Frank A., 1995, Monthly Notices of the Royal Astronomical Society, 273, 401 32

Metropolis N., Rosenbluth A. W., Rosenbluth M. N., Teller A. H., Teller E., 1953, The Journal of Chemical Physics, 21, 1087 80

Miller G. E., Scalo J. M., 1979, The Astrophysical Journal Supplement Series, 41, 513 29

Moiseev A. V., Tikhonov A. V., Klypin A., 2015, Monthly Notices of the Royal Astronomical Society, 449, 3568 64

Morisset C., 2006, Proceedings of the International Astronomical Union, 2, 467 32

Murray N., 2011, The Astrophysical Journal, 729, 133 44, 48, 59, 99

Murray N., Quataert E., Thompson T. A., 2010, The Astrophysical Journal, 709, 191 44, 48, 59, 99

Netzer H., Ferland G. J., 1984, Publications of the Astronomical Society of the Pacific, 96, 593 32

Niederhofer F., Hilker M., Bastian N., Silva-Villa E., 2015, Astronomy & Astrophysics, 575, A62 50

Och S. R., Lucy L. B., Rosa M. R., 1998, Astronomy & Astrophysics, 336, 301 32

Oesch P. A., et al., 2015, The Astrophysical Journal Letters, 804, L30 86, 87

Oliva E., Origlia L., 1998, Astronomy & Astrophysics, 332, 46 50

Pacifici C., Charlot S., Blaizot J., Brinchmann J., 2012, Monthly Notices of the Royal Astronomical Society, 421, 2002 34

Patrício V., et al., 2016, Monthly Notices of the Royal Astronomical Society, 456, 4191 67

Pauldrach A., Puls J., Kudritzki R. P., 1986, Astronomy & Astrophysics, 164, 86 31

Pauldrach A. W. A., Hoffmann T. L., Lennon M., 2001, Astronomy & Astrophysics, 375, 161 38, 40

Pequignot D., Stasińska G., Aldrovandi S. M. V., 1978, Astronomy & Astrophysics, 63, 313 32

Pessev P. M., Goudfrooij P., Puzia T. H., Chandar R., 2008, Monthly Notices of the Royal Astronomical Society, 385, 1535 110

Pettini M., Steidel C. C., Adelberger K. L., Dickinson M., Giavalisco M., 2000, The Astrophysical Journal, 528, 96 38, 67

Pettini M., Rix S. A., Steidel C. C., Adelberger K. L., Hunt M. P., Shapley A. E., 2002, The Astrophysical Journal, 569, 742 38, 72

Pickles A. J., 1998, Publications of the Astronomical Society of the Pacific, 110, 863 31

Pietrzyński G., et al., 2013, Nature, 495, 76 110

Planck Collaboration et al., 2016, Astronomy & Astrophysics, 594, A13 6

Porter T. A., Strong A. W., 2005, International Cosmic Ray Conference, 4, 77 62

Prugniel P., Soubiran C., 2001, Astronomy & Astrophysics, 369, 1048 31

Prugniel P., Vauglin I., Koleva M., 2011, Astronomy & Astrophysics, 531, A165 31

Puls J., Urbaneja M. A., Venero R., Repolust T., Springmann U., Jokuthy A., Mokiem M. R., 2005, Astronomy & Astrophysics, 435, 669 38

Rauch T., 2002, in Henney W. J., Franco J., Martos M., eds, Revista Mexicana de Astronomia y Astrofisica, vol. 27 Vol. 12, Revista Mexicana de Astronomia y Astrofisica Conference Series. pp 150–151 41

Rayner J. T., Cushing M. C., Vacca W. D., 2009, The Astrophysical Journal Supplement Series, 185, 289 31

Riess A. G., et al., 1998, The Astronomical Journal, 116, 1009 5

Rix S. A., Pettini M., Leitherer C., Bresolin F., Kudritzki R.-P., Steidel C. C., 2004, The Astrophysical Journal, 615, 98 39, 69, 70, 100

Roberts-Borsani G. W., et al., 2016, The Astrophysical Journal, 823, 143 86, 87, 88, 89

Robitaille T. P., Whitney B. A., 2010, Astrophysical Journal, Letters, 710, L11 62

Rodriguez-Gaspar J. A., Tenorio-Tagle G., 1998, Astronomy & Astrophysics, 331, 347 32

Rodríguez-Merino L. H., Chavez M., Bertone E., Buzzoni A., 2005, The Astrophysical Journal, 626, 411 38, 39, 40

Salpeter E. E., 1955, The Astrophysical Journal, 121, 161 29

Sánchez-Blázquez P., et al., 2006, Monthly Notices of the Royal Astronomical Society, 371, 703 31, 40

Sander A., Hamann W.-R., Todt H., 2012, Astronomy & Astrophysics, 540, A144 31, 41

Santos Jr. J. F. C., Frogel J. A., 1997, The Astrophysical Journal, 479, 764 44

Savage B. D., Mathis J. S., 1979, Annual Review of Astronomy and Astrophysics, 17, 73 48

Savage B. D., de Boer K. S., 1979, Astrophysical Journal, Letters, 230, L77 48

Savage B. D., de Boer K. S., 1981, The Astrophysical Journal, 243, 460 48

Savage B. D., Sembach K. R., Lu L., 1997, The Astronomical Journal, 113, 2158 48

Savage B. D., et al., 2000, Astrophysical Journal, Supplement, 129, 563 48, 64, 109

Scalo J. M., 1986, Fundamentals of Cosmic Physics, 11, 1 29

Schmidt-Voigt M., Koeppen J., 1987, Astronomy & Astrophysics, 174, 211 32

Schneider R., Ferrara A., Natarajan P., Omukai K., 2002, The Astrophysical Journal, 571, 30 9

Sembach K. R., Howk J. C., Ryans R. S. I., Keenan F. P., 2000, The Astrophysical Journal, 528, 310 38

Shapley A. E., Steidel C. C., Pettini M., Adelberger K. L., 2003, The Astrophysical Journal, 588, 65 19, 38, 67, 71, 72

Shirazi M., Brinchmann J., 2012, Monthly Notices of the Royal Astronomical Society, 421, 1043 95

Skilling J., 2006, Bayesian Anal., 1, 833 81

Sobral D., Matthee J., Darvish B., Schaerer D., Mobasher B., Röttgering H. J. A., Santos S., Hemmati S., 2015, The Astrophysical Journal, 808, 139 19, 38

Sommariva V., Mannucci F., Cresci G., Maiolino R., Marconi A., Nagao T., Baroni A., Grazian A., 2012, Astronomy & Astrophysics, 539, A136 39, 69, 70, 100

Spergel D. N., et al., 2003, The Astrophysical Journal Supplement Series, 148, 175 5

Spinrad H., Taylor B. J., 1971, The Astrophysical Journal Supplement Series, 22, 445 24

Stark D. P., et al., 2014, Monthly Notices of the Royal Astronomical Society, 445, 3200 19, 38, 55, 64, 67, 71, 72, 86, 91

Stark D. P., et al., 2015a, Monthly Notices of the Royal Astronomical Society, 450, 1846 19, 38, 55, 71, 72, 95

Stark D. P., et al., 2015b, Monthly Notices of the Royal Astronomical Society, 454, 1393 19, 95

Stark D. P., et al., 2016, Monthly Notices of the Royal Astronomical Society, 86, 87, 88, 89

Steidel C. C., Erb D. K., Shapley A. E., Pettini M., Reddy N., Bogosavljević M., Rudie G. C., Rakic O., 2010, The Astrophysical Journal, 717, 289 19, 38, 100, 101

Steidel C. C., Strom A. L., Pettini M., Rudie G. C., Reddy N. A., Trainor R. F., 2016, The Astrophysical Journal, 826, 159 19

Sutherland R. S., Dopita M. A., 1993, The Astrophysical Journal Supplement Series, 88, 253 32

Thuan T. X., Lecavelier des Etangs A., Izotov Y. I., 2002, The Astrophysical Journal, 565, 941 38

Thuan T. X., Lecavelier des Etangs A., Izotov Y. I., 2005, The Astrophysical Journal, 621, 269 38

Tinsley B. M., 1978, The Astrophysical Journal, 222, 14 24

Trager S. C., Worthey G., Faber S. M., Burstein D., González J. J., 1998, Astrophysical Journal, Supplement, 116, 1 41

Tripicco M. J., Bell R. A., 1995, Astronomical Journal, 110, 3035 19

Tylenda R., 1979, Acta Astronomica, 29, 355 32

Valdes F., Gupta R., Rose J. A., Singh H. P., Bell D. J., 2004, The Astrophysical Journal Supplement Series, 152, 251 31

Vazdekis A., 1999, The Astrophysical Journal, 513, 224 24

Vink J. S., de Koter A., Lamers H. J. G. L. M., 2001, Astronomy & Astrophysics, 369, 574 78

Walborn N. R., Panek R. J., 1984, Astrophysical Journal, Letters, 280, L27 41, 77

Warmels R. H., 1988, Astronomy and Astrophysics Supplement Series, 72, 427 66

Wild V., et al., 2011, Monthly Notices of the Royal Astronomical Society, 410, 1593 90, 92, 96

Wofford A., Leitherer C., Chandar R., 2011, The Astrophysical Journal, 727, 100 77

Wofford A., et al., 2016, preprint, (`arXiv:1601.03850`) 40, 99

Worthey G., 1994, The Astrophysical Journal Supplement Series, 95, 107 19, 24

de Grijs R., Gilmore G. F., Johnson R. A., Mackey A. D., 2002, Monthly Notices of the Royal Astronomical Society, 331, 245 50

van Hoof P. A. M., Weingartner J. C., Martin P. G., Volk K., Ferland G. J., 2004, Monthly Notices of the Royal Astronomical Society, 350, 1330 60

van den Bergh S., Hagen G. L., 1968, The Astronomical Journal, 73, 569 110